ASTROCENT

Measurement of Nuclear Recoils in Liquid Argon for Dark Matter Searches

Thesis by:
Paules Zakhary

In partial fulfillment for the degree of
Doctor of Philosophy
In
Astronomy

Advisors: Masayuki Wada
Marcin Kuźniak

AstroCeNT: Particle Astrophysics Science and Technology Centre,
Nicolaus Copernicus Astronomical Center,
The Polish Academy of Sciences
Warsaw, Poland

2024

Paules Zakhary
ORCID: 0000-0001-9752-1790

Abstract

Advancements in the field of astroparticle physics have always hinged on the development of sensitive experiments to detect elusive natural phenomena. Despite many evidence spanning diverse cosmological scales substantiating the *existence* of dark matter, its *nature* i.e. its particle physics properties, remains undetermined. As a result, a concerted effort is underway to detect Weakly Interacting Massive Particles (WIMPs), one of the leading dark matter candidates, by employing various detection technologies. These systems are designed to detect very low energy deposits resulting from the direct interaction of WIMPs with the target material of the experiment, e.g. liquefied noble gases or solid crystals.

The pursuit has already narrowed down the parameter space of WIMPs with masses around $\mathcal{O}(10\,\mathrm{GeV/c^2})$ and cross-sections of $\mathcal{O}(10^{-45}\,\mathrm{cm^2})$. Presently, the research is progressing towards lower masses of $\mathcal{O}(1\,\mathrm{GeV/c^2})$. For liquid argon (LAr) detectors, this entails less energetic recoils i.e. the sensitivity requirement transitions from $20 - 100\,\mathrm{keV}$ to $\mathcal{O}(1\,\mathrm{keV})$.

To probe this low-mass range, it is crucial to accurately characterize the LAr response to low-energy nuclear recoils (NRs). This dissertation provides a comprehensive overview of the work carried out using the ReD experiment to measure NRs in an LAr time projection chamber (TPC), with a focus on examining the ionization yield down to $1 - 2\,\mathrm{keV}_{nr}$. A thorough understanding of this response is of fundamental importance for optimizing the sensitivity of both current and next-generation LAr-based detectors employed in rare-event searches such as dark matter detection.

Streszczenie

Postępy w dziedzinie astrofizyki cząstek zwykle opierały się na rozwoju czułych eksperymentów mających na celu wykrywanie trudnych do uchwycenia zjawisk naturalnych. Pomimo wielu dowodów, które obejmują różne skale kosmologiczne i potwierdzają *istnienie* ciemnej materii, jej *natura*, tj. jej konkretne mikro-fizyczne właściwości, pozostaje nieokreślona. W związku z tym trwają intensywne prace mające na celu wykrycie, poprzez zastosowanie różnych technologii detekcji, Słabo Oddziałujących Masywnych Cząstek (WIMP), jednego z wiodących kandydatów na ciemną materię. Detektory te są zaprojektowane tak, aby wykryć bardzo niskie zdeponowane energie wynikające z bezpośredniej interakcji WIMP-ów z materiałem tarczy eksperymentu, np. ze skroplonymi gazami szlachetnymi lub ciałami stałymi.

Wyniki poszukiwań już zawęziły przestrzeń parametrów WIMP-ów o masach rzędu 10 GeV/c^2 do przekrojów czynnych co najwyżej rzędu 10^{-45} cm^2. Obecnie badania zmierzają ku niższym masom rzędu GeV/c^2. Dla detektorów ciekło-argonowych (LAr) oznacza to jeszcze mniejsze zdeponowane energie odrzutów jądrowych, tj. zamiast czułości na 20 – 100 keV wymagana będzie czułość na zdeponowane energie rzędu keV.

Aby zbadać ten zakres niskich mas, kluczowe jest dokładne scharakteryzowanie odpowiedzi LAr na odrzuty jądrowe o niskiej energii. Niniejsza rozprawa dostarcza kompleksowego przeglądu prac wykonanych za pomocą eksperymentu ReD w celu pomiaru NR w ciekło-argonowej komorze projekcji czasowej (TPC), koncentrując się na badaniu wydajności jonizacji aż do energii odrzutu $1 - 2\,\mathrm{keV}_{nr}$. Dokładne zrozumienie odpowiedzi LAr jest fundamentalne dla optymalizacji czułości zarówno obecnych, jak i przyszłych detektorów opartych na LAr, stosowanych w poszukiwaniach rzadkich zdarzeń, takich jak wykrywanie ciemnej materii.

Acknowledgements

Above all, I want to thank God, who is the reason for my existence and whose love and guidance have shaped every step of my life. He has protected me in ways I know and in ways I will never understand, leading me to this moment with more grace and blessing than I could have imagined. His constant presence fills my life with strength, and He has surrounded me with incredible people who have made my journey richer and more meaningful. For all of this, and countless other reasons, I am forever indebted.

I am profoundly grateful to my parents for always supporting that curious kid and backing my often unconventional life choices. Your example of perseverance and sacrifice has deeply inspired me. To my sister, *Pistis*, I owe a debt of gratitude for the countless ways you have enriched my life. You have been my rock, a second mother, and my closest friend. Your love and the values you have instilled in me mean far more than I can put into words. And to my brother, *Athanasius*, thank you for showing me through your own decisions the courage it takes to make bold choices. Watching you navigate your own path has been a guiding light for me. A heartfelt thanks to my uncle, *Dr. Ashraf Zakhary*, in Australia. Despite the distance, you have always been a constant source of support, listening with genuine care and sharing long talks about my wild ideas. You have made a meaningful difference in my life, and I'm truly thankful for everything.

To Prof. Masayuki Wada, I am deeply grateful for your kindness and compassion during my times of distress. Your unwavering support and patience in guiding my growth as a researcher mean a great deal to me. To Prof. Luciano Pandola, thank you for your articulate and engaging explanations, which made my learning experience both enlightening and enjoyable.

I would also like to express my deep gratitude to everyone I've encountered throughout my academic journey. Each of you has played a meaningful role in shaping my path . Although the list is very long, I want to offer a special thanks to Prof. Mohammad AlFiky, who first sparked my curiosity and passion for science. To Prof. Gerald Gabrielse and Prof. Daniel Ang, thank you for your early support, which made a lasting impact on my academic development. I am especially thankful to Prof. Vitaly Kudryavtsev, Prof. Marcin Kuźniak, and Prof. Shawn Westerdale for your unwavering dedication and generosity in sharing your knowledge with me. Thanks to the entire team at AstroCeNT, and especially Yuliya Hoika—thank you for being a genuinely kind and beautiful soul. Your presence truly made a difference; the office would not have been the same without you.

Thanks to my friends in Egypt–Sandra Mosaad, Mina Ibrahim, Mina Medhat, and Ismail Mohammad– for always knowing how to lift my spirits and support me during difficult times. Your friendship, despite the distance and rare meetings, means the world to me. Thanks to Giusseppe Piparo and Chiara Failla for being there for me in moments of struggle. Your presence and kindness have truly made a difference.

Last but not least, this journey has led me to meet someone incredibly special who has made everything so much more meaningful. I am truly grateful that our paths crossed and that we recognized it when it happened. *Fiorella Tringali*, thank you for being my home away from home, for bringing so much value into my life, and for accepting me for who I am. Thanks for being you and for making the end of this journey so much easier. I can not wait to embark on our next adventurous journey together!

In Memory of Uncle Magdy,

Your light still shines bright,
a guiding flame in my sight,

You never spoke of how to be,
but showed the way for all to see.

Thanks for everything...

Table of Contents

List of Illustrations

CHAPTER I

Introduction to Dark Matter

Gravitational effects seen within a broad range of cosmological scales, from dwarf galaxies to superclusters, suggest the existence of unobserved, *dark*, mass. The story began in the early 1930s when Jan Oort investigated the dynamics of stars in the Milky Way. By examining the vertical motion of stars above and below the galactic plane, he found that the gravitational pull due to luminous mass can not *solely* hold the galactic system together unless about 85 % of the stellar light was obscured by dust and intervening matter [1].

This mystery was soon extended by Fritz Zwicky to a larger scale, in particular within the Coma cluster about 99 Mpc from Earth. Zwicky employed the virial theorem to estimate the total mass of the cluster, discovering that the visible galaxies accounted for only a small fraction of the total mass needed to keep the cluster gravitationally bound. He proposed the presence of a substantial amount of unseen mass, which he termed *Dark Matter* (DM), necessary to account for the observed gravitational effects [2].

This concept of missing mass was further solidified by Vera Rubin's groundbreaking work in the 1970s. Rubin, along with her collaborator Kent Ford, studied the rotational curves of spiral galaxies. They found that the rotational velocities of stars and gas in these galaxies remained high even at large radii from the galactic center, contrary to expectations based on visible mass alone. This observation strongly suggested the presence of an extended DM halo enveloping the galaxies, exerting its gravitational influence beyond the visible edges [3].

In this chapter, I will examine two of the most compelling evidence for the existence of a new class of matter beyond the Standard Model (SM). However, prior to exploring these findings in detail, I will first establish key cosmological principles, which will serve as the basis for the subsequent discussion.

1.1 Cosmology Framework: ΛCDM Model

ΛCDM model is the leading theoretical framework in cosmology that describes the composition and evolution of the Universe. It is built upon our understanding of the key concepts of Einstein's General theory of relativity, which describes gravity not as a force but as a consequence of the curvature of space-time caused by mass and energy. This is encapsulated in the elegant formulation of Einstein field equations that relates the geometry of a curved space-time to its matter and energy content as:

$$R_{\mu\nu} - \frac{1}{2}g_{\mu\nu}R + \Lambda g_{\mu\nu} = \frac{8\pi G_N}{c^4}T_{\mu\nu}, \tag{1.1}$$

where $R_{\mu\nu}$ is the Ricci curvature tensor, R is the Ricci scalar, $g_{\mu\nu}$ is the metric tensor, Λ is the so-called cosmological constant, G_N is the gravitational constant, c is the speed of light, and $T_{\mu\nu}$ is the energy-momentum tensor. This Λ factor was introduced to account for the observed accelerated expansion of the Universe [4, 5].

The ΛCDM model is derived from the Einstein field equations under the assumption of a homogeneous and isotropic Universe, which is described by the Friedmann-Lemaître-Robertson-Walker (FLRW) metric:

$$ds^2 = -c^2dt^2 + a(t)^2\left(\frac{dr^2}{1-kr^2} + r^2d\Omega^2\right), \tag{1.2}$$

where k can be $+1$, 0, or -1 corresponding to positive, zero, or negative spatial curvature, respectively. $d\Omega^2$ represents the metric on the unit sphere. $a(t)$ is the cosmic scale factor which represents how distances between two points at rest with respect to each other evolves in time due to the expansion of the Universe.

Solving Eq. 1.1 for this metric in Eq. 1.2, one gets the Friedmann equations that governs the dynamics of the scale factor $a(t)$:

$$\left(\frac{\dot{a}}{a}\right)^2 = \frac{8\pi G_N}{3}\rho_{tot} - \frac{k}{a^2} + \frac{\Lambda}{3}. \tag{1.3}$$

Here, ρ_{tot} is the total energy density in the Universe [6, 7]. The Hubble parameter, $H(t) \equiv \frac{\dot{a}}{a}$, is typically introduced to quantify the rate of the Universe's expansion in terms of $a(t)$, the time-dependent cosmic scale factor.

Thus, the Hubble parameter is a time-dependent variable that is inversely related to the age of the Universe. The energy density ρ_{tot} can be conveniently expressed as a dimensionless parameter in terms of the critical density, which is defined from Eq. 1.3 corresponding to a flat Universe (i.e. $k = 0$), yielding:

$$\rho_{crit} \equiv \frac{3H_0^2}{8\pi G_N} = 1.87834(4) \cdot 10^{-29} h^2 \mathrm{g/cm}^3, \tag{1.4}$$

where the subscript "0" in H_0 signifies the current value of this time-dependent parameter [8]. While h is the dimensionless Hubble parameter given by:

$$h = \frac{H_0}{100\,\mathrm{km/s/Mpc}} = 0.674(5).$$

Therefore, the Friedmann equation can be simply written to demonstrate how the evolution of the Universe depends completely on its contents as:

$$\Omega - 1 = \frac{k}{H(t)^2 a^2}. \tag{1.5}$$

Here, $\Omega = \sum_i \Omega_i$, where i represent the different components contributing to the energy density, namely baryonic matter Ω_b, dark matter Ω_χ, radiation Ω_r, and dark energy Ω_Λ.

The ΛCDM model relates the evolution of the Hubble parameter to the several components of the total energy density by applying energy-momentum conservation as follows:

$$\frac{H(t)^2}{H_0^2} = \left[(\Omega_{\chi,0} + \Omega_{b,0})a^{-3} + \Omega_{r,0}a^{-4} + \Omega_{\Lambda,0}\right]. \tag{1.6}$$

1.2 Cosmic Microwave Background

During the recombination epoch, atoms started to form and photons decoupled from baryons causing the Universe to become transparent to electromagnetic radiation. Photons emitted at this epoch freely streamed through the Universe and were first detected on Earth by Penzias and Wilson in 1964 at Bell Labs [9], who identified an isotropic background in the radio-wave spectrum. This is the relic black-body radiation, released from the "last scattering" of that recombination epoch, which is now redshifted into the microwave spectrum and referred to as the cosmic microwave background (CMB).

Although the CMB is predominantly isotropic, reflecting the universe's overall homogeneity as depicted in Fig. 1.1, small anisotropies are primarily driven by early universe temperature fluctuations. By conceptualizing the early universe as a fluid comprising baryons and radiation, incorporating additional damping effects from non-baryonic DM, it becomes feasible to associate

these temperature variations to the energy densities of various particle species. More precisely, the energy densities of non-relativistic matter decrease proportional to $a(t)^{-3}$, whereas for radiation and relativistic particles, the energy density scales as $a(t)^{-4}$ due to the additional redshifting effects, as described by Eq. 1.6.

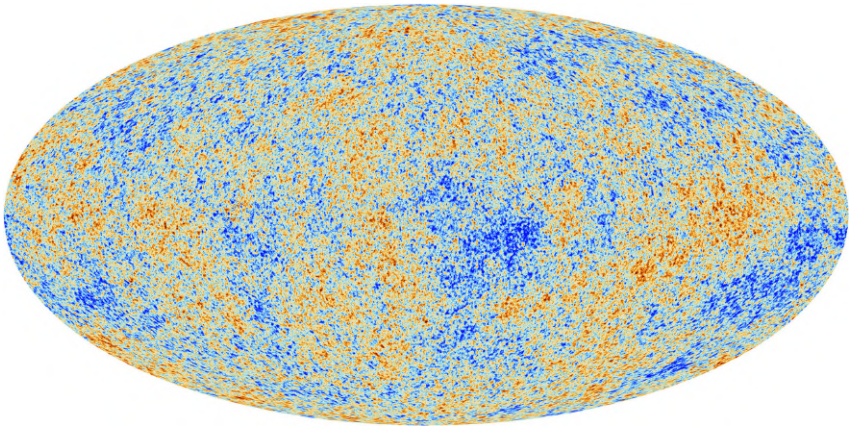

Figure 1.1: Temperature variations over the entire sky as measured by Planck. It shows overall homogeneity and isotropy with minor fluctuations. This map shows a range of 0.0005 K from the coldest (*blue*) to the hottest (*red*) parts representing areas of varying density fluctuations in the early universe across the sky. Credit: ESA and the Planck Collaboration

.

These fluctuations are driven by the interplay between gravity and radiation pressure. As shown in Fig. 1.2, on small scales, the power spectrum exhibits an incoherent acoustic oscillation around 1°, i.e. $\ell \sim 200$, resulting from the conflict within the extremely dense photon-Baryon plasma at that time. Photon pressure tends to erase anisotropies by expanding the plasma outward, while baryonic gravitational attraction enhances them by pulling the plasma back to form dense halos. This cycle of expansion and contraction continued until photons decoupled, emerging with distinct temperatures that reflect the initial density perturbations that allowed for the formation of early gravitational wells and the dynamics of the photon-baryon plasma.

Measurements of the intensity and scale of these CMB anisotropies delineate the prevalent energy densities during recombination ($z \sim 1100$), facilitating the utilization of ΛCDM cosmology to extrapolate primordial densities into the present. This process allows for understanding the particle physics occurring during that epoch and the determination of the present mass density, making the CMB an exceptionally powerful tool for probing the fundamental properties of various particle species.

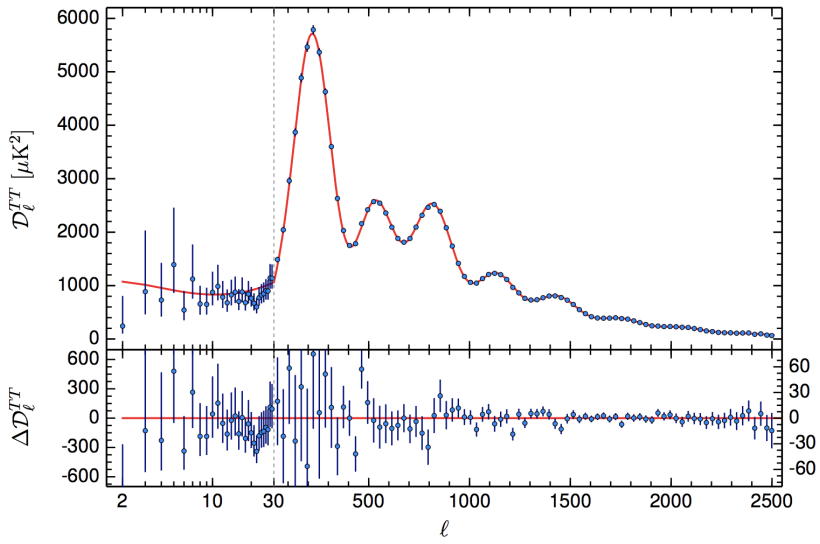

Figure 1.2: The CMB temperature power spectrum as reported by the Planck Collaboration in 2018 [8]. The relative height of the first few peaks and their locations help to determine the relative fraction and importance of DM, baryons, and radiation in the early universe. The *red solid line* is a fit to the ΛCDM theoretical prediction. The x-axis is logarithmic before the vertical gray dashed line at $\ell = 30$ and linear after.

The angular autocorrelation function of the CMB temperature fluctuations averaged over all directions n_1 and n_2 with $n_1 \cdot n_2 = \cos\theta$, is defined as [10]:

$$D_{TT}(\theta) = \left\langle \frac{\delta T}{T}(n_1)\frac{\delta T}{T}(n_2) \right\rangle \equiv \frac{1}{4\pi}\sum_{\ell=2}^{\infty}(2\ell+1)D_{TT,\ell}P_\ell(\cos\theta). \tag{1.7}$$

In this equation, $D_{TT}(\theta)$ quantifies the correlation between temperature fluctuations at different points on the sky, with ℓ representing the multipole expansion index and P_ℓ denoting the Legendre polynomials. The multipole moments encapsulate the amplitudes of these fluctuations, which arise from primordial density perturbations in the early universe. Lower ℓ values correspond to larger angular scales, while higher ℓ values relate to smaller angular scales.

The shape of the CMB angular power spectrum is sensitive to cosmological parameters. The first acoustic peak in the CMB power spectrum, seen around $\ell \sim 200$, results from the compression of the early universe's plasma. This peak's position, along with subsequent peaks, is influenced by the universe's curvature, as the ℓ values reflect the angular distance photons traveled to their last scattering surface. The amplitude of the first peak, and other odd-numbered peaks, increases with the amount of baryonic matter, which enhances plasma compression in acoustic oscillations.

In contrast, the second acoustic peak represents plasma rarefaction and is a harmonic of the first peak. Both types of peaks appear in the power spectrum because the CMB temperature's multipole expansion is sensitive to the absolute values of acoustic waves. The amplitude of even-numbered peaks, like the second, depends on plasma expansion and is unaffected by the baryonic matter.

The ratio of the first to the second peak amplitudes reveals the baryonic matter content of the universe. Additionally, the total non-relativistic mass affects the plasma's inertia, lowering the frequency of acoustic harmonics and suppressing higher frequency oscillations, which reduces the amplitude of subsequent peaks. Thus, the CMB power spectrum allows for separate evaluation of the total non-relativistic matter and baryonic matter in the universe.

In Fig. 1.2, the red line represents the optimal-fit of the ΛCDM model. This models features 6 parameters: the Hubble parameter H_0, the matter density parameter Ω_m, the baryon density parameter Ω_b, the DM density parameter Ω_χ, the scalar spectral index n_s, and the optical depth τ. The n_s describes how the density perturbations depend on the spatial scale, while τ is the mean free path for photon scattering, integrated from a certain time to the present-day. The fit results yield the total matter density and the relative fractions of baryonic and cold dark matter as:

$$\Omega_m = 0.315 \pm 0.007,$$

$$\Omega_b h^2 = 0.02237 \pm 0.00015, \qquad \text{and} \qquad \Omega_\chi^2 h^2 = 0.1200 \pm 0.0012.$$

This results in a ratio of cold dark matter to baryon density,

$$\frac{\Omega_\chi}{\Omega_b} \approx 5.4.$$

The Planck collaboration's robust fit demonstrated that the ΛCDM cosmological model comprising 4.9 % baryonic matter, 26.8 % dark matter, and 68.3 % dark energy aligns remarkably well with observational data [8]. This strong concordance provides one of the most compelling pieces of evidence for the existence of a form of DM that is non-baryonic and extends beyond the confines of the current SM of particle physics.

1.3 The Bullet Cluster

In 2004, a collision between two galaxy clusters that happened 100 million years ago was discovered, an event now known as the Bullet Cluster. This event is particularly significant due to the distinct behaviors exhibited by the clusters primary constituents when examined through X-ray emission, γ-ray emission, and gravitational lensing. The stellar components, identifiable by

their visible light emissions, depicted in the left panel of Fig. 1.3, passed through each other with negligible electromagnetic interaction, being influenced only by gravitational forces.

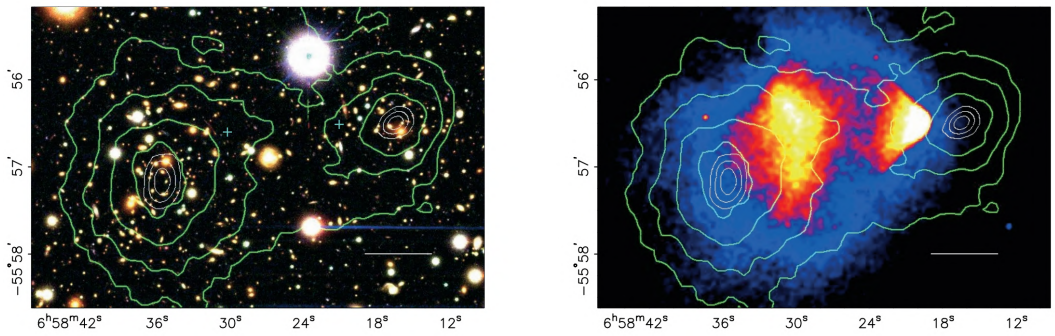

Figure 1.3: *Left*: The Magellan and Hubble Space telescopic image of the visible light observed from the ongoing collision of the bullet cluster showing individual galaxies or stars within them. *Right*: Chandra X-ray image showing the distribution of the plasma components of both merging clusters. The total mass density profile reconstructed from weak lensing is superimposed as (*green contours*) on both images. The centers of the plasma components are indicated as (*blue crosses*) on the *Left* image. Figure taken from [11].

The hot gas (plasma), which interact electromagnetically and is observable via X-ray imaging, were slowed down and concentrated at the centers of the colliding clusters, as shown in the right panel of Fig. 1.3 in red. Meanwhile, the DM component was inferred through weak gravitational lensing, which caused distortions in the images of background galaxies. This allowed for a two-dimensional reconstruction of the mass distribution of both galaxies, as illustrated by *green contours* in Fig. 1.3. The centers of these reconstructed mass distributions, represented by *green contours*, were found to be separated by eight standard deviations ($8\,\sigma$) from the centers of the plasma components, indicated by *blue crosses*.

This discrepancy is a very strong indication for the presence of an extremely weakly interacting form of matter, different than baryonic matter, with a total mass that far exceeds the baryonic mass. This allowed for estimating an upper limit on the self-interaction cross-section of DM per unit mass [12].

$$\frac{\sigma_{self}}{m_\chi} \lesssim 1\,\mathrm{cm}^2/\mathrm{g}$$

.

1.4 Selected Dark Matter Candidates

In the previous section, we reviewed some of the most compelling evidence for the existence of DM. The observations of gravitational effects across a wide range of cosmological scales, from dwarf galaxies to superclusters, suggest that DM candidates must exhibit specific properties to account for these phenomena. In this section, we will comprehensively review these properties, followed by an exploration of several theoretically motivated DM candidates.

- **Darkness:** As the name suggests, *Dark matter* is characterized by their minimal electromagnetic (EM) interaction with SM particles. In other words, they are not able to scatter photons, effectively rendering it "dark". This requirement implies that DM does not possess an electric charge. However, observational data does not completely rule out the possibility that DM particles could have an extremely small electric charge.

  For instance, the following constraint on the EM charge of DM particles with masses around the GeV scale is provided in [13] as:

  $$q_\chi \lesssim 10^{-4} \left(\frac{m_\chi}{\text{TeV}}\right)^{1/2}.$$

  A higher electric charge would result in a larger cross-section, leading to thermal equilibrium with SM particles in the early Universe. Moreover, a higher charge would impact DM behavior in stellar plasmas, and certain aspects of stellar dynamics allow us to impose stringent constraints on the presence of such particles. For more comprehensive details on DM fundamental charge, dipole moments and other types of charges, see references [14, 15].

- **Coldness:** DM must have clustered gravitationally over an extended period. Its behavior mimics that of non-relativistic particles bound by mutual gravitational attraction, which is necessary for amplifying the small perturbations observed in the CMB. Consequently, DM cannot be massless or relativistic; it needs to be cold, with low typical velocities, to effectively accumulate in galactic halos. Relativistic (hot) DM, which travels farther before being captured by gravitational wells, would lead to discrepancies with observations. This is why neutrinos, despite their potential as DM candidates if they were heavier, cannot account for all DM due to their high initial kinetic energies.

  Although thermal production is a leading method for generating DM, it is not a requirement. For DM to be considered cold in a thermal production scenario, the following condition must be satisfied:

  $$T \ll m_\chi,$$

where T is the temperature of the Universe when DM decoupled, and m_χ is the mass of the DM particle. Based on this criterion, any thermally produced DM candidate must have a mass, bounded in [16] as:

$$m_\chi \gtrsim \text{keV}.$$

This constraint does not apply to non-thermally produced DM, which can still exhibit low velocities and cluster on cosmological scales. A prominent example of non-thermal DM is the axion, which will be discussed further in this section.

- **Stability:** The earliest evidence for DM is derived from observations of the CMB, which provides a snapshot of the Universe approximately 13 billion years ago and continues to be detectable today. This suggests that if DM were to decay, its lifetime would need to be extraordinarily long, comparable to the age of the Universe.

$$\tau_{DM} \sim 10^{17}\text{s}$$

More stringent constraints on DM stability can be obtained by analyzing specific annihilation or decay channels within DM-dominated environments, which can help in detecting DM. This stability requirement is often addressed in theoretical models through imposing symmetries, such as R-parity in supersymmetry, K-parity in Kaluza-Klein theories, and discrete symmetries in little Higgs models, which prevent its decay into lighter particles [17]. Similarly, candidates like sterile neutrinos must have decay lifetimes exceeding the age of the Universe to be consistent with observational data [18].

- **Non-baryonic:** DM must be non-baryonic due to the constraints imposed by observations of CMB and big bang nucleosynthesis (BBN). These measurements reveal a precise amount of baryonic matter, as determined by the primordial production of elements like hydrogen, deuterium, helium, and lithium, which aligns closely with current observations which supports that the ratio of baryonic to DM is given by:

$$\frac{\Omega_\chi}{\Omega_b} \approx 5.4.$$

Given that BBN occurred in an era dominated by radiation, when the influence of DM would have been minimal, any contribution from baryonic matter would have disrupted these predictions. Therefore, to reconcile these observations with the ΛCDM model, DM must be composed of particles that do not interact with the primordial processes governing baryons.

- **Collisionless** DM must be largely collisionless to align with an observations such as those from the Bullet Cluster and the distribution of DM in galactic halos. If DM had significant self-interactions, we would observe deviations in cluster collisions and a loss of spherical symmetry in halos. Consider the Milky Way: its disk-like structure rather than a spherical shape is attributed to the interactions of SM particles and their dissipation into photons. Constraints from observations suggest that the cross-section for DM self-interactions must have a upper bound [19]:

$$\frac{\sigma_{self}}{m_\chi} \lesssim 1\,\mathrm{cm}^2/\mathrm{g}.$$

  While DM is primarily collisionless, models of self-interacting or partially interacting DM remain plausible and are actively explored [20].

1.4.1 Axions

Axions are compelling DM candidates due to their theoretical origins and potential to address several key problems in particle physics and cosmology. They were introduced by Peccei and Quinn to solve the strong CP problem in the SM [21]. The QCD Lagrangian includes a term that can violate charge parity (CP) symmetry, characterized by a parameter θ. If unconstrained, θ could result in a significant electric dipole moment for the neutron. However, since experiments have not detected such a dipole moment, θ must be less than 10^{-11}. This fine-tuning problem suggests the need for a new symmetry to prevent CP violation.

The Peccei-Quinn mechanism introduces a new *U(1)* chiral symmetry, which, when spontaneously broken at a scale f_a, generates a pseudo-Nambu-Goldstone boson known as the axion [22]. When the Lagrangian is rewritten to include the axion, its vacuum expectation value compensates for the CP-violating term in QCD, thus resolving the fine-tuning issue [23]. The axion couples to gluons and photons, with its mass that is linked to the symmetry-breaking scale f_a. This is expressed in [24] as:

$$m_a \approx 5.70\,\mu\mathrm{eV}\left(\frac{10^{12}\,\mathrm{GeV}}{f_a}\right).$$

For axions to be viable DM candidates, they must be stable, weakly interacting, and able to account for the observed DM density. With a sufficiently large f_a, axions are stable and interact very weakly with matter, meeting the criteria for cold DM [25]. Although axions are light, they can collectively act as a coherent field, behaving like cold DM. Their coupling with photons allows them to achieve the correct relic density through non-thermal production processes in the early Universe, such as photon-axion conversion or oscillation around the potential minimum [26].

Moreover, axions can decay into photon pairs, providing detectable signals. These decay processes, along with other interactions with SM particles, offer potential channels for experimental detection. Several experiments and observational strategies are being pursued to detect axions, including axion haloscopes and helioscopes, which search for axion-induced electromagnetic signals [27].

1.4.2 WIMPs

The thermal relic hypothesis posits that the DM we observe today is the remnant of a species that was in thermodynamical equilibrium with SM particles in the early Universe. Historically, this has led to the hypothesis that DM consists of Weakly Interacting Massive Particles (WIMPs), which as their name suggests, interact weakly with ordinary matter [28]. It is essential to note that the term WIMP does not pertain to a single, specific particle. Instead, it encompasses a broad class of hypothetical particles proposed within various theoretical frameworks.

During the radiation-dominated era of the early Universe, WIMPs were in thermal equilibrium with the primordial plasma. The number density n of WIMPs was maintained by a balance between their production and annihilation rates. This equilibrium was dependent on the mass-temperature ratio $x = m_\chi/T$, where m_χ is the mass of the WIMP and T is the temperature of the Universe.

While the temperature was higher than the mass of the WIMPs, their number density remained stable due to ongoing pair production and annihilation. However, as the Universe expanded and cooled, the temperature dropped below the WIMP mass. At this point, the production of WIMPs became inhibited, but their annihilation continued, leading to a decrease in their number density.

The decrease in the WIMP number density continued until the Universe's expansion rate (Hubble parameter) equaled the annihilation rate. This moment, known as the "freeze-out", marks the point beyond which the number of WIMPs remained approximately constant as the Universe continued to expand and cool.

In the context of an isotropic and homogeneous Universe, as described by the Friedmann-Lemaître-Robertson-Walker (FLRW) model [29], the number density evolution of WIMPs is given by:

$$\dot{n} + 3Hn = \langle \sigma v \rangle \left[(n_{\text{eq}})^2 - n^2 \right] . \tag{1.8}$$

Here:

- $\dot{n}$ is the time derivative of the number density.
- H is the Hubble parameter.
- $\langle \sigma v \rangle$ is the thermally averaged product of the annihilation cross-section σ and the relative velocity v.
- n_{eq} is the equilibrium number density, which follows either the Fermi-Dirac or Bose-Einstein distribution for relativistic particles (when $T \gg m$) or the Maxwell-Boltzmann distribution for non-relativistic particles (when $T \ll m$).

The required order of magnitude for $\langle \sigma v \rangle$ to solve Eq. 1.8 can be estimated by matching the DM density parameter Ω_χ with its observed value $\Omega_\chi h^2 = 0.1200 \pm 0.0012$ [8]. Consequently, regardless of the DM mass, the result yields:

$$\langle \sigma v \rangle \approx 10^{-26}\,\text{cm}^3/\text{s}. \tag{1.9}$$

It is noteworthy to observe that there is an inverse correlation between the annihilation cross-section and the relic density. WIMPs with lower interaction strengths (i.e. smaller σ) undergo freeze-out at higher temperatures, leading to an enhanced relic density. Due to the lack of precise knowledge regarding the type of interaction, couplings, mediator mass, and DM mass, various WIMP models can be constructed by adjusting the parameters involved in the estimation of the thermally averaged annihilation cross-section.

Early theoretical attempts situated DM within the electroweak framework. This rationale was motivated by noticing that when the mediator mass is set at a value comparable to the masses of electroweak gauge bosons of $\mathcal{O}(100\,\text{GeV})$ and the typical electroweak cross-section is considered, given in Eq. 1.10, the resulting cross-section is consistent with the prediction specified in Eq. 1.9.

$$\sigma \sim G_F^2 m_\chi^2 \propto \frac{g^4 m_\chi^2}{M^4}, \tag{1.10}$$

where $G_F \approx 10^{-5}\text{GeV}^{-2}$ is the Fermi constant in natural units. m_χ and M are the DM particle mass and the mediator mass respectively, while g is the coupling constant. If the WIMP mass is below a certain threshold, their abundance would be so high that the total energy density of the Universe would exceed the critical density, leading to an overclosed Universe. In this scenario, the Universe would eventually collapse under its own gravity rather than expand indefinitely. Under this framework, Lee and Weinberg imposes a lower limit on the WIMP mass at about 2 GeV to avoid overclosing the Universe [30].

This reasoning is particularly valid for WIMPs assumed to be fermions-like, for which the annihilation cross-section (σ) scales with the square of the WIMP

mass, m_χ^2. However, other lower limits for the WIMP mass are also plausible once the assumption on the mediator mass is relaxed. If the WIMP is a scalar particle, the relic density is influenced by its coupling to ordinary matter. There are two possible scenarios: either the bosonic WIMP interacts via as-yet-undiscovered fermions, potentially leading to an asymmetry between DM particles and antiparticles, or the interaction involves the exchange of a new neutral boson. In both cases, the connection between the DM density parameter (Ω_χ) and the annihilation cross-section (σ) shows only a weak dependence on the mass of the DM particle.

1.4.3 Sterile neutrinos

Sterile neutrinos are hypothesized extensions to the SM that can help explain several outstanding issues in particle physics, including the nature of DM. Unlike the three known types of neutrinos in the SM, which have left-handed chirality and interact via the weak force, sterile neutrinos do not interact through any of the SM forces except gravity, making them "sterile."

The discovery of neutrino oscillations, which implies that neutrinos have mass, contradicts the SM prediction of massless neutrinos. Introducing sterile neutrinos provides a mechanism to generate these masses via the seesaw mechanism. In this framework, a heavy sterile neutrino mixes slightly with the lighter SM neutrinos, resulting in one very heavy and one very light neutrino mass state. The tiny masses of the SM neutrinos are thus explained by the large mass of the sterile neutrino [31].

For sterile neutrinos to be viable DM candidates, they must satisfy several criteria. If their mass is greater than approximately $1\,\mathrm{keV/c^2}$ and their mixing angles with SM neutrinos are small, sterile neutrinos become non-relativistic early in the Universe's history, leading to a thermal relic density consistent with cold DM [32]. The extremely weak interaction between sterile neutrinos and SM particles ensures their stability over cosmic timescales, placing them in the category of Feebly Interacting Massive Particles (FIMPs).

The freeze-in mechanism is the favored process for achieving the correct relic density for sterile neutrinos [33]. In this scenario, the interaction cross-section between sterile neutrinos and SM particles is so low that sterile neutrinos never reach thermal equilibrium with the SM particles. Instead, their population slowly builds up through rare interactions as the Universe cools, eventually reaching the observed DM density.

The main experimental signature for sterile neutrinos is their decay into a monochromatic photon and a lighter SM neutrino. Detecting this signature remains an active area of research, with ongoing efforts in both astrophysical observations and laboratory experiments.

1.5 Detecting Dark Matter

In the preceding sections, I have outlined some of the cosmological observations that provide strong evidence supporting the *existence* of DM, as well as their implications for the particle physics properties of the constituents forming this dark sector. However, these constraints are relatively broad and can be satisfied by a variety of different particle species. I have introduced three of the most widely supported candidates in the field. For the remainder of this dissertation, I will concentrate only on WIMPs and explore their prospects for direct detection using terrestrial detectors. Goodman and Witten [34] were the first to suggest that WIMPs could be detected using a methodology analogous to that previously proposed by Drukier and Stodolsky [35] for the detection of solar and reactor neutrinos. The core principle of the proposed detection technique relies on WIMPs undergoing elastic scattering with atomic nuclei, resulting in a measurable nuclear recoil. This recoil serves as a direct, quantifiable signature of the WIMP-nucleus interaction, offering a means to experimentally observe this class of DM particles.

Before constructing an Earth-based experiment to detect WIMPs, it is essential to address several critical questions to estimate the expected signal rate. These include understanding the velocity distribution of the DM halo, determining the local mean density of DM around the Earth, and characterizing the specific velocities associated with the galaxy's motion and the Earth's movement through it. The first aspect necessitates theoretical assumptions and model construction, while the latter two are derived from astrophysical observations and measurements. In this section, I follow the standard reference in the direct detection field by Lewin and Smith [36].

1.5.1 The Standard Halo Model

The Standard Halo Model (SHM) provides a simplified framework essential for designing and interpreting DM detection experiments. It characterizes the velocity distribution of DM particles, the spatial density profile, and the overall mass and shape of the DM halo. Additionally, it estimates the local DM density near the Solar System and describes the gravitational effects of the halo on the galaxy's rotation curve and stellar dynamics.

This model postulates that the DM halo is an isothermal, isotropic, and non-rotating sphere. For a collection of particles in this configuration, the phase space distribution function $f(x, v, t)$ defined such that $f(x, v, t)\, d^3x\, d^3v$ gives the number of particles in an infinitesimal phase space volume $d^3x\, d^3v$ located at position x with speed v at time t. Such distribution function can be determined by solving the collisionless Boltzmann equation

$$\frac{df}{dt} = \frac{\partial f}{\partial t} + v \cdot \frac{\partial f}{\partial x} - \frac{\partial \Phi}{\partial x} \cdot \frac{\partial f}{\partial v} = 0, \tag{1.11}$$

where Φ denotes the Newtonian gravitational potential. For an isothermal spherical halo, the solution is given by Maxwell-Boltzmann statistics for an ideal gas at thermal equilibrium as:

$$f(x,v) = N \exp\left(-\frac{E}{k_B T}\right). \tag{1.12}$$

Here, N is a normalization constant and the mean kinetic energy of the ideal-gas particles is given by $E = \frac{1}{2} m_\chi v^2 + m_\chi \Phi(x)$. Then, the velocity distribution function can be obtained by integrating over the spatial coordinates x, as follows:

$$\begin{aligned} f(v) &= \int f(x,v)\, d^3x \\ &= N \exp\left(\frac{-m_\chi v^2}{2k_B T}\right) \int \exp\left(-m_\chi \Phi(x)\right)\, d^3x \\ &= N' \exp\left(-\frac{v^2}{2\sigma_v^2}\right). \end{aligned} \tag{1.13}$$

In this integral, the distribution of $\Phi(x)$ at the Earth's location is assumed to be constant and the spatial integral over that potential has been incorporated along with other constants into N'. Additionally, $\sigma_v^2 \equiv k_B T/m_\chi$ is resulting from a Maxwellian velocity distribution with radial velocity dispersion σ_v.

Furthermore, the DM halo is assumed to be a self-gravitating system, where the potential is generated by the DM density distribution itself. Therefore, $\Phi(x)$ is related to the density ρ by the Poisson's equation:

$$\frac{1}{r^2}\frac{d}{dr}\left(r^2 \frac{d\Phi}{dr}\right) = 4\pi G_N \rho. \tag{1.14}$$

Solving this continuity equation results in the halo density $\rho(r)$ as:

$$\rho(r) = \frac{\sigma_v^2}{2\pi G_N r^2}, \tag{1.15}$$

which provides the desired r^{-2} behavior to yield flat rotation curves, see [37] for more details.

In Eq. 1.13, the DM particle velocity is measured in the halo rest frame. Therefore in order to compute the observed velocity in an Earth-based detector, a transformation to the Earth frame is necessary, which can be expressed as:

$$\mathbf{v} \to \mathbf{v} + \mathbf{v}_E = \mathbf{v} + \Theta_0 + \mathbf{v}_\odot + \mathbf{v}_\oplus, \tag{1.16}$$

where Θ_0 is the local standard of rest (LSR) corresponding to the Galactic circular rotation at the Earth's radius R_0, $\mathbf{v}_\odot$ is the Sun's peculiar velocity, and

$\mathbf{v}_\oplus$ is the Earth's orbital velocity around the Sun. The SHM assumes that the Galactic rotation curve has reached its asymptotic value at $R_0 \approx 8.5$ kpc, giving the most probable velocity of WIMPs ($v_0 = \Theta_0 \approx 230$km/s). The Earth's motion around the Sun affects the kinetic energy of the incoming WIMPs annually, but the orbital velocity is usually averaged out over a year. Thus, the Solar peculiar velocity in the direction of Galactic rotation is typically the only contributing component, resulting in a yearly averaged $v_E = v_0 + v_\odot$.

We can define the differential WIMP number density (dn) for any general WIMP velocity distribution $f(\vec{v_\chi}, \vec{v_E})$, which is contingent upon both the WIMP velocity ($\vec{v_\chi}$) and the Earth's velocity relative to the galaxy, ($\vec{v_E} \approx 244 \pm 15$ km/s), with variations depending on the time of year, as:

$$dn = \frac{\eta_\chi}{k} f(\vec{v_\chi}, \vec{v_E})\, d^3\vec{v_\chi}. \tag{1.17}$$

Here k is the normalization absorbing all integration constants together, and it can be determined as:

$$k = \int_0^{2\pi} d\phi \int_{-1}^{1} d(\cos\theta) \int_{v_\mathrm{E}}^{v_\mathrm{esc}} f(\vec{v}, \vec{v_E}) v^2 dv, \quad \text{such that} \quad n_\chi \equiv \int dn. \tag{1.18}$$

In the last integration, we introduced v_esc, because the ideal Maxwellian velocity distribution in Eq. 1.13 extends to infinite velocities. However, in the physical scenario, WIMPs are gravitationally bound within the galaxy, necessitating that $|v_\chi + v_E| < v_\mathrm{esc}$, where v_esc is the escape velocity in the Milky Way assumed to be 600 km/s.

1.5.2 Event Rate Numerical Estimation

To estimate the rate of WIMPs in a given detector on Earth, several essential ingredients must be considered: the number of target nuclei present in the detector, the flux of WIMPs traversing the detector, the interaction probability between a WIMP and the target nuclei, and the detector's efficiency in registering the interaction. Assuming a 100 % detection efficiency, the most basic expression for the rate of DM interactions per unit mass of the detector can be written as:

$$R = \frac{N_A}{A} \eta_\chi \sigma \langle v \rangle, \tag{1.19}$$

where N_A/A represents the number of nuclei per unit mass of material, with N_A being Avogadro's number and A the atomic mass of the target medium. σ denotes the WIMP-nucleus elastic scattering cross section, which will be discussed in Sec. 1.5.3. While η_χ represents the WIMPs number density, and $\langle v \rangle$ is the average WIMP velocity.

It is insightful to consider calculating the simplest case of $v_E = 0$ and $v_{\rm esc} = \infty$. Then, we can incorporate the actual values of these parameters as separate factors that limit the rate. Consequently, we can define R_0 to be the event per unit mass in this case, and the normalization in Eq. 1.18 is commonly labeled as k_0, becomes simply:

$$k_0 = \int_0^{2\pi} d\phi \int_{-1}^{1} d(\cos\theta) \int_0^{\infty} v^2 \exp\left(-\frac{v^2}{v_0^2}\right) dv = \left(\pi v_0^2\right)^{3/2}. \tag{1.20}$$

Hence, the mean WIMP velocity employing the Maxwellian distribution, given in Eq. 1.13, can be written as:

$$\langle v \rangle = \frac{1}{k_0} \int_0^{\infty} v f(\vec{v})\, d^3v. \tag{1.21}$$

Switching to spherical coordinates, $d^3v = 4\pi v^2\, dv$, and using the substitution $u = v^2/v_0^2$, $du = 2v/v_0^2\, dv$, the integral becomes:

$$\begin{aligned} \langle v \rangle &= 4\pi \left(\frac{1}{\pi v_0^2}\right)^{3/2} \int_0^{\infty} v^3 \exp\left(-\frac{v^2}{v_0^2}\right) dv \\ &= 4\pi \left(\frac{1}{\pi v_0^2}\right)^{3/2} \frac{v_0^4}{2} \int_0^{\infty} u \exp(-u) \frac{du}{v_0} = 4\pi \left(\frac{1}{\pi v_0^2}\right)^{3/2} \frac{v_0^4}{2} \frac{1}{v_0} \\ &= 4\pi \cdot \frac{1}{\pi^{3/2}} \cdot \frac{v_0}{2} = \frac{2}{\sqrt{\pi}} v_0. \end{aligned} \tag{1.22}$$

By substituting in Eq. 1.19, the overall interaction rate can be represented as a function of WIMP energy in its simplest form:

$$R_0 = \frac{2}{\sqrt{\pi}} \frac{N_A}{A} \eta_\chi \sigma_0 v_0. \tag{1.23}$$

To gain a quantitative understanding of the event rate described by this formula, we can perform a numerical analysis. Following the approach of Lewin and Smith [36], we normalize the parameters to their typical values. This involves setting the WIMP number density (η_χ) to ρ_χ/m_χ and incorporating the relevant physical constants. The local WIMP density (ρ_χ), typically considered to lie within the range of $0.3 - 0.7\,\mathrm{GeV/cm^3}$, is commonly accepted to be approximately $0.4\,\mathrm{GeV/cm^3}$. m_χ and $m_{\rm T}$ are the WIMP and target nucleus masses, respectively, in units of GeV. With the approximation that $m_T \approx 0.932\,A$, we obtain:

$$R_0 = \frac{503}{m_\chi m_{\rm T}} \left(\frac{\sigma_0}{1\,\mathrm{pb}}\right) \left(\frac{\rho_\chi}{0.4\,\mathrm{GeV/cm^3}}\right) \left(\frac{v_0}{230\,\mathrm{km/s}}\right) \mathrm{event/kg/day}. \tag{1.24}$$

However, what is typically measured in direct detection experiments is the nuclear recoil energy of the target rather than the WIMP energy. Therefore,

it is more practical to derive the differential recoil energy spectrum.

This follows from the kinematics of two-body elastic scattering, fully derived in Appendix A. It relates the recoil energy of the target nucleus (E_{rec}) to the WIMP's initial energy (E_χ) and the scattering angle (θ) at which the WIMP emerges from the collision, as such:

$$E_{rec} = \frac{E_\chi r}{2}(1-\cos\theta), \quad \text{with} \quad r = 4\mu \equiv \frac{4m_\chi m_T}{(m_\chi + m_T)^2}. \tag{1.25}$$

Here, r is a dimensionless kinematic factor associated with the reduced mass of the WIMP-nucleus system (μ), representing the maximum fractional energy transfer possible in the interaction. Assuming an isotropic scattering (i.e. uniform in $\cos\theta$), the recoil energy becomes uniformly distributed in the 0 - E_{rec} range in the center-of-mass frame. Consequently, averaging over the differential incident-energy spectrum E_χ would yield the differential recoil-energy spectrum as:

$$\begin{aligned}
\frac{dR}{dE_{rec}} &= \int_{E_{\min}}^{E_{\max}} \frac{1}{E_\chi r} dR(E_\chi) \\
&= \frac{1}{E_0 r}\int_{v_{\min}}^{v_{\max}} \frac{v_0^2}{v_\chi^2} dR(v_\chi) = \frac{\sqrt{\pi}v_0 k}{2}\frac{R_0}{E_0 r}\int_{v_{\min}}^{v_{\max}} \frac{1}{k}\frac{f(\vec{v_\chi},\vec{v_E})}{v_\chi} d^3\vec{v_\chi} \\
&= \frac{N_A}{A}\frac{\rho_\chi}{m_\chi}\frac{\sigma_0 v_0^2}{E_0 r}\underbrace{\int_{v_{\min}}^{v_{\max}} \frac{1}{k}\frac{f(\vec{v_\chi},\vec{v_E})}{v_\chi} d^3\vec{v_\chi}}_{I}.
\end{aligned} \tag{1.26}$$

We can determine $v_{\min}$ by considering the smallest WIMP energy which can result in a recoil energy, E_{rec}. This corresponds to a head-on scattering, with $\theta = \pi$ in Eq. 1.25, and thus $E_{\min} = E_{rec}/r$. This yields:

$$v_{\min} = \sqrt{\frac{2E_{\min}}{m_\chi}} = \sqrt{\frac{E_{rec}}{E_0 r}} v_0, \quad \text{with} \quad E_0 = \frac{1}{2}m_\chi v_0^2. \tag{1.27}$$

To evaluate the velocity integral (I) in Eq. 1.26, we, first, derive the normalization factor, k, from Eq. 1.18 as follows:

$$\begin{aligned}
k &= \int_0^{2\pi} d\phi \int_{-1}^{1} d(\cos\theta) \int_0^{v_{\text{esc}}} \exp\left(-\frac{|\vec{v_\chi} + \vec{v_E}|^2}{v_0^2}\right) v_\chi^2 dv \\
&= \left(\pi v_0^2\right)^{3/2}\left[\text{erf}(z) - \frac{2}{\sqrt{\pi}} z e^{-z^2}\right] \\
&\equiv k_0\left[\text{erf}(z) - \frac{2}{\sqrt{\pi}} z e^{-z^2}\right],
\end{aligned} \tag{1.28}$$

where $z = v_{\text{esc}}/v_0$.

Then, since the pure Maxwellian velocity distribution theoretically extends to infinite velocities, but physically the distribution is truncated at the Galactic escape velocity $v_{\rm esc}$. Care must be taken due to the Earth's motion, leading to the condition:

$$|\vec{v_\chi} + \vec{v_E}| \leq v_{\rm esc}, \tag{1.29}$$

which results in:

$$v_{\rm max}(\cos\theta) = \sqrt{v_{\rm esc}^2 - v_E^2(1-\cos^2\theta)} - v_E\cos\theta. \tag{1.30}$$

Here, θ is the scattering angle in the Galactic rest frame. The integral (I) then becomes:

$$I = \frac{1}{k}\int_0^{2\pi} d\phi \int_{-1}^{1}\int_{v_{\rm min}}^{v_{\rm max}(\cos\theta)} v_\chi \exp\left(-\frac{v_\chi^2 + 2v_\chi v_E\cos\theta + v_E^2}{v_0^2}\right) dv_\chi\, d(\cos\theta). \tag{1.31}$$

There are three distinct cases for the relationship between $v_{\rm min}$ and $v_{\rm max}(\cos\theta)$ which lead to different results, more details on the derivation can be found in [38]:

$$I = \frac{k_0}{k}\frac{1}{2yv_0}\begin{cases} \mathrm{erf}(x+y) - \mathrm{erf}(x-y) - \frac{4y}{\sqrt{\pi}}e^{-z^2} & 0 < x < z-y, \\ \mathrm{erf}(z) - \mathrm{erf}(x-y) - \frac{2}{\sqrt{\pi}}(y+z-x)e^{-z^2} & z-y < x < y+z, \\ 0 & y+z < x, \end{cases} \tag{1.32}$$

where $x = v_{\rm min}/v_0$, $y = v_E/v_0$, and z is defined above. The last case sets the rate to zero to avoid nonphysical negative results.

The method outlined above abruptly truncates the Maxwellian distribution, which is equivalent to multiplying Eq. 1.13 with a Heaviside step function $\Theta(v_{\rm esc} - v)$. This approach is likely unphysical. Alternative methods smoothly transition the distribution to zero at $v = v_{\rm esc}$. Two examples are $f(v) = f_{\rm SHM}(v)\cdot e^{-z^2}$ [39] and $f(v) = f_{\rm SHM}(v)\cdot(1-e^{-z^2})$ [40], where $f_{\rm SHM}(v)$ is the Maxwellian distribution from Eq. 1.13. The value of k must be recalculated for each case using Eq. 1.18 with the specified distribution function.

1.5.3 Particle and Nuclear Physics Input

Up to this point, we have assumed that the WIMP-nucleus elastic scattering cross section is constant (σ_0), which appears in Eq. 1.26. However, in practice, it depends on the nuclear structure of the target and the momentum transferred (q) in the collision. While the nature of DM particles is yet unknown, a generic approach can be performed by employing the Fermi's Golden rule

and separate the energy dependence of the differential cross section into an independent term (σ) and another term, namely the form factor F^2, which includes the entire dependence on the momentum transfer.

Furthermore, the initial assumption in the previous sections is that the target nucleus is small relative to the De Broglie wavelength corresponding to the momentum transfer. This can be approximated for a WIMP of mass $100\,\mathrm{GeV/c^2}$ and using the local WIMP velocity of $\approx 230\,\mathrm{km/s}$, yielding assuming full momentum transfer:

$$\lambda_{DM} = \frac{h}{p} \approx 16 \text{ fm}. \tag{1.33}$$

However, for instance, the diameter of a xenon nucleus is approximately 13 fm, which is comparable to the De Broglie wavelength, resulting in significant decoherence effects. Therefore, a form factor correction need to be applied to account for the scattering decoherence off the target nucleus. Similarly, an argon nucleus, with a smaller diameter of around 7 fm, also requires a form factor correction, although the effects may be less pronounced than for xenon.

In this subsection, we will separately present the WIMP-nucleon cross section and the form factor correction for both spin-independent (SI) and spin-dependent (SD) interactions. Our discussion is based on the comprehensive reviews by Lewin and Smith [36], Jungman, Kamionkowski, and [41], and Schnee [42]. The goal is to provide an overarching outline of the essential components without delving into excessive details beyond the scope of this thesis.

Spin-independent WIMP-nucleus interaction

In WIMP detection experiments, the primary quantity measured is the WIMP-nucleus cross section. However, to facilitate comparison across different experiments, the WIMP-nucleon cross section is more commonly used within the direct detection community. This standardization arises because the WIMP-nucleus cross section varies with the atomic mass number of the target material; for example, it is higher for xenon than for argon and germanium due to xenon's larger atomic mass.

The SI cross section is parameterised as a function of the target nature as:

$$\sigma^{SI} = \frac{4\mu^2}{\pi}\left(Z\frac{f_p}{f_n} + (A - Z)\right)^2, \tag{1.34}$$

where μ is the reduced mass of the WIMP-nucleus system, while A and Z denote the atomic mass and number of the target nucleus, respectively. The parameters f_p and f_n correspond to the effective WIMP coupling to protons

and neutrons within the target nucleus, respectively, which are typically assumed to adhere to an isospin symmetry (i.e. $f_p = f_n$). This approximation simplifies Eq. 1.34 and allows us to relate the WIMP-nucleus σ^{SI} and the WIMP-nucleon σ_n^{SI} cross sections as follows:

$$\sigma^{SI} \approx \frac{4\mu^2}{\pi} A^2 f_n^2 \equiv \sigma_n^{SI} \frac{\mu^2}{\mu_n^2} A^2. \tag{1.35}$$

Here, the last equality resulted from defining the SI cross section on a single nucleon $\sigma_n^{SI} = 4\mu_n^2 f_n^2/\pi$ and enabled us to write explicitly the ratio μ^2/μ_n^2 which accounts for the different kinematic phase-space factors between the WIMP-nucleus and WIMP-nucleon systems. Eq. 1.35 shows that the σ^{SI} is enhanced by a factor A^2, favouring heavy nuclei as a target. This is consistent with the expectation of a coherent scattering where the contribution from all the nucleons are summed up together.

However, as mentioned before, a form factor correction needs to be applied to account for the fact that with larger momentum transfers the nucleus appears less and less homogeneous and the interaction loses coherence. In SI interactions, the form factor is evaluated as the Fourier transformation of the Woods-Saxon potential, represented as:

$$F_{SI}^2 = \left(3 \frac{\sin(q\, r_n) - q\, r_n \cos(q\, r_n)}{(q\, r_n)^3} \right)^2 e^{-q^2 s^2}. \tag{1.36}$$

Here, the parameters r_n and s are originate from Fermi's approximation of the nuclear structure, assuming spherical symmetry with a radius $r_n \approx 1.14\, A^{1/3}$ fm and a skin thickness $s \approx 0.9$ fm. The skin thickness refers to the radial distance over which the nuclear density decreases from 90 % to 10 % of its central value [42].

Figure 1.4 shows the form factor corrections for a few different target nuclei along with their implications on the final differential signal rate. Due to the relatively large radius of the xenon nucleus, approximately 6 fm, the form factor for xenon declines rapidly. This decline results in a 95 % reduction in the WIMP-nucleus cross section at 50 keV. In contrast, for germanium and argon, the form factor correction is less significant due to their smaller nuclear radii of approximately 5 fm and 4 fm, respectively. At 50 keV, the form factor correction reduces the WIMP-nucleus cross section by 60 % for germanium and 33 % for argon. The first minimum, where scattering coherence is entirely lost, occurs at recoil energies around 90 keV, 250 keV, and 700 keV for xenon, germanium, and argon, respectively.

The differential event rates, which scale with A^2 decrease when the form factor correction is considered for all target materials. This suppression is energy dependent due to the corresponding decrease in the De Broglie wavelength, as described by Eq. 1.33, which is conversely related to the momentum

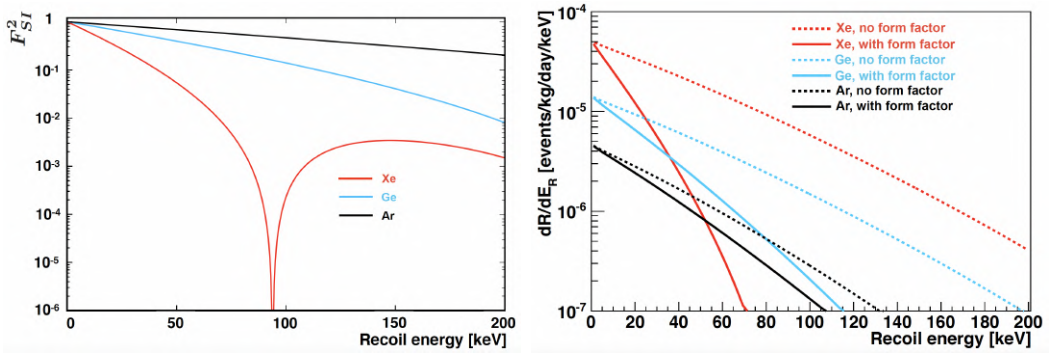

Figure 1.4: *On the Left*: The Form factors for target materials commonly employed in direct detection experiments. *On the Right*: The Differential event rates calculated for these targets, assuming a WIMP-nucleon cross section of approximately 10^{-45}cm^2. The *dashed lines* represent calculations without form factor corrections, while the *solid lines* include the form factor effects. Figures are taken from [43].

transferred that can be expressed as $q = \sqrt{2mE_{rec}}$. The loss of scattering coherence diminishes the benefit of utilizing a target with a high atomic mass (A) for higher recoil energies. Consequently, the differential event rate for xenon falls below that of germanium or argon for recoil energies exceeding approximately 35 keV or 55 keV, respectively.

Spin-dependent WIMP-nucleus interaction

The SD cross section can be written as:

$$\sigma^{SD} = \frac{32}{\pi}\mu^2 G_F^2 \frac{J+1}{J}[a_p\langle S_p\rangle + a_n\langle S_n\rangle]^2, \tag{1.37}$$

where $\langle S_p\rangle$ and $\langle S_n\rangle$ are the expectation values of total proton and neutron spin operators determined using detailed nuclear model calculations in the limit of zero momentum transfer, respectively. G_F denotes the Fermi coupling constant, while J is the total angular momentum of the nucleus.

As mentioned in the SI case, direct detection experiments typically report the cross section for WIMP interactions with individual nucleons. Therefore, it is useful to relate the SD WIMP-nucleon cross section to the SD WIMP-nucleus cross section, expressed in Eq. 1.37. However, the scenario for SD interactions is quite different. Firstly, the SD WIMP couplings to protons a_p and neutrons a_n can not be considered the same and frequently they cancel each other out. Therefore, it is crucial to report limits on the SD interaction with protons separately from those with neutrons, assuming the negligible influence of the other interaction in each case. This can be done for the case where $\langle S_p\rangle = \langle S_n\rangle = J = 1/2$, yielding:

$$\begin{aligned} \sigma_p^{SD} &= \frac{24}{\pi} G_F^2 \mu_p^2 a_p^2, \qquad \text{and} \qquad \sigma_n^{SD} = \frac{24}{\pi} G_F^2 \mu_n^2 a_n^2, \\ \sigma_p^{SD} &= \frac{3}{4} \frac{J}{J+1} \frac{\mu_p^2}{\mu^2} \frac{\sigma^{SD}}{\langle S_p \rangle^2}, \qquad \text{and} \qquad \sigma_n^{SD} = \frac{3}{4} \frac{J}{J+1} \frac{\mu_n^2}{\mu^2} \frac{\sigma^{SD}}{\langle S_n \rangle^2}. \end{aligned} \tag{1.38}$$

Additionally, unlike the coherent interaction on the nucleus that leads to a SI cross section scaling with A^2 due to the additive contributions of each nucleon within the matrix element, the SD contributions from nucleons with opposite spins interfere destructively. Therefore, the total SD cross section is contingent upon the net spin of the nucleus. In other words, nuclei with even numbers of protons (or neutrons) exhibit nearly zero net proton (or neutron) spin, making them essentially insensitive to SD interactions.

Consequently, argon, which has even numbers of both protons and neutrons in all its significant isotopes, is effectively insensitive to SD interactions. Many other WIMP targets, such as germanium, silicon, and xenon, have even numbers of protons and therefore lack sensitivity to SD interactions involving protons. Only certain isotopes of these target materials, representing a fraction of the detector's active mass, have sensitivity to SD interactions involving neutrons.

The form factor for SD interactions incorporates corrections arising from the spin structure function, making its calculation significantly more complex. This complexity stems from the necessity to account for the complete nuclear shell model and empirical parameterizations of the residual nuclear potential. Nonetheless, a first-order approximation provides a simplified yet insightful representation, and it can be expressed as:

$$F_{SD}^2 \approx \left(\frac{sin(q\, r_n)}{q\, r_n} \right)^2. \tag{1.39}$$

1.5.4 WIMPs: Direct Detection Signature

The primary signature for the direct detection of WIMPs is the nuclear recoil resulting from elastic scattering between WIMPs and target nuclei. This recoil serves as a critical experimental observable for probing the particle properties of DM.

In this section, the core principles governing the identification of this signal by various direct detection experiments have been explained. Beginning with the astrophysical component, detailed in Sec. 1.5.1, where the local mean density of the DM halo (ρ_χ) is determined and the velocity distribution of the DM halo, expressed as integral (I), is derived and expressed in Eq. 1.32. In Sec. 1.5.3, it was demonstrated that the WIMP-nucleus cross section can

be decomposed into SI and SD components. These components are further modulated by the momentum transfer dependence encapsulated within the nuclear form factor. Incorporating these components together, the differential rate of elastic WIMP scattering events in a terrestrial detector can be formulated from Eq. 1.26, distinguishing the contributions from nuclear and particle physics from those of astrophysics and the detector characteristics as follows:

$$\frac{dR}{dE_{rec}} = \underbrace{\frac{N_A m_T}{2 m_\chi \mu^2}}_{\text{Detector}} \underbrace{\left[\sigma^{SI} F_{SI}^2(E_{rec}) + \sigma^{SD} F_{SD}^2(E_{rec})\right]}_{\text{Particle and Nuclear}} \underbrace{\rho_\chi I}_{\text{Astro}} . \tag{1.40}$$

Ongoing experimental efforts, employing increasingly sensitive detection technologies and diverse target materials, continue to refine the precision of measurements, thereby constraining the parameter space of viable WIMP models. Detailed reviews of recent advancements can be found in [44, 45], while the latest results from major experiments, such as DarkSide, DEAP, LZ, LUX, XENON, SuperCDMS, PandaX and Pico are reported in [46, 47, 48, 49, 50, 51, 52].

CHAPTER II

Noble Liquid Detectors

Over the past three decades, liquefied noble gases have emerged as highly promising materials for rare-event detection, particularly in the context of dark matter searches, due to their exceptional sensitivity and scalability. Argon and xenon, in particular, have demonstrated remarkable performance characteristics that are crucial for achieving the low detection thresholds required in these searches. Their unique physical properties, such as high scintillation and ionization yields, combined with the ability to achieve ultra-low background conditions, make them highly effective for detecting low-energy recoils of $\mathcal{O}(1\,\mathrm{keV})$.

The scintillation light emitted by liquefied noble gases is in the vacuum ultraviolet (VUV) spectrum, with argon and xenon emitting at wavelengths of approximately 128 nm and 178 nm, respectively. This VUV emission is a direct consequence of either their excitation or their ionization followed by recombination. The effective work functions for xenon and argon, determined experimentally, are 13.8 eV and 19.5 eV, respectively [53]. Consequently, these gases exhibit photon yields of up to 73 photons/keV for xenon and 51 photons/keV for argon, further enhancing their utility in detecting rare events.

In this chapter, an overview of the scintillation and ionization mechanisms specific to liquefied noble gases, with a particular focus on liquid argon (LAr) will be presented. Then we discuss the operational principles of detectors that leverage these properties, following the reviews of Aprile et al. [54] and Chepel et al. [55] to present a coherent review of current advancements and methodologies in the field.

2.1 Liquid Argon Luminescence

Luminescence in liquefied noble gases results from the de-excitation of their unstable excited molecules (excimers), which decay radiatively through the transition to the ground state emitting vacuum-ultraviolet (VUV) scintillation light. This dissertation focuses on LAr, though the same principles apply to xenon and other liquefied noble gases due to their similar scintillation mechanisms. Excimer formation is initiated by the deposition of energy due to a particle interaction in LAr and occurs via two primary processes: excitation or ionization.

In the case of excitation, the deposited energy goes to the atomic electrons promoting one valence electron to a higher orbital, thereby generating an excited atom (exciton), denoted as Ar^*. This exciton typically pairs with a nearby ground-state atom to form an excimer, indicated as Ar_2^*. This excimer formation, known as "*exciton self-trapping*", occurs on the order of picoseconds. The excimer subsequently decays radiatively to the unbound ground state on the order of nanoseconds, emitting a 128 nm ultraviolet photon, represented as $h\nu$. These processes can be described by the following set of reactions:

$$\begin{aligned} Ar + X &\rightarrow Ar^* + X && \text{Impact excitation} \\ Ar^* + Ar &\rightarrow Ar_2^* && \text{Excimer formation} \\ Ar_2^* &\rightarrow 2Ar + h\nu && \text{De-excitation} \end{aligned} \tag{2.1}$$

In the case of ionization, the deposited energy is sufficient to liberate an electron from the argon atom, producing an electron-ion pair ($Ar^+ + e^-$). The argon ion tends to bind with a neutral argon atom in the ground state, forming a charged dimer denoted as Ar_2^+. The free electron, liberated by ionization, is then captured by the charged dimer, splitting it into a doubly excited atom (Ar^{**}) and a ground-state atom. The doubly excited atom dissipates some energy as heat and non-radiatively decays to a single excited state. This process is known as recombination which results in an exciton that binds with a nearby ground-state atom to form an excimer, which subsequently de-excites, releasing an ultraviolet photon. This scenario can be summarized by the following reactions:

$$\begin{aligned} Ar + X &\rightarrow Ar^+ + e^- + X && \text{Ionization} \\ Ar^+ + Ar &\rightarrow Ar_2^+ && \\ Ar_2^+ + e^- &\rightarrow Ar^{**} + Ar && \text{Recombination} \\ Ar^{**} &\rightarrow Ar^* + \text{heat} && \\ Ar^* + Ar &\rightarrow Ar_2^* && \text{Excimer formation} \\ Ar_2^* &\rightarrow 2Ar + h\nu && \text{De-excitation} \end{aligned} \tag{2.2}$$

There exist competing processes that enable argon excitons to decay non-radiatively, thereby preventing the formation of excimers and consequently reducing the scintillation light yield. The rates of these processes scale with the square of the exciton density, leading to greater suppression at higher densities. These processes are collectively known as "*electronic quenching*" and include bi-excitonic quenching, photoionization, and the Penning process. These mechanisms can be described as follows:

$$\begin{aligned} \mathrm{Ar}^* + \mathrm{Ar}^* &\rightarrow \mathrm{Ar} + \mathrm{Ar}^+ + e^- && \text{Bi-excitonic collisions} \\ \mathrm{Ar}^* + \mathrm{Ar}_2^* &\rightarrow \mathrm{Ar} + \mathrm{Ar}_2^+ + e^- && \text{Photo-ionization} \\ \mathrm{Ar}_2^* + \mathrm{Ar}_2^* &\rightarrow 2\mathrm{Ar} + \mathrm{Ar}_2^+ + e^- && \text{Penning process} \end{aligned} \tag{2.3}$$

2.2 Particle Discrimination in Liquid Argon

Excimers can be produced in either a singlet state ($^1\Sigma_u^+$) or a triplet state ($^3\Sigma_u^+$). The decay of the singlet state is an allowed transition with a lifetime of 6.7 ns, whereas the decay of the triplet state has a strong spin-orbit coupling in Ar_2, resulting in a much longer lifetime of up to 1600 ns [56].

The scintillation light emitted cannot be absorbed in LAr because the energy of photons is too low to be able to excite or ionize the ground state atoms. Thus, LAr is effectively transparent to its own scintillation emission. Furthermore, the proportion of excimers produced in the singlet and triplet states is determined by the linear energy transfer (LET) of the incident radiation. Higher energy dissipation per unit track length leads to the formation of more singlet excimers. Consequently, electromagnetic interactions primarily excite the argon excimer triplet state, while nuclear recoils predominantly excite the singlet state. This distinction is fundamental to the background suppression techniques employed in LAr-based experiments.

2.3 Particle Interactions in Liquid Argon

The energy deposition mentioned in Sec. 2.1, which causes the excimer formation due to either excitation or ionization, occurs as a result of a particle interaction in LAr. As an incoming particle traverses through an LAr medium, it can either scatter off the nuclei or the electrons of the argon atoms depending on the nature of the particle. Nuclear Recoils (NRs) predominantly result from interactions with α particles, neutrons, and expected as well from WIMPs, while Electron Recoils (ERs) are mainly caused by γ-rays, β particles, and muons.

In either case, the energy of the incident particle can induce atomic motion, raise an electron to a higher energy state, resulting in an exciton (Ar^*), or liberating an electron from the atom, producing an electron-ion pair ($Ar^+ + e^-$).

These liberated electrons may undergo recombination, resulting in the formation of excitons, as described in Eq. 2.2. These excitons, along with others directly caused by excitation, will then rapidly relax, as outlined in Eq. 2.1, leading to the emission of scintillation photons, commonly referred to as S1.

In the presence of an electric field, a fraction of the ionization electrons escape recombination and drift along the field lines and can be extracted into a gaseous phase above the liquid, where the excitation and subsequent de-excitation of these gas atoms result in a secondary scintillation, known as S2.

While nearly all energy deposited from ERs converts to observable signals (i.e. S1 and S2), more than half the energy from NRs goes into atomic motion or dissipates as heat, which is undetectable by scintillation detectors [57].

2.3.1 Nuclear Quenching Factor

Lindhard's theory [57] provides a framework for quantifying the total energy loss experienced by a recoiling nucleus (E_{rec}) within a noble liquid medium. According to Lindhard, this energy loss can be expressed as the sum of the electronic stopping power, $\eta(E_{\text{rec}})$, and the nuclear stopping power, $\nu(E_{\text{rec}})$, as follows:

$$\begin{aligned} E_{\text{rec}} &= \eta(E_{\text{rec}}) + \nu(E_{\text{rec}}) \\ \left(\frac{dE}{dx}\right)_{\text{Total}} &= \left(\frac{dE}{dx}\right)_{\text{Electronic}} + \left(\frac{dE}{dx}\right)_{\text{Nuclear}} . \end{aligned} \tag{2.4}$$

Here, η denotes the energy lost per unit distance to excite or ionize the surrounding atoms, which becomes dominant at higher recoil energies. In contrast, ν is defined as the energy loss per unit distance due to the atomic collisions along the recoil path, contributing to the kinetic energy, or thermal motion, of the medium's atoms without causing excitation or ionization. The nuclear stopping power, ν, is particularly relevant within lower energy ranges. Therefore, it plays a pivotal role in the dissipation of the recoiling nucleus's energy associated with WIMP-nucleus elastic scattering.

Given that only the electronic stopping power contributes to the observable signal, it is advantageous to define the reduction factor of the visible light output, f_n, which accounts for the energy lost to thermal motion. This factor can be expressed as:

$$\begin{aligned} f_n(E_{\text{rec}}) \equiv \frac{\eta(E_{\text{rec}})}{E_{\text{rec}}} &= \frac{\eta(E_{\text{rec}})}{\eta(E_{\text{rec}}) + \nu(E_{\text{rec}})} \\ &= \frac{\int_0^{E_{\text{rec}}} \left(\frac{dE}{dx}\right)_{\text{Electronic}} dE}{\int_0^{E_{\text{rec}}} \left(\frac{dE}{dx}\right)_{\text{Electronic}} dE + \int_0^{E_{\text{rec}}} \left(\frac{dE}{dx}\right)_{\text{Nuclear}} dE}. \end{aligned} \tag{2.5}$$

To evaluate f_n as a function of recoil energy, these integrals must be computed for each possible recoil energy value using the formula given in [57]:

$$f_n = \frac{\kappa g(\epsilon)}{1 + \kappa g(\epsilon)}, \tag{2.6}$$

with κ and ϵ can be determined for a given type of atom target with its corresponding atomic number Z and mass number A, while g is a function of ϵ. These factors can be expressed as:

$$\kappa = 0.133 Z^{2/3} A^{-1/2}, \qquad g(\epsilon) = 3\epsilon^{0.15} + 0.7\epsilon^{0.6} + \epsilon, \qquad \epsilon = 11.5 \left(\frac{E_{\text{rec}}}{\text{keV}} \right) Z^{-7/3}.$$

2.3.2 Electronic Quenching Factor

As discussed in Sec. 2.1, there are several mechanisms (Eq. 2.3) that can affect excimer formation, thereby reducing scintillation photon yield. The likelihood of these processes occurring is influenced by the density of free excitons generated, which is directly linked to ionization density. The Birks saturation law [58] effectively characterizes the relationship between scintillation quenching and ionization density by utilizing the correlation between the electronic stopping power and ion density. The production of excitons leads to a saturation in scintillation, which becomes increasingly pronounced as the collision exciton probability κ in Eq. 2.6 increases. In this context, "saturation" refers to the limitation in the scintillation yield due to competing processes that arise with increasing ionization density, which ultimately reduces the scintillation photon yield (S). This suppression of scintillation per unit length ($\frac{dS}{dx}$) can be expressed as:

$$\frac{dS}{dx} = \frac{A \left(\frac{dE}{dx} \right)}{1 + \kappa B \left(\frac{dE}{dx} \right)}, \tag{2.7}$$

where the values of A and κB can be determined experimentally. The fraction of scintillation light that remains after being suppressed by ionization density is given by Birks Law [58]:

$$f_l = \frac{1}{1 + \kappa B \left(\frac{dE}{dx} \right)}, \tag{2.8}$$

For LAr, κB was measured to be 7.4×10^{-4} g/MeV/cm^2, more details in [59].

2.3.3 Total Energy Quenching

The Mei model [59] provides a comprehensive framework for understanding the total energy loss in a recoil in liquid argon and, more generally, in any noble liquid. It incorporates both contributions discussed above, namely:

- **Nuclear quenching** (f_n), which accounts for the portion of the recoil energy that is dissipated into the thermal motion of the atomic nuclei rather than contributing to scintillation. Therefore, it depends on the length of the recoil track, and it is described quantitatively by Lindhard Theory.

- **Electronic quenching** (f_l), which addresses the processes in Eq. 2.3 that restrain excimer formation and in turns suppress the light yield. The Birks saturation Law models how the ionization density—an indicator of the energy deposited per unit length—affects the saturation of light yield. At higher ionization densities, recombination processes become less efficient, leading to increased quenching.

While these quenching effects are minimal for ERs, they become significant in the context of NRs, which are relevant for dark matter detection. Since nuclear and electronic quenching are independent, the total scintillation efficiency can be expressed as the product of the two factors:

$$\mathcal{L} = f_n \times f_l. \tag{2.9}$$

Figure 2.1, illustrates these quenching factors: the left panel shows the nuclear quenching factor as derived from the Lindhard model (Eq. 2.6), and the right panel displays the global quenching factor, representing the total scintillation efficiency for NRs as expressed in Eq. 2.9.

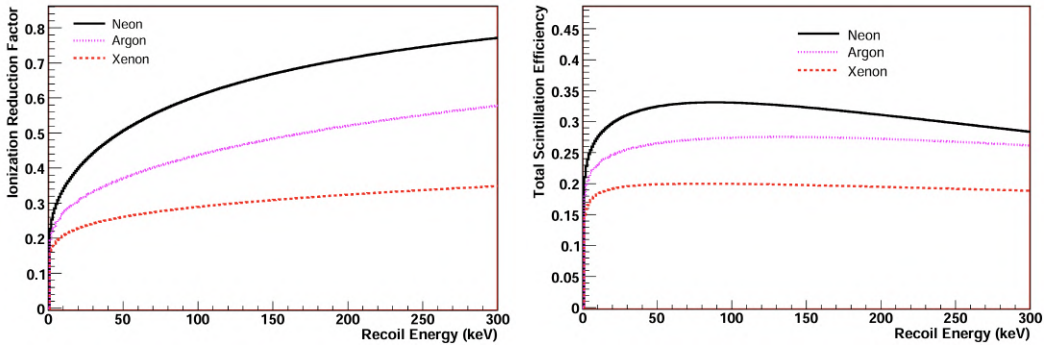

Figure 2.1: *Left*: The ionization energy suppression factor f_n based on Lindhard theory plotted against recoil energy. *Right*: The overall scintillation efficiency $\mathcal{L}$ for NRs as a function of recoil energy. The figures, sourced from [59], depict data for liquid neon (*black*), liquid argon (*red*), and liquid xenon (*magenta*).

There is a discrepancy in the scintillation light output relative to the energy deposited due to whether the interaction is caused by NR or ER. Therefore, when discussing the intensity of the scintillation signal, it is standard practice to express it using the units "keV electron equivalent" (keV_{ee}), which represents

the amount of energy an electron would need to produce the same amount of scintillation light. In contrast, keV$_{nr}$ refers to the recoil energy associated with an NR event. The necessity of defining these distinct energy scales arises from the fact that electrons, γ-rays, and β-particles interactions generally experience minimal quenching compared to interactions inducing NRs. Consequently, these two units are related through the global quenching factor $\mathcal{L}$ as follows:

$$E_{\text{rec}}\,[\text{keV}_{ee}] = \mathcal{L}\,E_{\text{rec}}\,[\text{keV}_{nr}]. \tag{2.10}$$

2.4 Signal Production in Liquid Argon

The previous discussion has established that particle interactions in liquefied noble gases can produce both a scintillation light signal—comprising photons generated through excitation and recombination—and a charge signal from ionized electrons that escape recombination. In this section, I will briefly review the particle interactions in terms of the resulting observable signals.

The generation of an observable signal starts with the deposition of energy E which, as previously discussed, results in different numbers of quanta N_q depending on whether the interaction is a NR or an ER. Therefore, they are referred to as E_{ER} or E_{NR} to indicate the interaction type. The average number of quanta is the sum of the number of excitons N_{ex} and ions N_i, and it can be expressed in both cases as follows:

$$N_q = N_{ex} + N_i = \frac{E_{\text{ER}}}{W}, \quad \text{and} \quad N_q = N_{ex} + N_i = \frac{E_{\text{NR}}\mathcal{L}}{W}. \tag{2.11}$$

Here, $\mathcal{L}$ is the global quenching factor discussed in Sec. 2.3.3. W indicates the effective work function of LAr that represent the average energy required to produce a quantum, whether through scintillation or ionization. It has a typical constant value of 19.5 eV adopted by experiments, as given in [55, 53]. The exciton-to-ion ratio $\alpha \equiv N_{ex}/N_i$ is also commonly introduced, allowing the previous equations to be rewritten as:

$$N_i(\alpha_{\text{ER}} + 1) = \frac{E_{\text{ER}}}{W}, \quad \text{and} \quad N_i(\alpha_{\text{NR}} + 1) = \frac{E_{\text{NR}}\mathcal{L}}{W}. \tag{2.12}$$

While a complete theoretical description of the α ratio's dependence on the incoming particle's type, energy, or the applied electric field is still lacking, experimental studies have provided some insights. Notably, the α ratio differs between ER and NR interactions. For ER, α has been measured as 0.21 [60], while for NR, it has been reported to vary between 0.6 and 2.4 in the NR energy range of 16.9 – 57.3 keV [61]. Other studies suggest a constant value for α, such as 0.19 in [62] and 1 in [63].

2.4.1 Electron-ion Recombination

In view of the previous discussion, a fraction of the electrons liberated due to ionization can recombine with the positive ions, potentially emitting scintillation light. This phenomenon is known as "*recombination.*" The recombination is a very complex process and depends on many factors: the applied electric field across the LAr medium, the initial distribution of electrons and ions and therefore the nature and the kinematics of the original interacting particle, the mobility of the charges inside the LAr, the distance traveled by the electrons, and the diffusion rate.

From a theoretical point of view, two classes of models are available: Thomas-Imel box-model [64] and "*columnar recombination*" model by Jaffe [65]. The former parameterize the recombination process for low-energy recoils of $\mathcal{O}(1\,\mathrm{keV})$, while the other handles higher energy recoils.

Thomas-Imel box-model suggests that the electron-ion pairs can be treated as independent entities, meaning each electron and its corresponding ion interact primarily with each other, rather than with other pairs or the surrounding environment. It assumes that immediately following the primary interaction, the charges are uniformly dispersed within a cubic enclosure of side length a. In other words, within the "box" (a localized region around the ionization event), the electrons and ions recombine or move independently of neighboring pairs. This localized treatment simplifies the modeling of recombination and charge transport processes. In the presence of an electric field, the proportion of charges that survive recombination and subsequently become collected is determined by:

$$\frac{Q}{Q_0} = \frac{1}{\xi} ln(1+\xi), \qquad \text{with} \qquad \xi = \frac{N_0 \alpha}{4a^2(u_- + u_+)\mathcal{E}}\,, \tag{2.13}$$

where ξ is a free parameter to be determined experimentally and can be defined in terms of the number N_0 of pairs inside the box with side length a, α the recombination coefficient, the mobility u_- and u_+ of the electrons and the ions, respectively, and the electric drift field $\mathcal{E}$. Later this model was empirically modified [66, 67] to adopt a power-law dependence of electric drift field and introduce two distinct free parameters b and C.

$$\frac{Q}{Q_0} = \frac{N_i}{\xi} ln(1+\xi), \qquad \text{with} \qquad \xi = \frac{N_i C}{\mathcal{E}^b}. \tag{2.14}$$

Here N_i is the number of initial ion-electron pairs produced due to the energy deposition, written in Eq. 2.12. Given $\frac{Q}{Q_0}$, which represents the escape probability, the recombination probability can be expressed as:

$$r = 1 - \frac{Q}{Q_0}. \tag{2.15}$$

2.4.2 Liquid Argon Observables

To summarize, the scintillation light, corresponding to the S1 signal, originates from the excitons produced directly as well as those formed through recombination. On the other hand, the electroluminescence, or the S2 signal, is generated by electrons that are freed through ionization and are able to escape recombination due to the influence of the applied drift electric field. Therefore, the number of photons (n_{ph}), and the number of electrons (n_e), can be described as functions of the recombination probability as follows:

$$n_{ph} = N_{ex} + rN_i, \quad \text{and} \quad n_e = (1-r)N_i. \tag{2.16}$$

The detection of both scintillation (S1) and electroluminescence (S2) signals relies on photosensors, necessitating a clear relationship between the number of photons and electrons to the S1 and S2 signals through the properties of the detector. To characterize this relationship, we define the factor g_1 representing the light collection efficiency, which expresses the relation between the produced photons and the detected number of photo-electrons for the S1 signal. Likewise, g_2 represents the average number of detected electroluminescence photo-electrons per one electron in the S2 signal. Both are detector properties and remain constant for NR and ER events. Thus, the observables can be expressed as:

$$\mathrm{S1} = g_1 n_{ph}, \quad \text{and} \quad \mathrm{S2} = g_2 n_e. \tag{2.17}$$

2.5 Detector Design

After examining the properties of liquid noble gases, particularly argon, it is a logical progression to explore how they can be leveraged to provide the sensitivity and detector-mass scalability required for rare-event searches. This section explores the operational principles of a dual-phase liquefied noble gas time projection chamber (TPC) as a detector for neutrino physics and dark matter searches.

The concept of the TPC as a particle detector was initially introduced by David Nygren in 1974 [68]. In Nygren's original design, charged particles moving through a detection medium—initially gaseous methane—ionize the gas, creating electron-ion pairs. To prevent the recombination of these ions and electrons, an electric field is applied, which causes the free electrons to drift towards a two-dimensional readout plane. Scintillation light, produced during the initial ionization process, triggers the detection and provides precise timing for the event. By measuring the time it takes for the ionization electrons to reach the readout plane, and knowing the constant drift velocity of the electrons in the medium, the position of the interaction along the drift direction can be accurately determined. Although these systems offer exceptional spatial resolution and tracking capabilities, their low interaction rates—due

to the low density of the gaseous medium—posed a significant limitation. To address this issue, Carlo Rubbia proposed in 1977 the use of LAr as a detection medium [69].

Since then, the TPC concept has undergone significant advancements, leading to the development of current dual-phase TPCs. This technology allows for the simultaneous measurement of both scintillation and ionization signals resulting from particle interactions within the detection medium. Figure 2.2 provides a schematic representation of the signal production process in a typical dual-phase TPC.

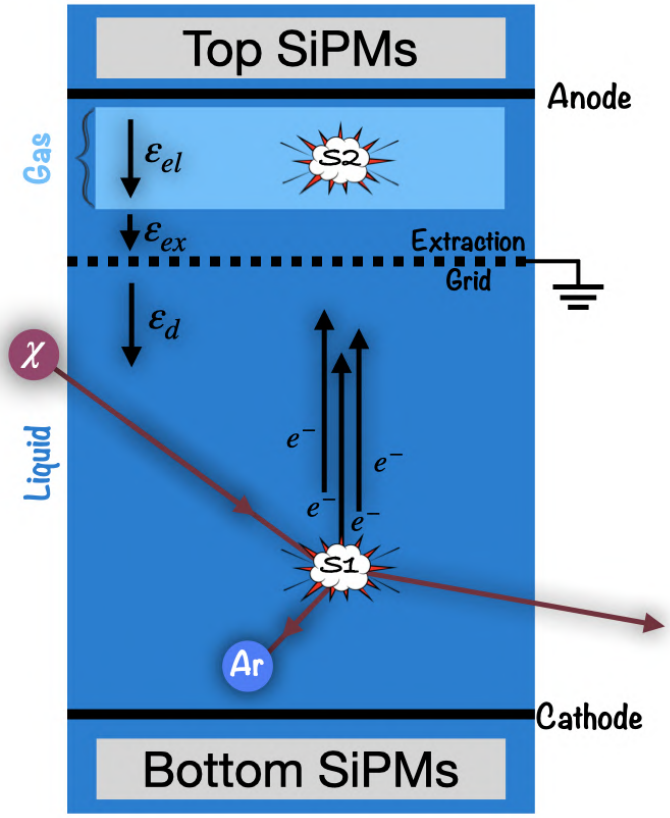

Figure 2.2: A sketch showing the working principle of a dual-phase TPC; The prompt scintillation light (S1) produced as a result of the energy deposit by a WIMP (χ). The electric field in three different regions of the TPC, indicated here as the drift field (ε_d), extraction field (ε_{ex}) and electroluminescence field (ε_{el}), is responsible for drifting free ionisation electrons towards the extraction grid, extracting them into the gas phase, and producing the electroluminescence signal in the gas, respectively. Both signals are detected by SiPMs placed above and below the active volume. The S2 signal pattern on the top SiPMs, along with the time difference between S1 and S2, enables 3D position reconstruction.

In a dual-phase TPC, when a particle traverses the liquid volume of the detector, it deposits energy that leads to the excitation and ionization of the target atoms, resulting in the formation of excitons and electron-ion pairs. The excitons subsequently emit scintillation light, and a fraction of the electron-ion pairs undergo recombination, further contributing to this light; this collective emission is referred to as a primary scintillation signal (S1).

The TPC is equipped with two conductive electrodes: the anode at the top and the cathode at the bottom, both maintained at fixed electric potentials. Electrons escaping recombination are drifted upwards toward a grounded metallic wire grid, positioned just beneath the liquid-gas interface, under the influence of the *drift field* (ε_d) established between the cathode and the grid. Between this grid and the anode, two distinct electric fields are established with different intensities due to the varying dielectric constants of the liquid and gaseous phases. The field within the liquid phase, known as the *extraction field* (ε_{ex}), is designed to enable electrons to surpass the liquid-gas potential barrier. In the gas phase, the field, termed the *electroluminescence field* (ε_{el}), accelerates the electrons enough to excite but not to ionise the gas generating a proportional electroluminescence signal (S2).

Both signals are detected by light sensors—either photomultipliers (PMTs) or silicon photomultipliers (SiPMs)—located at the top and bottom of the detector. Since the photons emitted by argon scintillation have a wavelength of 128 nm, which falls outside the sensitive range of typical photosensors, they are first converted into visible light for detection. To facilitate this conversion, the internal surfaces of the TPC are entirely coated with a layer of tetraphenyl butadiene (TPB). TPB serves as a wavelength shifter, re-emitting photons at approximately 420 nm, a wavelength to which photosensors are expected to have optimal sensitivity. In a typical TPC, three-dimensional position of interaction events can be reconstructed using these signals. The spatial distribution of the S2 light on the top array of the photo-detectors provides the horizontal xy coordinates of the interaction. While the z-coordinate is inferred from the drift time of the electrons from the interaction point to the gas pocket, i.e. the time difference between the S1 and S2. This 3D vertex reconstruction is an effective tool for background rejection.

Furthermore, as discussed in Sec. 2.2, the substantial difference in decay times between triplet and singlet states in LAr—with a ratio of approximately 200—can be exploited as a powerful tool for ER rejection. By examining the cumulative integral of the charge, the relative contributions of singlet and triplet excimers can be estimated. It is evident from Fig. 2.3 that in NR events, the majority of the light is emitted within the first few nanoseconds contrary to ER events.

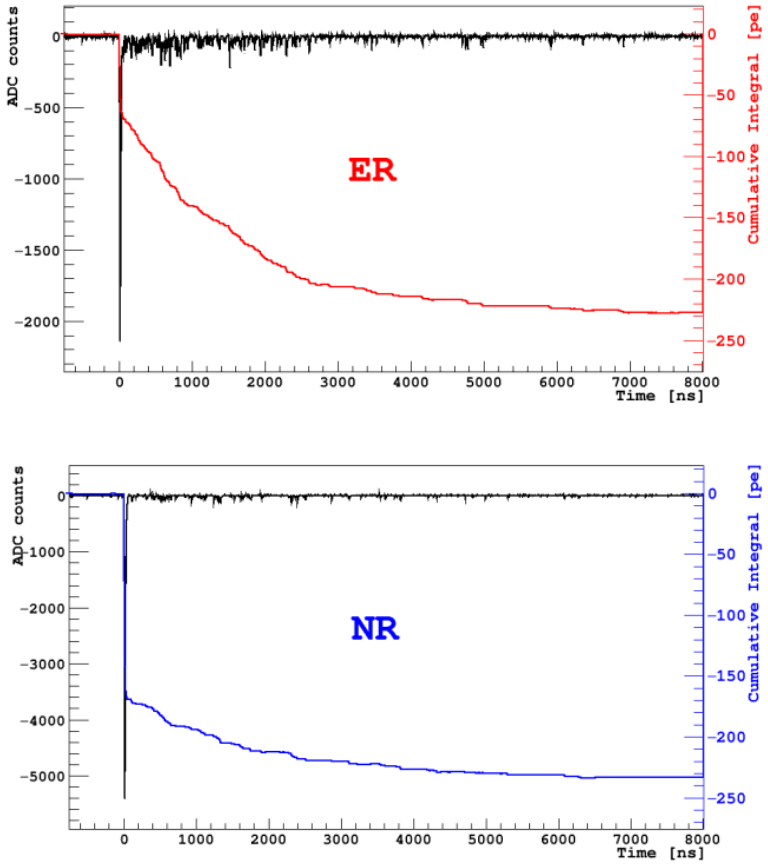

Figure 2.3: Two typical waveforms for ER (*top*) and NR (*bottom*) in liquid argon. The waveforms are chosen to have approximately the same integral. The solid curves represents the cumulative integral. In the NR case, the majority of the signal charge is concentrated in the prompt fraction, in contrast to the ER waveform. Figures are taken from [70].

To characterize this difference, a parameter is commonly defined as the ratio of the scintillation pulse intensity within the first hundred nanoseconds to the total pulse intensity. This ratio provides a reliable estimate of the LET of the incident particle, thereby enabling identification of the particle type, and it can be expressed as:

$$f_{\text{prompt}} = \frac{\int_{t_{\text{start}}}^{t_{\text{prompt}}} \text{S1}(t)dt}{\int_{t_{\text{start}}}^{t_{\text{end}}} \text{S1}(t)dt}. \tag{2.18}$$

This method, known as Pulse Shape Discrimination (PSD), is a robust technique for distinguishing between ER and NR events. In LAr, the singlet fraction typically measures around 0.3 for ERs and approximately 0.7 for NRs. As a result of the PSD, argon detectors can in principle be free from all the known β and γ backgrounds to an unprecedented degree in the WIMP search

region of interest (ROI), a capability that was validated by the DarkSide-50 experiment over a 500+ day run [71].

2.6 The DarkSide Program

The DarkSide program comprises a series of experiments, employing dual-phase TPCs designed to detect WIMPs, utilizing LAr targets of progressively increasing mass. Some of these experiments have already been commissioned and have collected data, such as DS-10 with a 10 kg target and DS-50 with a 50 kg target. Upcoming experiments include DS-LowMass, which will utilize a 1 t target, and DS-20K, currently under construction, with a target mass of 50 t. The program's long-term goal is Argo, which aims to achieve a target mass between 200 – 300 t. The DarkSide program has catalyzed the establishment of the Global Argon Dark Matter Collaboration (GADMC), a comprehensive initiative that consolidates multiple Argon-based dark matter experiments, including ArDM and DEAP, to foster greater collaboration in the pursuit of DM direct detection.

The GADMC collaboration has strategically focused on exploring both high-mass WIMPs, within the mass range of 10 $\mathrm{GeV/c^2}$ to 10 $\mathrm{TeV/c^2}$, while also extending its research to encompass low-mass WIMPs in the 1 – 10 $\mathrm{GeV/c^2}$ range. In the case of high-mass WIMPs, the relevant nuclear recoil energy falls between 30 – 200 keV_{nr}, where PSD is highly effective in differentiating between electron and nuclear recoils. Conversely, for low-mass WIMPs, which generate nuclear recoils in the lower energy range of 1 – 30 keV_{nr}, background differentiation relies on the detailed analysis of the ionization signal spectrum rather than PSD which is less effective.

The primary objective of DS-20K and Argo is to achieve sensitivities down to the so-called "*neutrino floor*", below which Coherent Elastic Neutrino-Nucleus Scattering(CEνNS) from atmospheric neutrinos may obscure DM signals. This correspond to cross section for WIMP-nucleon elastic scattering of $10^{-48}\,\mathrm{cm^2}$ for WIMP masses around 100 $\mathrm{GeV/c^2}$. Achieving this sensitivity is possible due to several technological advancements: efficient PSD against background of scintillation signals, accurate three-dimensional event localization within the TPC, advanced chemical purification and cryogenic distillation of LAr, implementation of an outer neutron veto system, and the use of highly radio-pure SiPMs.

In the low-mass region, the aim for DS-LowMass [72] is to perform an electron-counting analysis focused *solely* on ionization signals (S2-only) to search for low-mass WIMPs. This approach is necessary because detecting the scintillation signal (S1) from low-energy nuclear recoils has low efficiency. Even though the ionization channel provides access to the lowest energy sensitivity of these detectors, the lack of S1 comes at the expense of losing the

capacity to reject ERs based on PSD and to reconstruct interactions' vertical positions. Therefore, meticulous background studies focused on the dominant backgrounds below $3\,\mathrm{keV}_{ee}$ for developing suppression and rejection strategies in order to reach tolerable event rates that would not compromise the detection signals. Among these backgrounds is ^{39}Ar with a half-life of 269 years, which produces low-energy beta decays that overlap with the energy ROI for low-mass WIMPs. Thus, a critical aspect for the success of these searches is the depletion of ^{39}Ar in the target LAr. DarkSide-50 has demonstrated that Argon sourced from underground (UAr) contains ^{39}Ar at levels reduced by at least a factor of 1400 compared to atmospheric argon [73].

CHAPTER III

Low-energy NR Calibration

In the previous chapter, we demonstrated that liquid argon (LAr) is a highly efficient medium for detecting both high- and low-mass Weakly Interacting Massive Particles (WIMPs). Furthermore, we provided an overview of the operational principles of LAr time projection chambers (TPCs) as an effective detection technology, capable of simultaneously measuring ionization and scintillation signals, which enables accurate event reconstruction and efficient background suppression. The primary challenge in detecting low-mass WIMPs stems from the low-energy nuclear recoils (NRs) they produce, which often cause the primary scintillation signal (S1) to fall below the detection threshold. In this chapter, we will briefly examine how the exclusive use of the ionization signal (S2-only) and leveraging ultra-low background conditions through argon chemical purification and cryogenic distillation, LAr TPCs can attain the sensitivity required for probing the low-mass WIMP region. In addition, the factors limiting this sensitivity will be analyzed, along with potential calibrations that could enhance sensitivity. This chapter motivates the search for low-mass WIMPs and reviews the experimental setup designed to characterize the argon response in the low-energy region.

The research relied on the collaborative efforts of the ReD working group, whose contributions were vital for the project's success. During a seven-month period, I collaborated with the local ReD group in Catania, Italy, to prepare and commission key detectors. My involvement included assembling the mounting frame for the PScis, making critical hardware adjustments—such as replacing the anode and cathode windows of the TPC in a cleanroom environment—and performing preliminary calibrations on the BaF_2 detectors and

PScis, along with conducting laser and source runs in the TPC. These activities were essential for ensuring optimal detector performance prior to data collection. This chapter summarizes my contributions while acknowledging the collaborative nature of the broader research effort.

3.1 Low-mass WIMP Searches

In terms of the ionization yield, argon and xenon detectors exhibit fairly similar performance. However, low-mass WIMPs elastically scattering off an argon atom would produce more energetic recoil compared to xenon, as the momentum transfer is more favorable due to argon's lower atomic mass. This compensates for the lower cross-section in argon with respect to xenon.

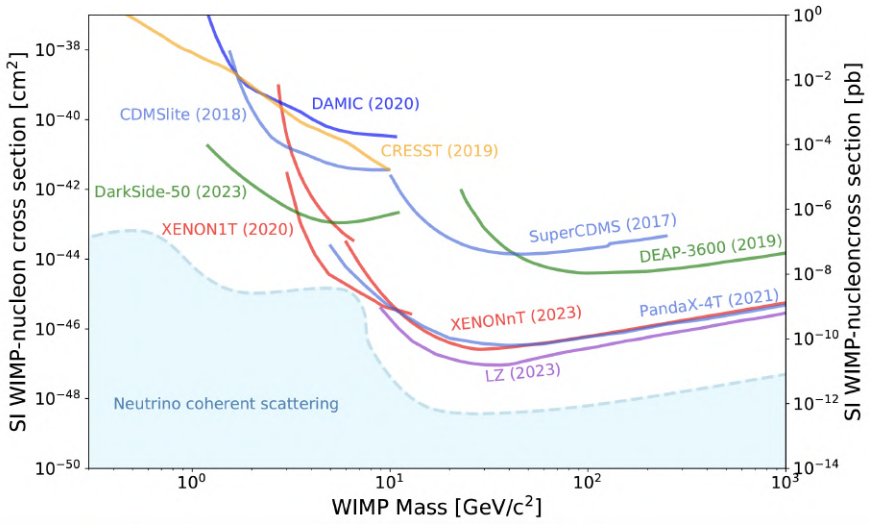

Figure 3.1: The exclusion limits drawn by various experiments on the spin-independent WIMP-nucleon elastic scattering as a function of the WIMP mass. The figure is taken from the Particle Data Group: 2024 Review [44].

DarkSide-50 has demonstrated that the same technology designed for a high-mass WIMP search can be used in the context of searching for low-mass DM candidates by looking *solely* at the ionization signal [74]. This analysis yielded the most stringent upper limit on the spin-independent WIMP-nucleon elastic scattering in the mass range of 1.2 – 4.7 GeV/c^2, as shown in Fig. 3.1. However, a deeper understanding of the NR signal response of LAr over the recoil energy range expected from low-mass WIMP interactions is of paramount importance to minimize the significant systematic uncertainties —due to the intrinsic stochastic nature of the ionization process— and hence enhance the sensitivity of LAr detectors.

DarkSide-50 used a model with two free parameters to describe the NR ionization yield [75]. The two parameters have been determined by performing a fit on calibration data with an ^{241}Am^{13}C (AmC) and an ^{241}Am^{9}Be (AmBe) neutron sources, alongside external datasets from the ARIS [76], SCENE [77], and Joshi et al. [62] experiments. One of the parameters is related to the recombination in the Thomas-Imel framework. While the other is related to the normalization of the f_V, which represents the fraction of energy going to the excitation and ionization channels. This can be calculated theoretically as:

$$\frac{S_e(\epsilon)}{S_e(\epsilon)+S_n(\epsilon)}, \qquad \text{with} \quad \epsilon \approx 0.625\,\frac{a_0}{e^2}\,\frac{E_{rec}}{2Z^{7/3}},$$

where ϵ represents the reduced energy for a NR of energy E_{rec} with target atomic number Z, Bohr radius a_0, and elementary charge e. $S_e(\epsilon)$ and $S_n(\epsilon)$ are the electronic and nuclear stopping powers, respectively. Even though there are different models to calculate these screening effects, their energy dependence at low-energy recoils are uncertain as shown in the left panel of Fig. 3.2. A further suppression in $S_e(\epsilon)$ for low-energy recoils is also plausible, which would lead to even lower ionization yields. Therefore, in the DS-50 model, f_V was modified with a suppression term with one free parameter and adopted the most conservative model of Ziegler then refitted with the same datasets, as depicted in the right panel of Fig. 3.2. The uncertainties on the neutron-nucleus differential cross sections relevant to the scattering processes were not accounted for during the global fit. Furthermore, differential cross sections are usually measured at high angles which corresponds to large recoil energies and then fitted to an optical model. This might be a weakness that could be addressed and more effectively constrained by directly measuring the ionization yield in this low-energy range below 5 keV$_{nr}$.

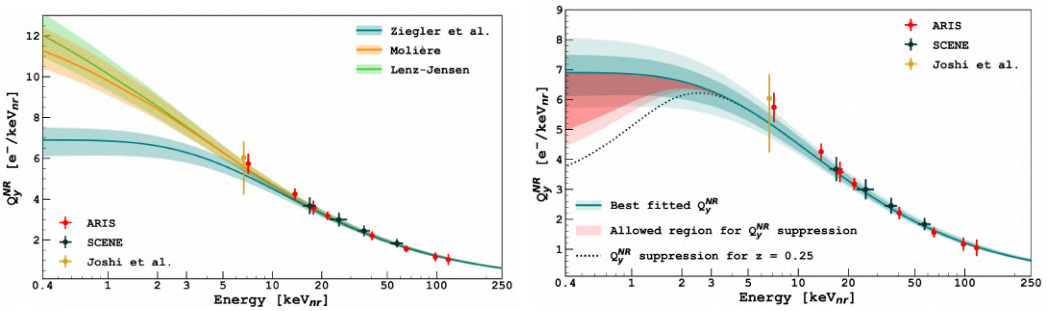

Figure 3.2: Global fit of DarkSide-50 AmBe and AmC data, and ARIS and SCENE datasets for different nuclear screening functions. The blue curve corresponds to the Ziegler et al. [78] model, while the orange and the green curves correspond to the Moliere [79] and the Lenz-Jensen [80, 81] models, respectively. The shaded regions correspond to the 1 σ bands. Figures taken from Ref. [74].

3.2 The ReD Experiment

The ReD (*Recoil Directionality*) experiment, an R&D project of the GADMC Collaboration, was designed to investigate the directional sensitivity of dual-phase LAr TPCs. This sensitivity is theorized to stem from columnar recombination, where the scintillation and ionization signals depend on the angle between the recoiling nucleus and the electric field. When a nucleus recoils, it creates a high-density track of excited and ionized atoms. The drift field separates some electrons from this track, resulting in the S2 signal. Columnar recombination models propose that the fraction of recombined charge is affected by the angle between the recoil direction and the drift field. In extreme cases, a recoil perpendicular to the drift field allows electrons to cross a minimal portion of the ion cloud, while a recoil parallel to the drift field forces electrons through the entire ion column, increasing recombination probability.

Initial indications of this phenomenon were observed in SCENE data [77]. In February 2020, ReD conducted a data campaign to investigate the previous hints and provide further insights into the recombination mechanism in argon. The ReD TPC was exposed to a tagged neutron beam of known energy and direction, provided by the TANDEM accelerator at INFN - Laboratori Nazionali del Sud (LNS) in Catania. Detection of neutrons scattered off argon was achieved using a neutron spectrometer consisting of seven Liquid Scintillator (LSci) detectors. These detectors were strategically placed to detect neutrons that underwent elastic scattering at identical angles, thereby producing nuclear recoils of about 70 keV within the TPC. Although these nuclear recoils shared the same energy, their momenta formed different angles relative to the TPC drift field of 200 V/cm. Thus, the test for directional effects involved checking whether the TPC's scintillation and ionization responses varied for nuclear recoils of the same energy but different angles. Analysis of the collected data indicated that, if the columnar recombination effect exists, it is too weak to be practically useful for dark matter experiments. More details about the experimental setup and the analysis were published in [82].

3.3 Experimental Setup

Another objective of the ReD experiment is to measure the ionization yield of nuclear recoils within the energy range of 2 to 10 keV_{nr}. This goal is the primary focus of this dissertation.

This measurement employed a ^{252}Cf source that α decays with 96.908 % occurrence to form ^{248}Cm, while undergoes spontaneous fission in 3.1 % of the cases producing neutrons with a multiplicity of 3.76 per fission. The energy of the fission neutrons ranges between 0 and 13 MeV, with a mean energy of 2.3 MeV and a most probable value at 1 MeV [83]. For the purpose of our measurement, we used a ^{252}Cf with an activity of 26 kBq procured by Istituto

Nazionale di Fisica Nucleare (INFN) at Laboratori Nazionali del Sud (LNS) in Catania, Italy. This ^{252}Cf source has been chosen for this low-energy NR

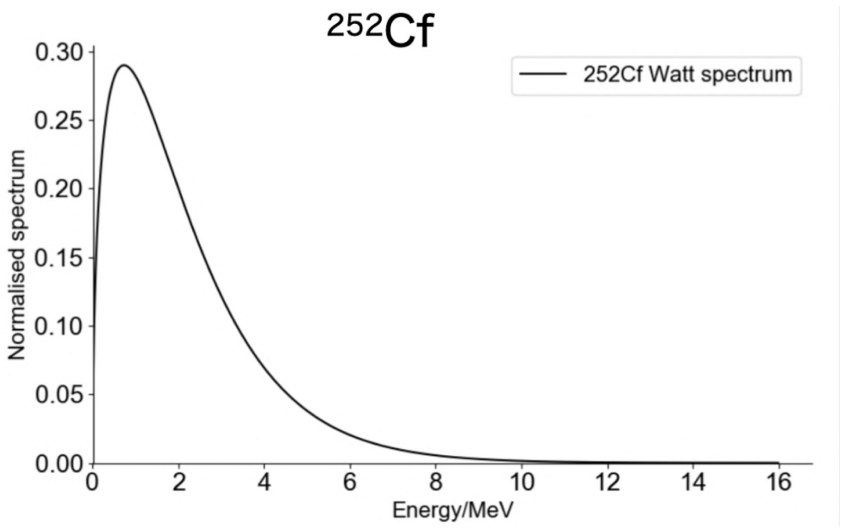

Figure 3.3: The neutron energy spectrum of ^{252}Cf spontaneous fission [84]

calibration due to:

- its high yield that makes it effective for generating a neutron flux of 4.5×10^3 neutrons/s.
- its neutron energy spectrum, which is well understood and allows for accurate calibration across the targeted range of low-energies, as shown in Fig. 3.3.
- its long enough half-life of about 2.6 years, which makes it practical for extended use without significant changes in the rate.
- the accompanying γ-radiation generated during spontaneous fission, which facilitates effective event tagging. This characteristic is the principal advantage of employing ^{252}Cf over an AmBe source.

The experimental setup, illustrated in Fig. 3.4, utilizes this 26 kBq ^{252}Cf source, which is securely housed within a shielding configuration composed of boron-loaded high-density polyethylene (HDPE), lead, and iron. Additionally, two barium fluoride (BaF_2) detectors are employed within the shielding, positioned in close proximity to the ^{252}Cf source. Neutrons emitted from this source are predominantly absorbed by the shielding walls, except for those collimated into an exit cone with an aperture of 2°, which guarantees a uniform illumination of the ReD TPC, positioned approximately 90 cm from the source.

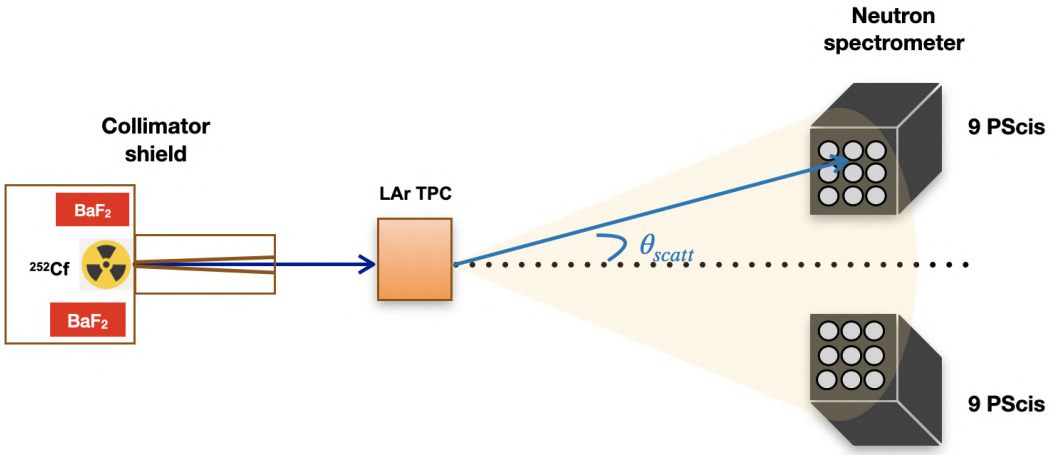

Figure 3.4: ReD Experimental setup: The ^{252}Cf source is hosted inside a shield comprising a High-Density Polyethylene (HDPE) box with a collimator featuring a 2.6-degree opening angle located within a nose section The blue arrow stands for the path travelled by the neutron before scattering elastically inside the TPC, the cyan one is the possible path of the outgoing neutron n' inside the angular range seen by the Neutron spectrometer. Schematic is taken from [85].

Within the TPC, the neutrons undergo elastic scattering off the argon nuclei. Following these interactions, the scattered neutrons continue their trajectory until they are intercepted by a neutron spectrometer located about 100 cm downstream of the TPC.

The neutron spectrometer is composed of 18 plastic scintillators (PScis) arranged in two 3×3 matrices symmetrically placed approximately 25 cm above and below the TPC level, ensuring they remain outside the direct neutron flux emerging from the shielding. The PScis matrices are designed to cover an angular scattering range of $\theta_{scatt} = 12° - 17°$.

This spatial arrangement is crucial for doing a time-of-flight (ToF) measurement on an event-by-event basis; The BaF_2 detectors tag the accompanying γs of the ^{252}Cf fission event providing the critical *START* signal for the ToF measurement, while one of the PScis capture the scattered neutron recording the *STOP* signal for the ToF measurement.

By utilizing the ToF data and the fixed scattering angle determined by the position of the PScis, the energy of the incoming neutron can be accurately reconstructed, more discussed in Sec. 4.3. Furthermore, the recoiling energy of argon nuclei within the TPC can be determined solely based on kinematic

principles from Eq. 3.1, a full derivation is given in Appendix A,

$$E_{rec} = 2E_{\mathrm{n}} \frac{m_{\mathrm{n}} m_{\mathrm{Ar}}}{(m_{\mathrm{n}} + m_{\mathrm{Ar}})^2} (1 - \cos\theta_{scatt}), \tag{3.1}$$

where:

- E_{n}: is the kinetic energy of the incoming neutron. It is evaluated on an event-by-event basis using the time of flight (ToF) between the BaF_2 and PScis, along with the distance traveled by the neutron (d). The energy is calculated, neglecting the energy loss in the TPC, as $E_{\mathrm{n}} = \frac{1}{2} m_{\mathrm{n}} \left(d/\mathrm{ToF}\right)^2$. This approximation is justified since the neutrons produced by the ^{252}Cf source have kinetic energies on the $\mathcal{O}(1\,\mathrm{MeV})$, while their energy loss due to scattering within the TPC is expected to be on the $\mathcal{O}(1\,\mathrm{keV})$. Given that the energy loss in the TPC is three orders of magnitude smaller than the initial energy, it is considered negligible.

- m_{n} and m_{Ar}: are the masses of a neutron and an argon atom, respectively.

- θ_{scatt}: is the outgoing neutron scattering angle, as measured in the lab frame. This is fixed geometrically by the placement of the neutron spectrometer.

This setup facilitates the study of the LAr response to nuclear recoils in the energy range of 2 – 10 keV. By precisely characterizing the response of LAr to low-energy nuclear recoils, we can substantially enhance the sensitivity and accuracy of LAr-based detectors in the detection of low-mass dark matter.

3.3.1 System Alignment

As previously highlighted, the spatial configuration of the experimental components—namely the ^{252}Cf source, the TPC, and the neutron spectrometer—is essential for performing this ToF measurement. To ensure precise alignment, a laser was employed to measure distances and verify the relative positioning of the experimental components. The laser spot has a diameter of 1 mm, allowing for precision measurements within a range of a few millimeters.

A key challenge arises from the fact that the TPC is enclosed within a cryostat, which will remain sealed during operation. Therefore, it is imperative to accurately determine and mark the TPC's position externally to facilitate proper alignment with the other system components. For vertical alignment of the TPC relative to the top flange of the cryostat, a meter and a bubble level were used. The horizontal position and orientation of the TPC relative to the flange is constrained mechanically; Since the TPC is suspended by four Polytetrafluoroethylene (PTFE) rods inserted into four precisely positioned holes on the inner surface of the flange, measuring these hole positions allows us to determine the TPC's orientation. The angular positions of these holes

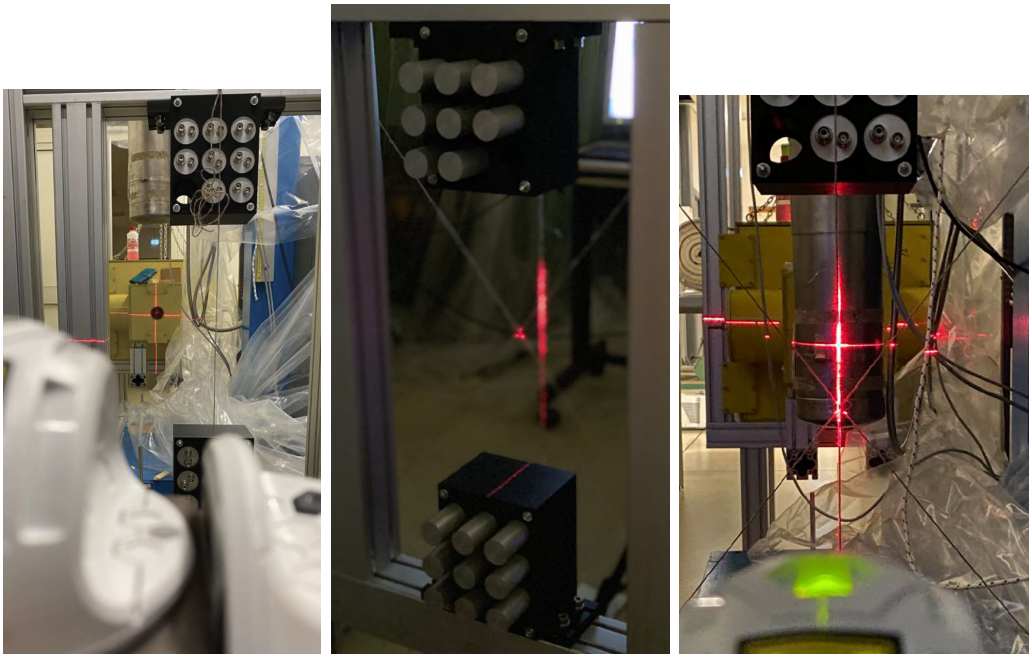

Figure 3.5: The image on the *left* illustrates the laser positioned behind the PScis support structure, with its beam passing through the exit cone and visibly reaching the interior of the shielding where the ^{252}Cf source is located. The support structure was subsequently adjusted so that its axial center, indicated by threads arranged in an X configuration, and the rear thread, which passes through the center of the middle PScis in both the top and bottom cameras, align precisely with the source, as shown in the *middle* image. Finally, the image on the *right* shows the cryostat after being lowered to align the marked center point of the TPC with the same axis.

along with the vertical depth were marked on the external side of the cryostat to provide a reference for the TPC's position and orientation.

To symmetrically position the two neutron cameras above and below the central horizontal axis of the collimator cone, corresponding to the direct line from the ^{252}Cf source, threads were suspended from the support structure of the PScis in an X configuration. A vertical thread passed through the center of the middle PScis and the intersection point of the X threads, as depicted in the middle image of Fig. 3.5. The alignment was further refined by ensuring that this intersection point, the marked center of the TPC on the external cryostat, and the center of the source shield's exit cone were all collinear. This was accomplished using a laser positioned behind the support structure, as shown in Fig. 3.5.

3.4 Taggers Characterization

When a detector is utilized in an experimental setup, the DAQ system records the waveforms, which display pulses representing the measured charge in arbitrary units known as Analog-to-Digital Converter (ADC) counts as a function of time. By integrating these pulses, the total charge is obtained. To calibrate the detector, it is customary to expose it to known calibration sources that produce peaks at specific, well-established energies. This process allows for the determination of the detector's gain, which is a conversion factor used to translate the charge measured in ADC counts into a standard energy unit, such as eV. This calibration step is crucial for ensuring that the measured charge can be accurately interpreted in terms of energy, enabling precise and reliable experimental results. The taggers employed in this setup that were used for the ToF measurement and their energy calibration will be explained in the following subsections.

3.4.1 Barium fluoride (BaF_2) Crystals

Figure 3.6: The images depict BaF_2 crystals wrapped with several layers of Teflon tape and an outer layer of aluminum foil to minimize light loss and enhance light collection from the scintillation process, with one side left exposed for coupling to PMTs. *On the right*, the image displays two BaF_2 detectors situated within the shielding, positioned in close proximity to the ^{252}Cf source to efficiently tag the accompanying γ radiation from spontaneous fission.

The setup employs two BaF_2 crystals, each with a volume of 30 cm^3. BaF_2 detectors have been selected for their exceptional fast scintillation that makes them capable of enduring high source rates. This capability is crucial for accurately tagging the time information of the accompanying γ radiation from the ^{252}Cf spontaneous fission. BaF_2 emits scintillation light at various wavelengths, including a prominent emission at 195 nm. The decay time of its fast scintillation component is within 600 – 800 ps. In addition to these fast components, BaF_2 also emits a slower scintillation light at around 310 nm, with

an average decay time of approximately 630 ns [86]. The intensity ratio between the fast and slow scintillation components in BaF_2 is influenced by the ionizing power of the absorbed particle, enabling gamma discrimination and particle identification through pulse shape discrimination (PSD) techniques. For optimal light collection efficiency, the crystals are manually wrapped with several layers of Teflon tape and an outer layer of aluminum foil, as shown in Fig. 3.6. One side of each crystal is left uncovered to facilitate its attachment to photomultiplier tubes (PMTs). A small amount of optical grease is used to ensure a secure optical connection. The two PMTs have different wavelength sensitivities, with one being more responsive to the shorter wavelengths of the fast light component than the other. This decision was primarily due to the availability of only a single ultraviolet-sensitive PMT, which is the optimal option for our experimental requirements.

3.4.2 BaF_2 Energy Calibration

To calibrate the two BaF_2 crystals, they were operated at the recommended power by the manufacturer of 900 V and exposed to a ^{137}Cs, ^{60}Co, and ^{152}Eu sources. The energy peaks of these isotopes were fitted using a Gaussian function to determine both the mean energy and resolution. This analysis specifically targeted the 662 keV photon from the ^{137}Cs source and the 1.173 MeV γ-ray emitted by the ^{60}Co source. Additionally, it included the significant γ-ray emissions at 121.78 keV and 344.25 keV associated with the decay of ^{152}Eu, which correspond to the de-excitation of excited states in the daughter nuclide ^{152}Sm. The energy spectra and the Gaussian fitting procedure are presented in Fig. 3.7. BaF1 showed a higher gain and a better resolution than BaF0. This difference in response is due to the different models of the PMTs connected to the crystals which have different wavelength sensitivity ranges. The one coupled to BaF1 is more sensitive to the fast light component with shorter wavelengths.

Table 3.1 presents the results of the linear fit, where the means of the four peaks were determined through Gaussian fitting. This approach facilitated the extraction of the parameters a and b in the linear relationship defined by the equation:

$$\text{energy}\,[\text{keV}] = a \times \text{charge}\,[\text{ADC}] + b.$$

3.4.3 Plastic Scintillators (PScis)

The neutron spectrometer utilized to intercept the scattered neutrons from the TPC is comprised of 18 PSci detectors, manufactured by Scionix. These detectors consist of EJ-276 cylindrical scintillators, coupled with Hamamatsu R1924A PMTs. The selection of EJ-276 scintillator material is due to its excellent n/γ PSD capabilities, which are critical for distinguishing potential γ-ray

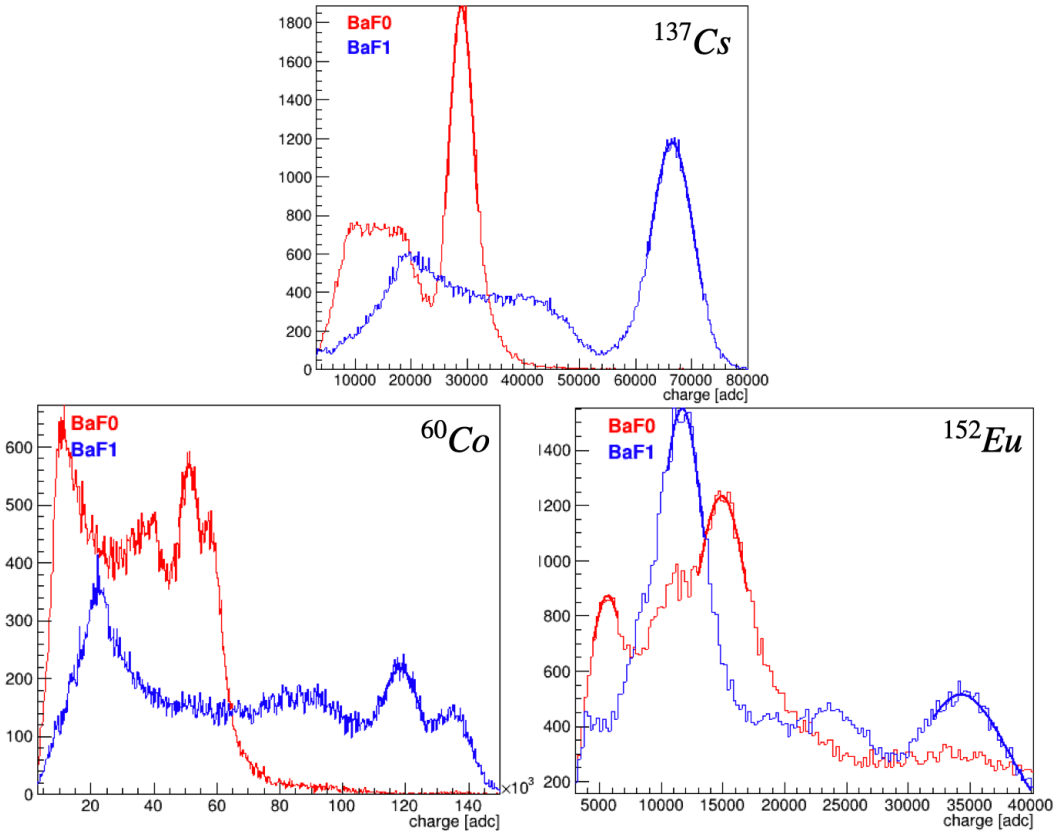

Figure 3.7: The energy spectra of the ^{137}Cs, ^{60}Co, and ^{152}Eu sources as detected by BaF0 (*red*) and BaF1 (*blue*). The peaks have been fitted with a Gaussian to determine the mean energy resolution, evaluated as σ/μ. They are 5.33 % and 4.34 % for BaF0 and BaF1, respectively. Figures by Dr. Maximo Ave Pernas.

BaF_2 ID	**a [keV/ADC]**	**b [ADC]**
0	0.146	2.28×10^{-2}
1	6.376	9.85×10^{-3}

Table 3.1: The result of the linear fit of the ^{137}Cs, ^{60}Co, and ^{152}Eu peaks used to convert the charge measured in [ADC] to energy in [keV].

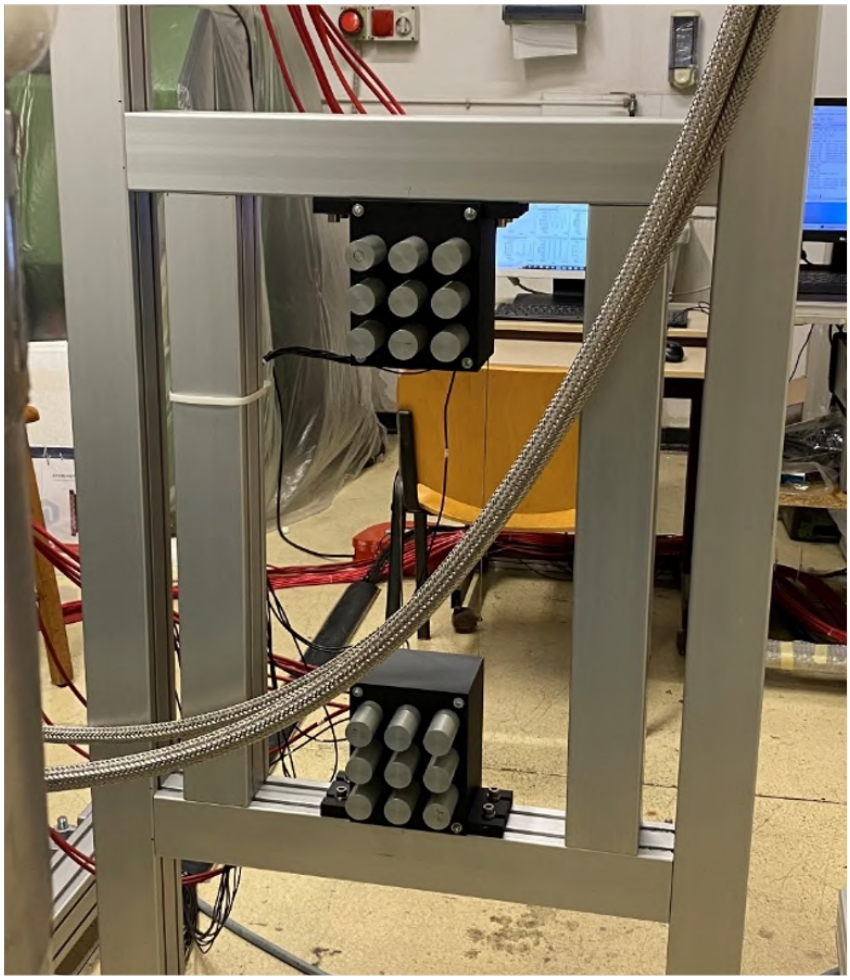

Figure 3.8: The image displays the mounting frame for the two arrays of PScis, which accommodate a total of 18 Scionix EJ-276 scintillator detectors to tag the outgoing scattered neutrons in the TPC.

background events during neutron tagging processes. Furthermore, their small diameter (1 inch), compared with Liquid Scintilators (LScis) allows to obtain a better granularity on the neutron position in the kinematics calculation. They were arranged in two matrices and deployed symmetrically, about 25 cm above and below the level of the TPC, in order to offer a better control on the alignment systematics. Figure 3.8 depicts the finalized support structure for the two PSci arrays; each array contains nine PSci detectors secured in position by a 3D-printed plastic holder.

3.4.4 PScis Energy Calibration

The energy response of the PScis was analyzed using ^{241}Am, which undergoes alpha decay to ^{237}Np. The resulting ^{237}Np nucleus, initially in an excited state, emits a γ-ray of 59.54 keV as it transitions to a lower energy level. This γ-ray

can be fully absorbed by the PScis. We exposed each PSci to the ^{241}Am source and reconstructed the waveforms by utilizing a prolonged charge integration window of 500 ns, ensuring complete capture of the pulse. The gain is defined as the ratio between the ^{241}Am peak charge in ADC counts, evaluated as the mean value of the Gaussian fit, and the known gamma energy in keV. Figure 3.9 illustrate the Gaussian fitting procedure of the 18 PScis with the legends quantifying their gain.

3.5 ReD TPC

The ReD LAr dual-phase TPC, designed and constructed by the UCLA DarkSide group, serves as the central component of the experimental setup. This chamber is characterized by its parallelepiped geometry measuring 5 cm in length, 5 cm in width, and 6 cm in height. Its internal volume is encapsulated by two acrylic windows, each 4.5 mm thick, positioned on the top and bottom. The four vertical walls are composed of two acrylic plates, each with a thickness of 1.5 mm, with a 3M Enhanced Specular Reflector (3M$^{\text{TM}}$ ESR) film placed between them, providing a reflectivity exceeding 98 % [87]. This "sandwich" configuration protects the reflective surface of the 3M film without diminishing the amount of transmitted light, due to the high transparency of the acrylic material. Additionally, this setup eliminates the need for a PTFE reflector, which was identified as a source of Cherenkov background in DarkSide-50 and must be minimized for DarkSide-20k.

Given the scintillation properties of argon, emitting 128 nm VUV photons, conversion to visible light is necessary for detection by optical sensors. This conversion is achieved by coating all internal surfaces of the windows and walls with Tetraphenyl Butadiene (TPB) wavelength shifter, with a coating thickness ranging from approximately 160 – 200 µg/cm^2. This layer converts the VUV photons to approximately 420 nm, which corresponds to the maximum photo detection efficiency of our SiPMs [88].

To establish and maintain the electric field within the chamber, the top and bottom acrylic windows are coated with a 25 nm-thick layer of Tin-Indium-Oxide (ITO) enabling their use as electrodes, following the approach employed in DarkSide-50. Furthermore, a field cage comprising nine copper shaping rings, spaced 0.5 cm apart, surrounds the active volume. To facilitate a field discontinuity at the liquid-gas interface while maintaining high optical transparency, a 50 µm thick stainless steel etched mesh with hexagonal cells, referred to as the grid with an optical transparency of 95%., is positioned approximately 1 cm below the anode window, shown in the right panel of Fig. 3.10.

Using a custom-made triple feedthrough, we apply specific potentials to three electrodes in the TPC: +5211 V to the anode, −839 V to the cathode, and +60 V to the first ring of the field cage. The grid is grounded via a dedi-

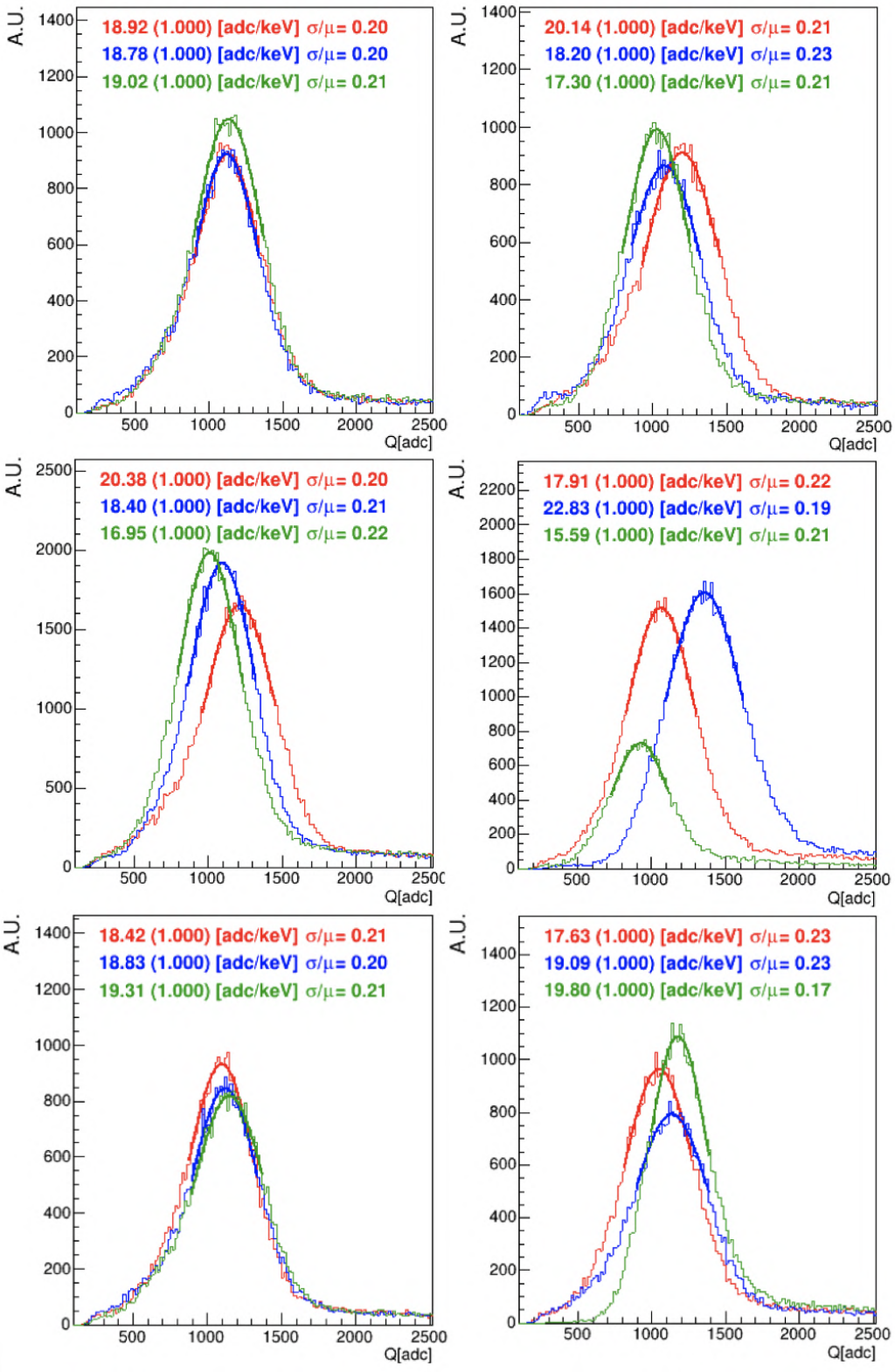

Figure 3.9: The energy spectra of ^{241}Am as detected by the 18 PScis are shown, with the legend indicating the gain calculated as the ratio of the mean value from the Gaussian fit to the known gamma energy of ^{241}Am, which is 59.54 keV. Figures by Dr. Maximo Ave Pernas.

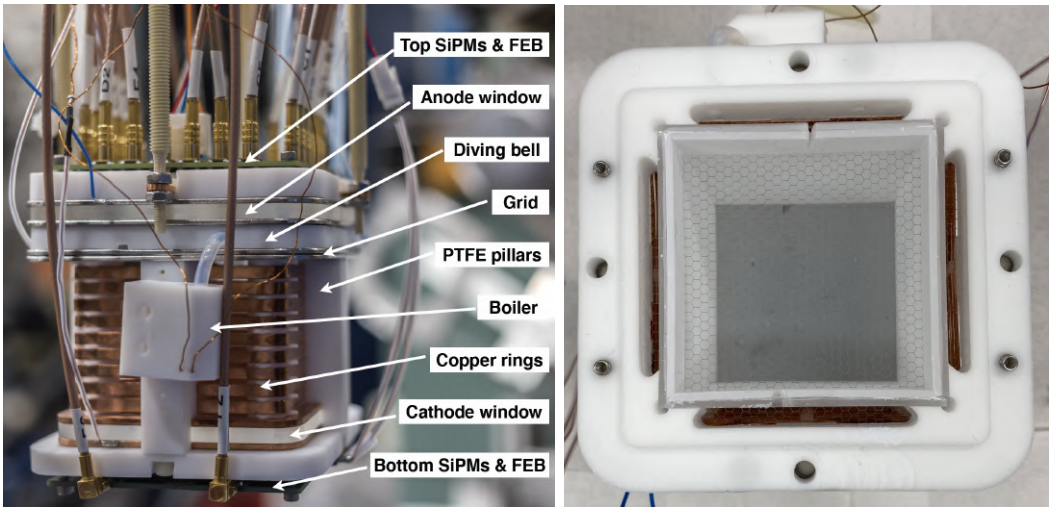

Figure 3.10: *On the left*, a picture of the ReD TPC with labels featuring the parts visible from this side. *On the right*, a picture of the squared PTFE frame (diving bell) and the hexagonal cells grid.

cated contact to the flange of the dewar. Between each ring of the field cage, two 100 MΩ resistors are connected in parallel, resulting in an equivalent resistance of 450 MΩ for the voltage divider. The potential applied to the first ring compensates for edge effects and ensures a uniform drift field.

To mitigate noise from the high voltage power supply, a low-pass filter is installed immediately before the feedthrough, outside the dewar. This configuration establishes three distinct fields within the TPC: a drift field of 200 V/cm, an extraction field of 3.8 kV/cm in the liquid, and an electroluminescence field of 5.7 kV/cm in the gas region.

Gas pocket creation is facilitated by a boiler located external to the TPC, employing a PT-1000 resistor to boil liquid argon and release gas into the chamber via a teflon inlet tube into the so-called diving bell– a narrow region inside the detector between the external PTFE frame holding the grid and the active volume. Due to this diving bell, the gas reaches the active volume of the detector by an overfull mechanism that fixes the height of the gas pocket mechanically ensuring stable operation in double-phase mode. In this configuration, the TPC features a maximum drift length of 5 cm, a 3 mm thick layer of liquid argon above the grid, and a 7 mm thick gas layer. Finally, the TPC is supported by a PTFE structure suspended from the cryostat main flange using four threaded rods, ensuring stability and alignment. More details about the ReD TPC properties and performance is published in [74]

3.5.1 The Cryogenic System

The ReD cryogenic system is a custom-designed apparatus developed by Criotec Impianti S.p.A. in Chivasso, Italy. This system facilitates the liquefaction, recirculation, and purification of commercial 6.0-grade argon gas. All components, including electronics and electrical connections, are mounted on a cart for better mobility. A schematic of the system is illustrated in Fig. 3.11.

This system can be operated in two regimes; one is used during the filling phase, while the other during the recirculation. Before introducing the gas into the apparatus, a preliminary pump-and-purge phase is essential to establish a vacuum level of approximately 10^{-3} mbar.

In the filling mode, the commercial argon gas is gradually introduced into the system from the cylinder at room temperature. It passes through a Mass Flow Controller (MFC) and reaches the condenser, where it is cooled down by contact with a copper cold head. This cold head is cooled down by a compressor exploiting helium pressure variations. It is composed of a PT90 pulse tube coupled with a CP2850 compressor that has a cooling capacity of 90 W at 80 K, both developed by CryoMech [89]. A temperature sensor and a heater between the cold head and the compressor enable feedback control mechanism of the cooling power. Subsequently, the gas enters the dewar, which houses the ReD TPC. The dewar, a double-walled container with a conical shape, hosts the TPC and the liquid argon, with an internal diameter ranging from approximately 13 cm at the bottom to about 25 cm at the top, is sealed with a CF250 flange. Continuous circulation of argon gas at increasingly lower temperatures of the cold head, allows the cooling of the mechanical components, eventually leading to the liquefaction of argon. After approximately twelve hours from the moment the gas is first introduced into the system, the liquid reaches a level of 30 cm, which is indicated by a temperature sensor at this position. At this point the flow of the argon gas from the cylinder is halted, and the system enters in the recirculation mode.

In recirculation mode, the liquid argon boils and evaporates at the surface. Then through the use of valves, the vapour is pushed by the recirculation pump and passes through the SAES getter [90], where the heated getter material forms irreversible chemical bonds with any oxide, carbide, or nitride impurities. After purification, the gas is reintroduced into the condenser cell and re-liquefied. This process maintains equilibrium, keeping the level of liquid argon almost constant.

3.5.2 Silicon Photomultipliers (SiPMs)

A distinctive feature of the ReD experiment is the use of cryogenic SiPMs for reading the TPC signal. This innovation establishes ReD as the pioneer-

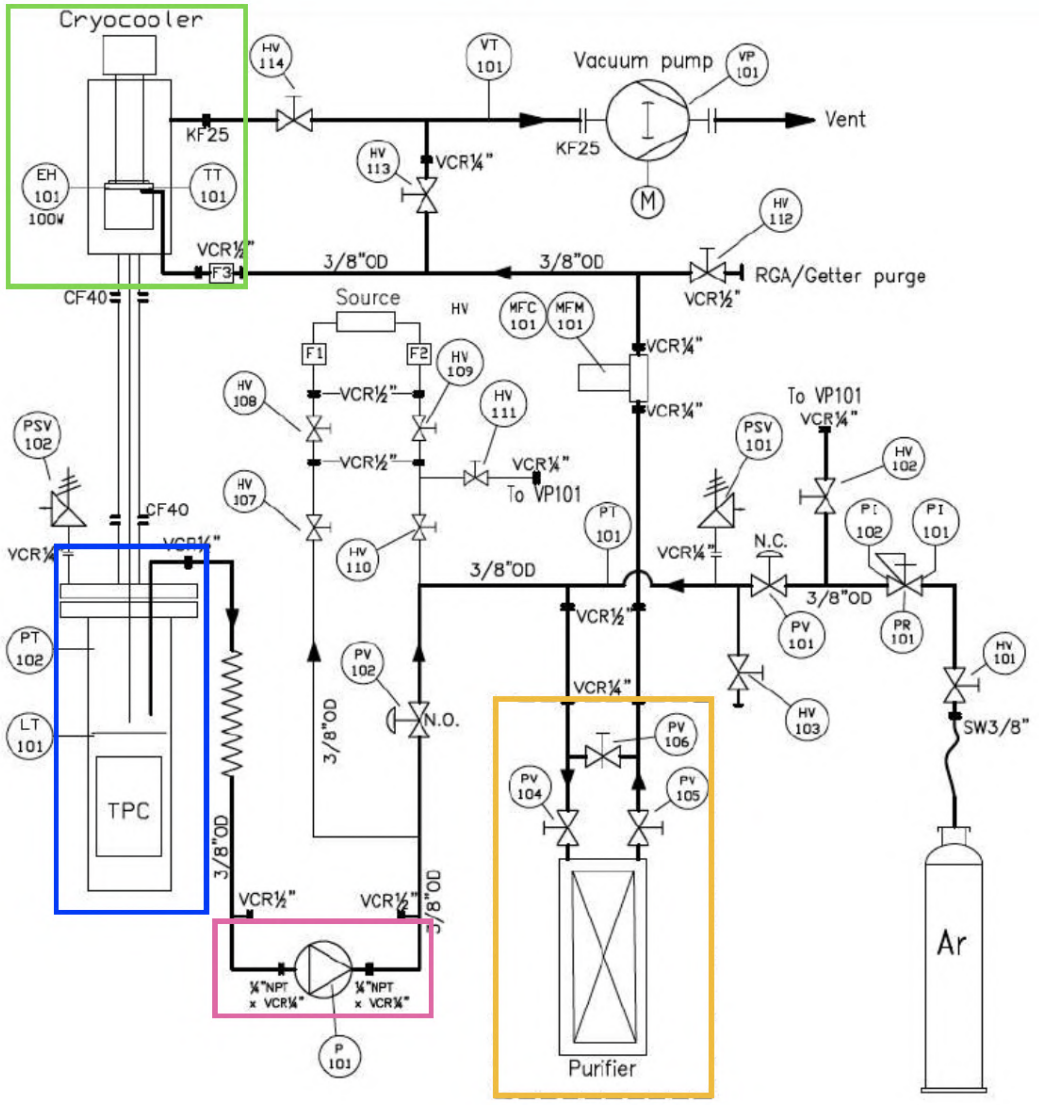

Figure 3.11: The ReD cryogenic system schematic. Argon gas from a commercial bottle is introduced inside the condenser, *the green frame*, where it is liquefied by the cold head connected to a cryocooler. Liquid argon then drops inside the cryostat, *the blue frame*, which contains the TPC. During a regular data taking phase, the pump P101, *magenta frame*, allows recirculation of the gas through the purifier, *orange frame*, and once again into the condenser in a continuous loop.

ing prototype of a dual-phase argon TPC utilizing SiPM technology. These SiPMs, engineered by the Fondazione Bruno Kessler (FBK) in Trento, exhibit only minor differences compared to those intended for the DarkSide-20k experiment. The readout electronics, which supply power to the photosensors and amplify their output signals, were developed and optimized through a collaborative effort involving the INFN groups from Naples, LNGS, and Bologna [91].

SiPMs represent advanced and versatile light detectors with superior Photon Detection Efficiency (PDE) compared to Photomultiplier Tubes (PMTs) and significantly higher single-photon resolution, all while operating at low bias voltages. The fundamental unit of a SiPM is the Single Photon Avalanche Diode (SPAD). Essentially, a SiPM is an assembly of SPADs arranged in parallel, producing a signal proportional to the number of primary photons detected. To understand the working principle, one must first examine the SPAD, which operates in Geiger mode as a reverse-polarized junction. When a photon generates an electron-hole pair, these carriers are driven by an electric field to the multiplication region, initiating an avalanche. The required voltage to trigger this avalanche is referred to as the breakdown voltage (V_{bd}) [92]. SPADs are biased a few volts above this threshold, typically expressed as:

$$V_{\mathrm{bias}} = V_{\mathrm{bd}} + V_{\mathrm{ov}}$$

where V_{ov} denotes the over-voltage. The avalanche is self-sustaining, necessitating a passive quenching mechanism, typically a high resistance in series with the SPAD, to stop the current flow. Post-quenching, the diode recharges and becomes ready to detect new signals. The avalanche mechanism generates an electric current independent of the number of photons in a single SPAD, making the SPAD essentially a binary device. Therefore, multiple SPADs, each with its own quenching resistance, are combined into a SiPM. A typical SiPM consists of thousands of SPADs with micrometer dimensions. By measuring the total charge of the SiPM signal, the number of fired SPADs—and thus the number of incident photons—can be determined.

SiPM signals feature a rapid rise time of a few nanoseconds due to the avalanche initiation, followed by a slower tail lasting for tens of nanoseconds, corresponding to the cell recharge time. SiPMs typically exhibit a gain between 10^5 and 10^7 and a single photo-electron resolution, quantified as σ/μ, of around 2 % [92].

In the ReD TPC, two 5×5 cm^2 tiles are utilized, each with 24 rectangular NUV-HD SiPMs [93] measuring 11.7×7.9 mm^2, as shown in the left panel of Fig. 3.12. These SiPMs are specifically designed for optimal photon detection efficiency in the visible range at approximately 420 nm, featuring a high SPAD density and triple doping concentration. Each SiPM has a cell pitch of 25 µm, and is equipped with a 10 MΩ quenching resistance.

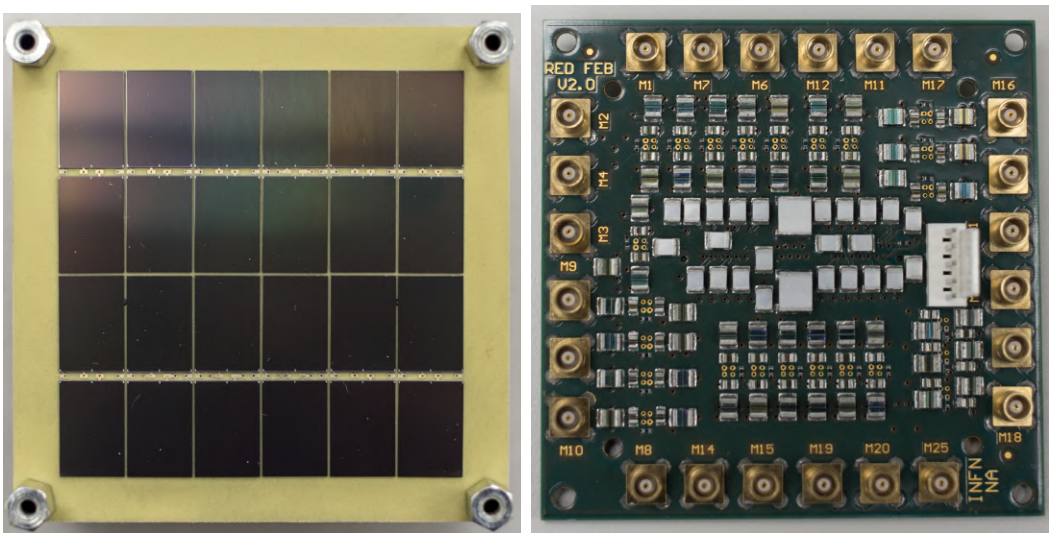

Figure 3.12: *On the left*, the image depicts the front view of one of the NUV-HD SiPM tiles used in the ReD experiment. The square-shaped tile comprises 24 SiPMs interconnected by micro-length wires from the back side. *On the right*, A picture of the 24-channel readout Front End Board, designed and developed in Naples in collaboration with the LNGS and Bologna DarkSide groups, featuring 24 MCX connectors for signal cables.

One tile is situated at the top of the TPC and another at the bottom, each positioned behind their respective acrylic windows. The location of an S2 event in the gas pocket offers a reliable estimate of the xy coordinates of the associated interaction point within the TPC. Consequently, the 24 SiPMs on the top tile are read out individually to enhance spatial resolution, while the SiPMs on the bottom tile have 4 summed-channel readouts, each from the input of 6 SiPMs. The signals readout and the voltage distribution are facilitated by a dedicated custom-designed front-end board, which is illustrated in the right panel of Fig. 3.12. This board has been optimized and produced by the DarkSide INFN groups in Naples, LNGS, and Bologna. The SiPMs are typically operated at an over-voltage of 7 V, corresponding to a V_{bias} of 34 V.

3.6 Laser Calibration

To investigate the response of the SiPMs in the ReD experiment, we employed a Hamamatsu PLP-10 pulsed diode laser, which was externally triggered at a frequency of 100 Hz. The laser emits pulses with a wavelength of 403 nm and a duration of 50 ps. The photons generated by the laser were directed to the inner volume of the TPC via a bundle of optical fibers. This laser calibration facilitates the determination of the number of single photo-electrons corresponding to each detected signal, commonly known as the Single Electron Response (SER). Furthermore, this calibration enables the quantification

of noise and the monitoring of SiPM stability over the course of the experimental runs.

The raw waveforms acquired from each channel undergo processing through a matched filtering algorithm designed to optimize the signal-to-noise ratio. The matched filter is based on the convolution of the waveform with a time-reversed template of the single photo-electron response. This template for the SiPM response, denoted as $s(t)$, was obtained by computing the average single photo-electron waveform from a laser calibration run, as observed by one of the top tile SiPMs. It was found to be accurately modeled by the sum of a fast component (f_{fast}), which determines the rapid rise of the signal and is described by an exponential, and a slow component (g_{slow}), which reflects the recharge time of the SPAD. The slow component is formulated as the convolution of a Gaussian function with an exponential tail. They can be expressed mathematically as:

$$\begin{aligned} f_{\text{fast}}(t) &= \frac{1}{\sqrt{2\pi}\sigma} \exp\left(-\frac{t^2}{2\sigma^2}\right) \\ g_{\text{slow}}(t) &= \frac{1}{2\tau} \exp\left[-\frac{1}{\tau}\left(t - \frac{\sigma^2}{2\tau}\right)\right]\left[1 + erf\left(t - \frac{\sigma}{\sqrt{2}\tau}\right)\right] \\ s(t) &= f_{\text{fast}}(1 - p_s) + p_s g_{\text{slow}}, \end{aligned} \tag{3.2}$$

where p_s, σ, and τ are free characteristic parameters of each SiPM, more details in [74].

Following the filtering process, a moving average is computed on the filtered waveform using a window of 150 samples. The moving average is subsequently subtracted from the filtered waveform, resulting in the histogram designated as "Residual" in Fig. 3.13.

Hits are then identified as segments of this residual histogram that exceed a defined discrimination threshold. This threshold is proportional to the root mean square (RMS) value computed over n samples in the pre-trigger region of the filtered waveform, adjusted by a coefficient tuned to the electronic noise level in the system. For the ReD experiment, a threshold of 3× RMS, evaluated over the first 55 samples, was found to be optimal.

For each detected hit, both the channel identifier and the peak time—defined as the time at which the maximum amplitude is observed within a segment are recorded. Additionally, the hit integral within a fixed window around the peak and the prominence of the peak are calculated and stored. Prominence, defined as the difference between the filtered waveform and the moving average, serves as an indicator of peak height. This metric can be used as a proxy for the number of photo-electrons.

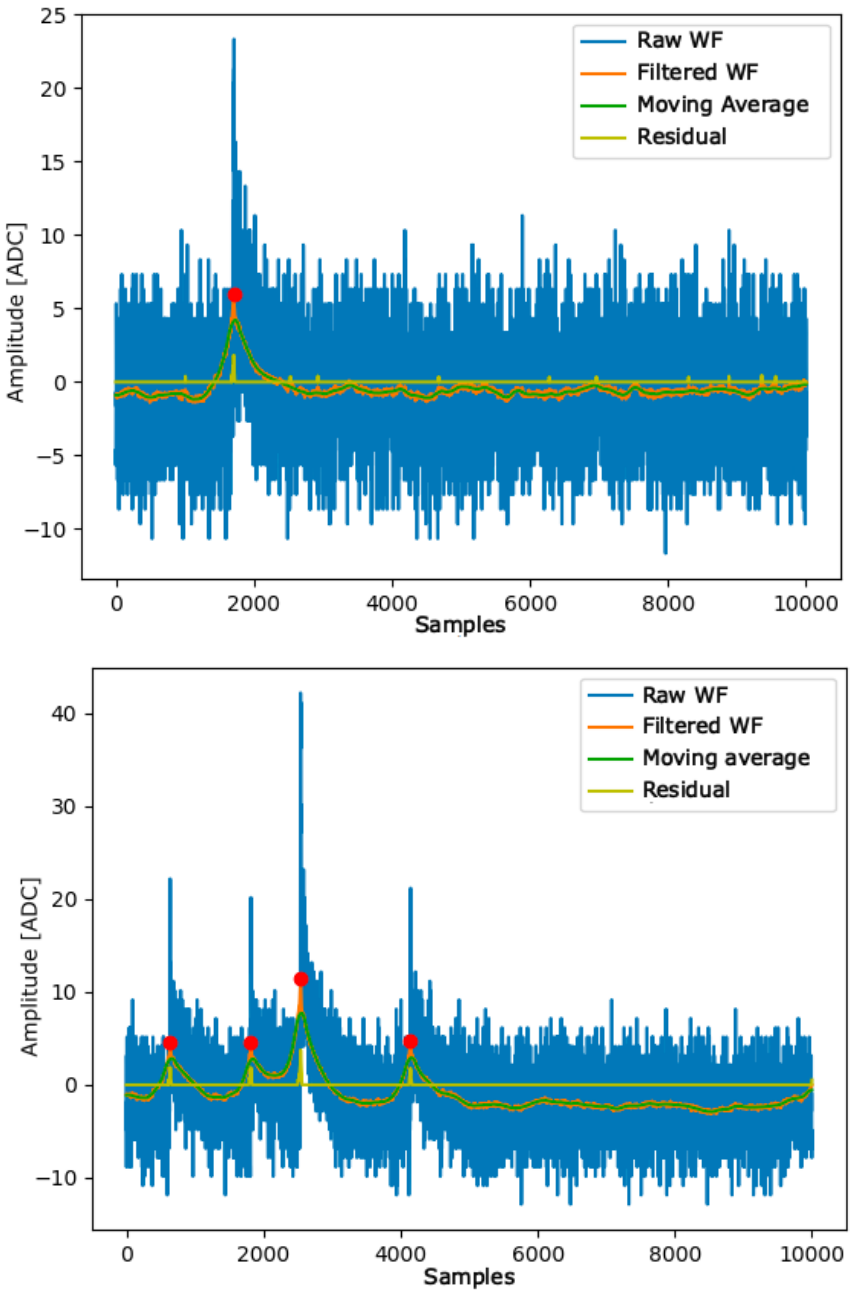

Figure 3.13: The figures depict the steps involved in the hit-finding algorithm developed within the DarkSide collaboration. The histogram labeled as "Residual" is computed from the difference between the filtered waveform and its moving average. Peaks that satisfy the discrimination cut are highlighted by a red point at their top.

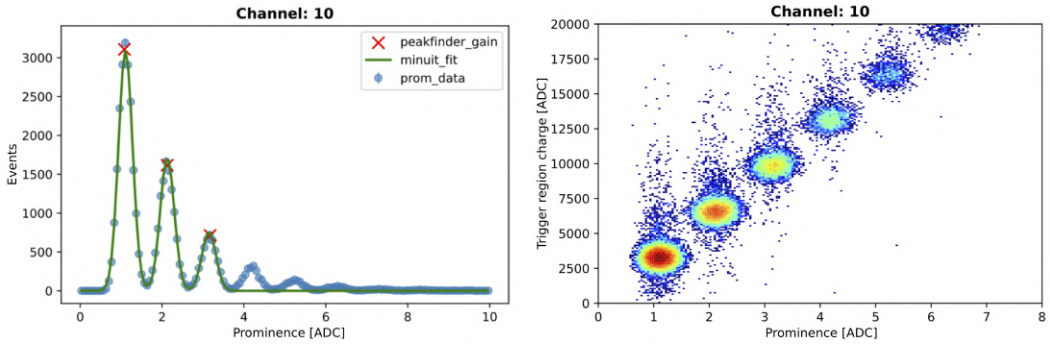

Figure 3.14: *Left*: the prominence finger plot with a composite Gaussian fits applied to the first three peaks. *Right*: A 2D histogram illustrating the linear correspondence between charge and prominence.

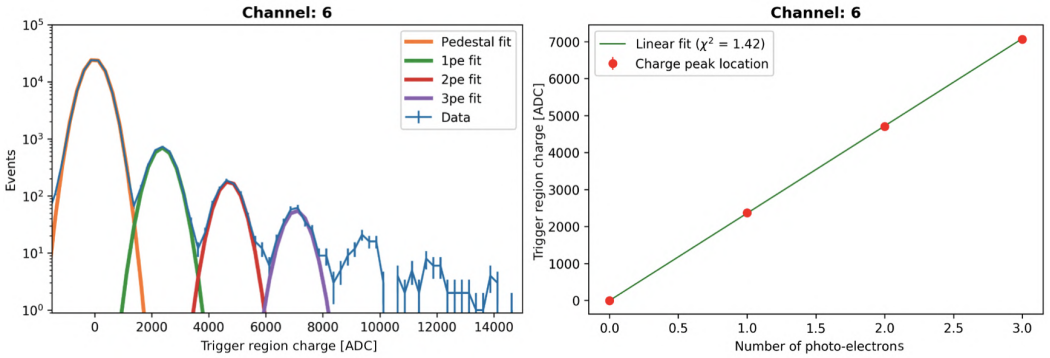

Figure 3.15: *Left*: the charge finger plot with independent Gaussian fits of the first four peaks. *Right*: linear fit applied to the fit mean values of the identified charge peaks.

The calibration process for each channel in each run is conducted individually using two distinct variables: the charge, defined as the integral of the raw waveform over a fixed window of 4 µs around the trigger time, and the peak prominence, as determined by the hit finding algorithm outlined earlier in this section. Although these parameters are correlated, they convey different aspects of the signal information. The prominence methodology provides detailed temporal information and high resolution, whereas the charge retains information about the "pedestal peak" that represents zero photo-electrons, which is essential for calculating occupancy, as demonstrated in the left panels of Figs. 3.14 and 3.15.

The initial step in the calibration involves generating a histogram, where the prominence of the reconstructed hits populates equally separated peaks forming what is referred to as the finger plot. In this high-resolution spectrum, peaks correspond to the number of photo-electrons being detected by the SiPM. At least three prominence peaks are required to establish a reliable

calibration curve. These peaks are fitted using a composite function consisting of three Gaussians, as depicted in the left panel of Fig. 3.14. A linear fit establishes the relationship between the prominence fit mean value (prom) and the number of photo-electrons (nPE), with fit parameters a and b:

$$\mathrm{nPE} = \frac{\mathrm{prom} - b}{a}. \tag{3.3}$$

Although the relationship between charge and nPEs can be determined without incorporating prominence information, the inclusion of the prominence step enhances the precision of the fits. This approach enables an independent Gaussian fit to each peak in the charge distribution, allowing the extraction of the peak position and its standard deviation in charge.

Subsequently, by retrieving the nPE based on the calibration done with the prominence we can individually identify the charge peaks associated with the peaks in prominence, including the pedestal peak corresponding to nPE = 0, as shown in the left panel of Fig. 3.15. While the relationship between charge and nPEs can be determined without incorporating prominence information, including the prominence step enhances the resolution of the fits. This allows for an independent Gaussian fit to each peak in the charge distribution and retrieve the fit parameters of the peak position and its sigma in charge. This allows to establish a linear relation similar to that in Eq. 3.3, which relates the charge gain to the number of photo-electrons, as illustrated in the right panel of Fig. 3.15.

The fit results of parameters a and b representing the slope and offsets of the linear function for all SiPMs are shown in the top panel of Fig. 3.16 in terms of prominence and in the bottom panel in terms of charge.

By examining these parameters, in Fig. 3.16, it is possible to monitor the behaviour of each channel across different runs, allowing for the identification of any instabilities during data taking.

3.6.1 SiPM Noise Characterization

Laser calibration offers valuable insights into the various mechanisms contributing to noise in SiPMs. Since noise is an inherent characteristic of SiPM operation, understanding it is essential for optimizing the sensitivity, accuracy, and reliability of SiPM-based detectors. This is particularly critical in rare event searches, such as those for dark matter, where noise can obscure low-energy signals.

Direct cross-talk (DiCT) happens when a photon, emitted during an avalanche, escapes and provokes a new avalanche in an adjacent SPAD cell. Due to the close proximity of SiPM cells, this phenomenon occurs nearly in-

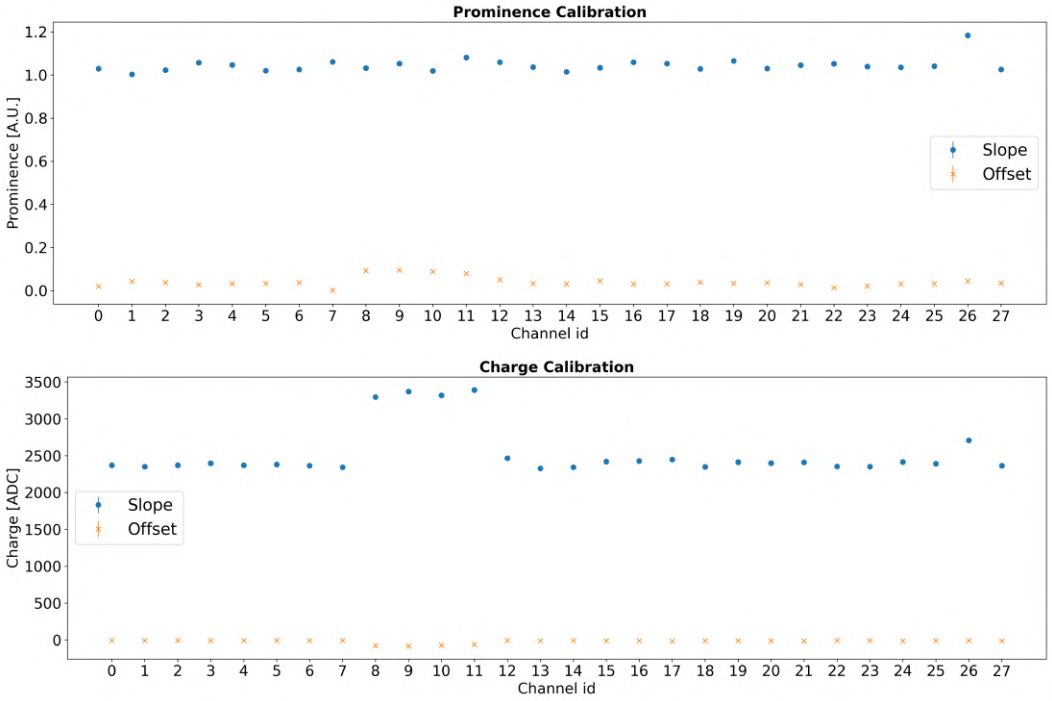

Figure 3.16: The SiPMs calibration results in prominence (*top*) and charge (*bottom*). Channels 8 to 11 are associated with the bottom tile, where the outputs from six SiPMs are integrated into a single readout.

stantaneously, typically within $\mathcal{O}(1\,\mathrm{ps})$. Consequently, this type of noise is indistinguishable from the primary avalanche. As a result, the detectable signal combines the primary event with the cross-talk; therefore, it exhibits an amplitude of at least two photo-electrons. It is also worth noting that one event can trigger a cascade of subsequent cross-talk events.

In the absence of cross-talk, the finger-plot charge distribution would follow a Poisson distribution. However, in reality, it conforms to the Vinogradov model [94], which deviates from Poisson due to an additional parameter representing the cross-talk probability.

To model cross-talk statistically over a Poisson distribution, let us assume a true photo-electron (PE) occupancy of μ, and let x denote the probability of one avalanche triggering cross-talk. Each PE event leads to a series of cross-talk events with a probability of x and concludes with no further cross-talk with a probability of $(1-x)$. Consequently, the probability of observing m cross-talk events given n true PEs is proportional to:

$$P(m_{\mathrm{CT}}, n_{\mathrm{PE}}) \propto x^m (1-x)^n.$$

There exist numerous sequences of true PEs, each potentially containing m cross-talk events, all occurring with a probability of x. However, the exact

distribution of cross-talk events among these sequences is unknown. The proportionality coefficient represents the ways in which m cross-talk events can be distributed among n PEs, which follows a negative binomial distribution, given by:

$$\binom{n+m-1}{m} = \frac{(n+m-1)!}{(n-1)!m!}. \tag{3.4}$$

The -1 in $(n+m-1)$ arises because we are considering the distributions of cross-talk events (successes) that occur after the first true PE, i.e. the first "failure" in the negative binomial framework, and the -1 in $(n-1)!$ reflects that we start counting from the second true PE since the first PE triggers the process. Therefore, the joint probability of observing m cross-talk events and n PEs can be expressed as:

$$P(m_{\mathrm{CT}}, n_{\mathrm{PE}}) = \frac{e^{-\mu}\mu^n}{n!}\frac{(n+m-1)!}{(n-1)!m!}x^m(1-x)^n. \tag{3.5}$$

Let $N = n + m$ represent the total observed number of avalanches. It is important to note that the probability of observing 10 avalanches, for instance, is the cumulative probability of different combinations, such as 1 PE and 9 cross-talks, 2 PEs and 8 cross-talks, and so on. This cumulative probability can be expressed generally by summing Eq. 3.5 for n ranging from 1 to N with $m = N - n$, yielding:

$$P(N) = \sum_{n=1}^{N} \frac{\mu^n e^{-\mu}}{n!}\frac{(N-1)!}{(n-1)!(N-n)!}x^{N-n}(1-x)^n \tag{3.6}$$

This equation represents the Vinogradov model, providing the probability of detecting N photo-electrons given an occupancy μ and an internal cross-talk probability x.

To determine the cross-talk probability x without fitting the finger plot to this complex model, we first extract the parameter μ from the the population of pedestal peak (i.e. number of events in the peak), which is unaffected by cross-talk since it corresponds to events where no PE were produced. We then compare the observed population of the 1 PE peak to the expected population under pure Poisson statistics, given by $P = \mu e^{-\mu}$. The discrepancy between these values indicates the fraction of events affected by cross-talk, which have shifted to populate higher PE peaks. The DiCT for ReD SiPMs were evaluated for each channel independently, as shown in Fig. 3.17.

Channels 8 to 11 correspond to the bottom tile, where the outputs from six SiPMs are combined into a single readout, resulting in a sixfold increase in effective surface area. The top channels exhibit a direct cross-talk (DiCT) probability of approximately 35 %, which is higher than the 20 % reported at an overvoltage of 6 V in [88]. However, given that our operation is conducted

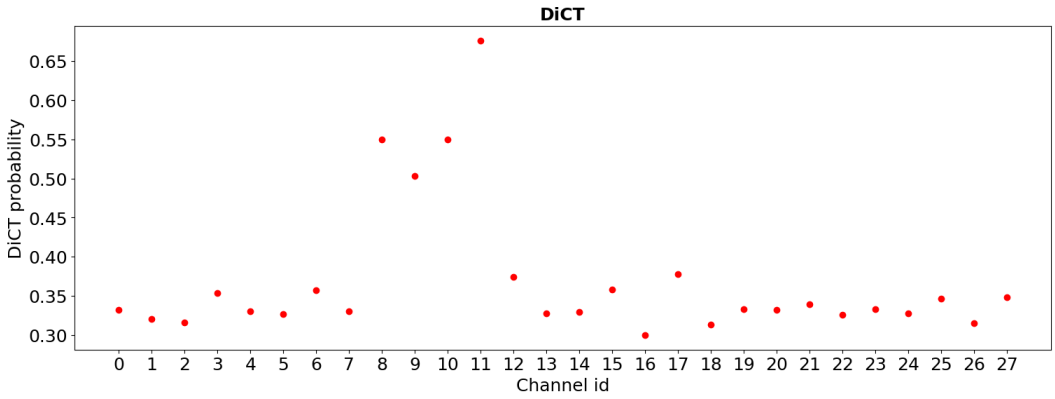

Figure 3.17: The direct cross-talk probability through all ReD channels evaluated as described in the text. Channels 8 to 11 represent the bottom tile, in which the outputs from six SiPMs are combined into a single readout.

at a higher overvoltage of 7 V, this discrepancy can be rationalized through extrapolation.

Delayed cross-talk (DeCT) operates on a similar principle to DiCT. However, in DeCT, the photon generated is absorbed in a non-depleted region of the silicon. The resulting carrier then diffuses through the silicon substrate until it reaches the multiplication region, where it induces a discharge. While the amplitude of this discharge is equivalent to 1 PE, the pulse experiences a delay of $\mathcal{O}(10\,\text{ns})$ compared to the primary event due to the diffusion time.

Afterpulsing (AP) occurs when electrons, trapped by impurities in the lattice, are later released, causing a secondary avalanche in the same SPAD. The timing and amplitude of afterpulses depend on the trapping time and the cell recovery time. Since the SiPM capacitance may still be recharging, an afterpulse occurring shortly after the primary event will have a reduced amplitude. These afterpulses can be characterized by measuring both the probability of their occurrence and their timing relative to the initial photo-electron pulse. The probability of an afterpulse event occurring following a single photo-electron can be quantified by detecting subsequent pulses that occur within a predefined time window after the primary pulse. This probability is then calculated as the ratio of the observed afterpulses to the total number of primary pulses detected. Due to the independence of afterpulse generation across different SPADs within the SiPM, the total probability of afterpulsing following N photo-electrons in a primary pulse is proportional to N, being simply N times the afterpulse probability for a single PE.

To further understand the behavior of afterpulses, their timing distribution can be investigated by collecting data on the time delays between the primary pulse and the subsequent afterpulses. These time intervals are typically plot-

ted as a histogram, which reveals the distribution of afterpulse occurrences over time. This distribution is often well-described by an exponential decay function, reflecting the underlying physical processes involved, such as the trapping and delayed release of charge carriers within the SiPM.

Dark Count Rate (DCR) refers to the rate at which the SPAD spontaneously generate pulses in the absence of incident light. These dark counts arise from thermally generated carriers that trigger avalanche events, mimicking a 1 PE signal produced by a real photon. The rate of these thermally induced events is highly dependent on the temperature and the operating voltage of the SiPM. These events are independent of the number of PEs in the signal, meaning they occur at a consistent rate before and after the laser pulse. To determine this rate without conflating it with other types of noise, we measure these events in the pre-trigger region, the section of the acquisition window preceding the laser pulse. The DCR for ReD SiPMs were evaluated independently, as shown in Fig. 3.18. All channels exhibit a DCR of approximately 10^3 Hz, with the exception of the bottom channels 8 to 11, which are summed, and one malfunctioning SiPM from the top tile, channel 16.

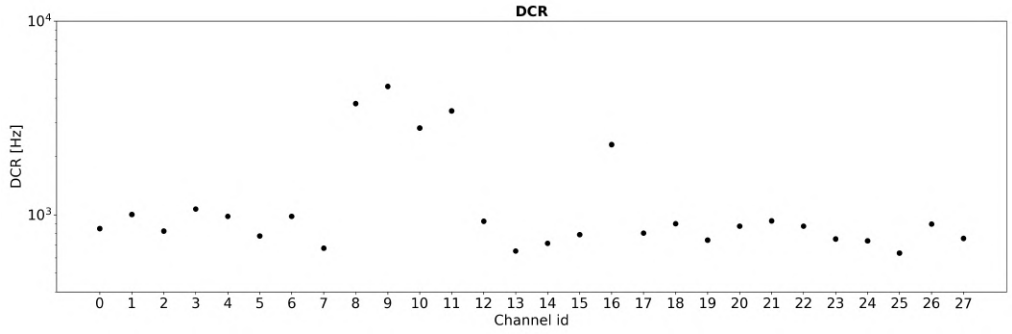

Figure 3.18: The Dark count rate calculated in the pre-trigger region across all ReD channels

3.7 Trigger and Data Acquisition

The data acquisition (DAQ) system consists of three CAEN V1730 Flash ADC boards, each capable of handling 16 signal output channels. These boards feature a 14-bit resolution, an input range of 2 V peak-to-peak, and a sampling rate of 500 MHz [95].

The system digitizes waveforms from all the detectors in the experimental setup, namely the two BaF_2 detectors, 28 SiPMs in the TPC, and 18 PScis, at a sampling rate where each sample corresponds to 2 ns. Each recorded waveform is composed of 50,000 samples waveforms, corresponding to a total duration of 100 µs, with the initial 5,000 samples (10 µs) captured prior to the

hardware trigger to establish the baseline and its fluctuations. This extended acquisition window is set to accommodate for the maximum drift time of 55 µs, which is the time required for an ionization electron generated at the bottom of the TPC to reach the top SiPMs under the applied drift field of 200 V/cm.

The hardware trigger logic is fired upon the coincidence between signals from one of the BaF_2 detectors and one of the PScis, within a coincidence window of 200 ns. This timing window is optimized to capture the full neutron spectrum emitted by the ^{252}Cf source. A valid signal is registered when it exceeds the DAQ thresholds, which were set above the noise level, considering the possible change in the baseline noise.

CHAPTER IV

Data Analysis and Results

In the previous chapter, we motivated the investigation of low-mass dark matter, emphasizing the constraints faced by liquid argon (LAr) time projection chambers (TPCs) in exploring this low-energy regime due to the limited understanding of the LAr response in that region. We subsequently introduced the ReD experimental setup, specifically designed to characterize the LAr response to low-energy nuclear recoils (NRs). Following this, we described the components of the setup and the calibration procedures undertaken during the commissioning phase for all detectors, namely barium fluoride (BaF_2), the plastic scintillators (PScis), and the TPC. Additionally, we outlined the triggering scheme implemented within the data acquisition (DAQ) system. This setup operated from January 10^{th} to March 16^{th}, 2023, successfully accumulating over 10 million events.

In this chapter, I will thoroughly explain the analysis conducted to characterize the ionization yield within the $2 - 10\,\text{keV}_{nr}$ range. It is important to highlight that the ReD working group has its own software for reconstructing physics parameters, which provided the necessary inputs to my analysis. However, the analysis work presented in this chapter, unless otherwise noted, was conducted by me, although I benefited from insightful discussions within the collaboration.

4.1 Candidate Neutrons Selection

The first objective of the analysis is to select a clean sample of neutron events that are in coincidence with the three detectors, namely BaF_2, TPC, and PScis. This was achieved based on BaF_2-PSci ToF and PSci f_{prompt}.

4.1.1 BaF_2-PSci Time-of-Flight (ToF)

The waveforms recorded from all detectors are processed through a pulse-finding algorithm that employs a moving average technique. This custom algorithm accurately detects the peak of the prompt component. Once the peak is identified, the algorithm calculates the interpolated time at a fixed threshold relative to the peak's maximum value.

Upon analyzing the acquired data, it was observed that the internal clocks of the DAQ boards were asynchronous, leading to event-wise timestamp discrepancies across the three boards. To address this temporal misalignment, the timestamps of each event recorded by Board 1 and Board 2 were corrected by aligning them with the reference timestamp from Board 0, thereby ensuring precise synchronization across all boards.

In the subsequent analysis, we focused on events where a single peak is observed on only one PSci. For these events, we calculated the time difference between the PSci peak and all the BaF_2 peaks associated with the same event, treating BaF0 and BaF1 separately. Histograms of these time differences (dt) for each PSci were generated for each run, as depicted in the top panel of Fig. 4.1. From these histograms, we identified the time bin with the highest event count for each run. These events are expected to be γ-rays, which are produced in greater abundance compared to neutrons. This expectation is based on the fact that a single spontaneous fission event from the ^{252}Cf source typically results in the emission of approximately three neutrons and an average of six to seven γ-rays. Furthermore, they will be seen later to have an f_{prompt} coinciding with that of *gamma*s. Consequently, this time bin with the highest event count is expected to be consistent across all runs, as it reflects the ToF taken by γ-events from the ^{252}Cf source, which can be calculated roughly as $t = d_{BaF-PSci}/c = 6.52\,\text{ns}$, where c is the speed of light. However, it was observed to vary among runs, as shown in the bottom panel of Fig. 4.1. To address this discrepancy along with other expected detector-wise variability due to different cable lengths and amplifier responses, two types of offsets were defined.

- The channel offset (μ_i) should vary between individual detectors (i) but remain constant across all runs. This offset accounts for different cable lengths and amplifier responses.
- The board offset (η_{jk}) should be fixed for detectors on the same board (j) but vary from run to run (k), in order to account for the arbitrary offset between the DAQ boards caused every time a new run starts.

To achieve accurate results, it was essential to simultaneously determine μ_i and η_{jk} for all runs in the campaign to adjust dt so that it matches the ToF expected for direct γ-events (dt_γ), such that:

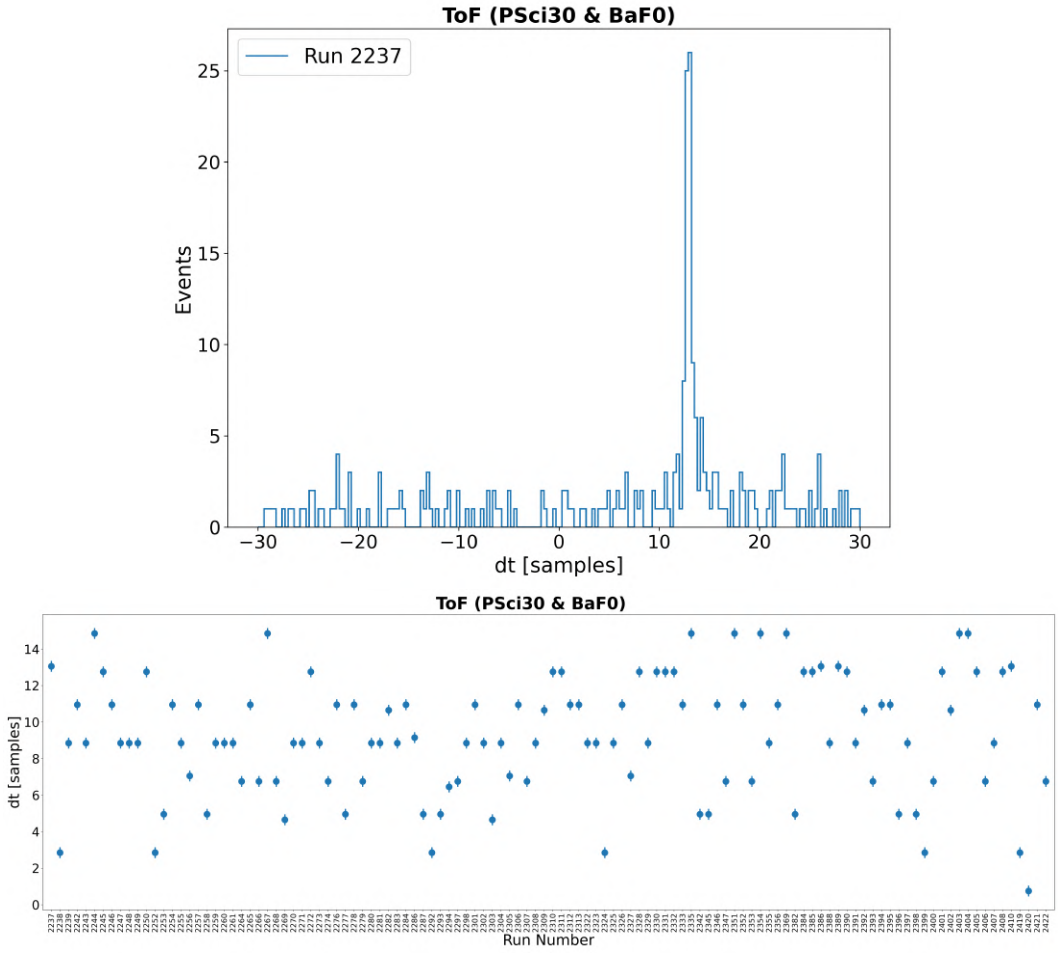

Figure 4.1: The calculated time difference (dt) between PSci30 and BaF0 peaks in one run (*top*) and all runs (*bottom*) with a bin width of 0.32 ns which will be used as the error for the simultaneous fit used to derive the offsets. Time is expressed in units of samples, with each sample corresponding to 2 ns.

$$dt + \mu_i + \eta_{jk} = dt_\gamma.$$

This simultaneous least-squares fit yielded the offsets needed to correct the calculated ToF with respect to BaF0, as illustrated in Fig. 4.2.

The offsets calculated so far are with respect to BaF0; however, we calculated the ToF as well from BaF1 which resides on the same DAQ board as BaF0. Therefore, we only need to evaluate the channel offset (μ_i). This was accomplished by applying the offsets evaluated with respect to BaF0 on BaF1-PSci coincidence events, as illustrated in Fig. 4.3. The offset for BaF1 was then determined by evaluating the difference between the two peaks, resulting in a BaF1 offset of 2.59 [sample], i.e. 5.18 ns.

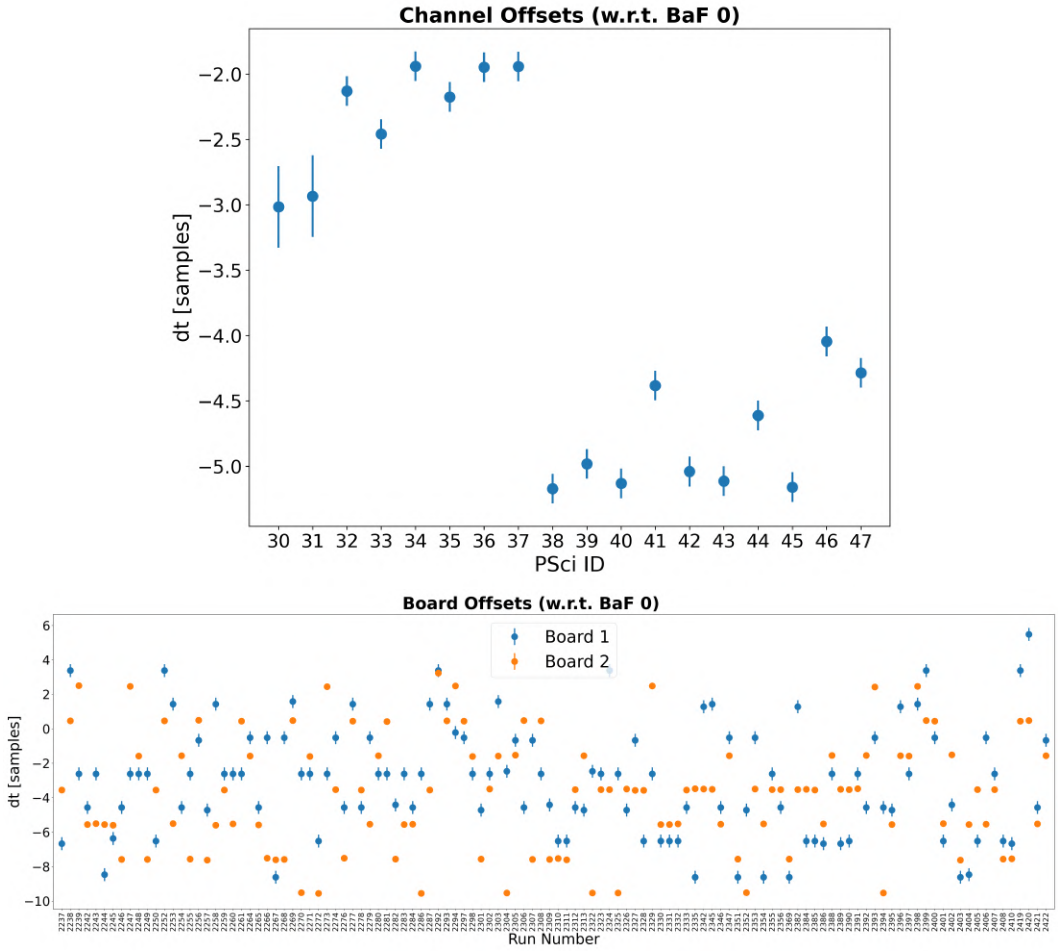

Figure 4.2: The channel (*top*) and board (*bottom*) offsets w.r.t. BaF0 derived from the gamma flash of ^{252}Cf, which will be used to correct the calculated ToF across the campaign runs.

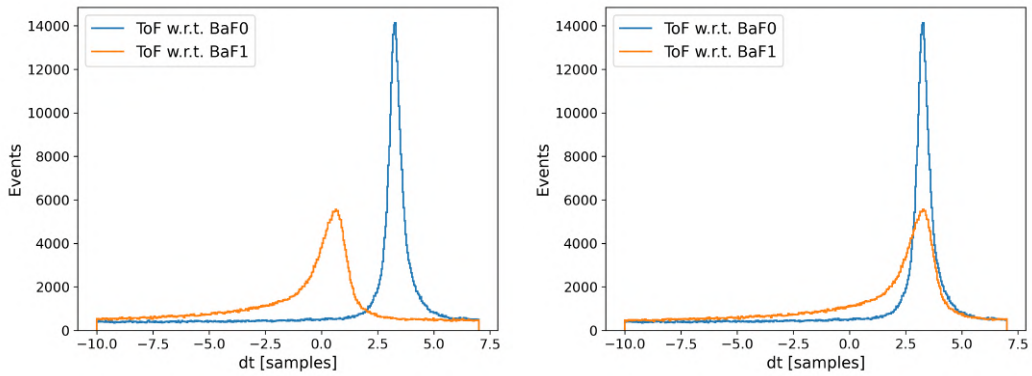

Figure 4.3: BaF1-PSci coincidence events before (*left*) and after (*right*) BaF1 channel correction

The response of the two BaF_2 detectors vary due to the different photomultiplier tubes (PMTs) connected to them. The PMT linked to BaF1 exhibits a broader prompt peak at low trigger thresholds compared to the one associated with BaF0. This discrepancy is due to the superior quantum efficiency of the PMT linked to BaF0 in the ultraviolet range compared to the PMT connected to BaF1. Consequently, this variation in PMT performance results in a broader and non-Gaussian ToF peak for coincidence events with BaF1. Therefore, the ToF uncertainty is evaluated by the RMS of the Gaussian fit and the FWHM of the γ-flash peak, as depicted in Fig. 4.4. This results in standard deviations of 0.6 ns and 1.4 ns for BaF0-PScis ToF and BaF1-PScis ToF, respectively. To assemble the final sample of candidate neutrons, we select all events that triggered BaF0 exclusively, as well as those that triggered BaF1 exclusively. For events common to both detectors, we use ToF relative to BaF0, which offers superior time resolution.

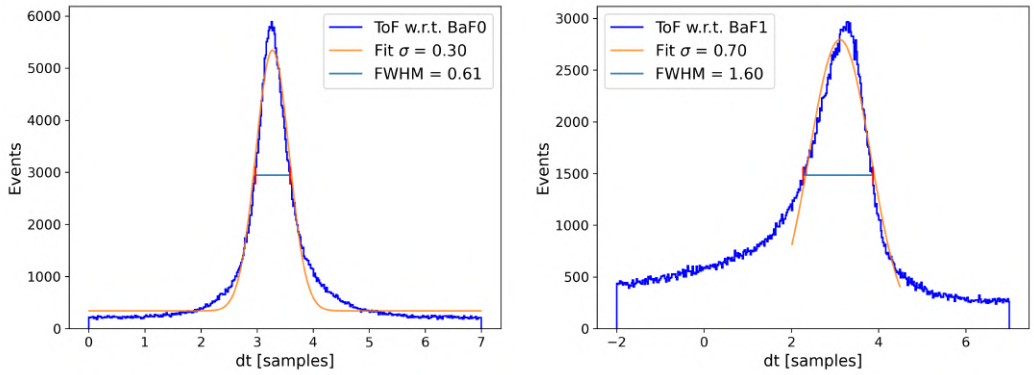

Figure 4.4: The ToF resolution for BaF0-PScis (*left*) and BaF1-PScis (*right*).

4.1.2 PScis f_{prompt}

Due to the Pulse Shape Discrimination (PSD) capability of PScis, we can examine the f_{prompt} vs. ToF parameter space, depicted in the left panel of Fig. 4.5. In this parameter space, the gamma and neutron populations are distinctly separated. Gamma events exhibit higher f_{prompt} values, while neutrons appear as a cluster of particles arriving after the gamma flash, shown in the right panel of Fig. 4.5, with lower f_{prompt} values.

Our objective is to have less than 0.01 % contamination of γ events in the signal dataset of candidate neutrons. This is achieved by implementing an energy-dependent cut on the PSci f_{prompt} parameter. The detailed procedure involves the following steps:

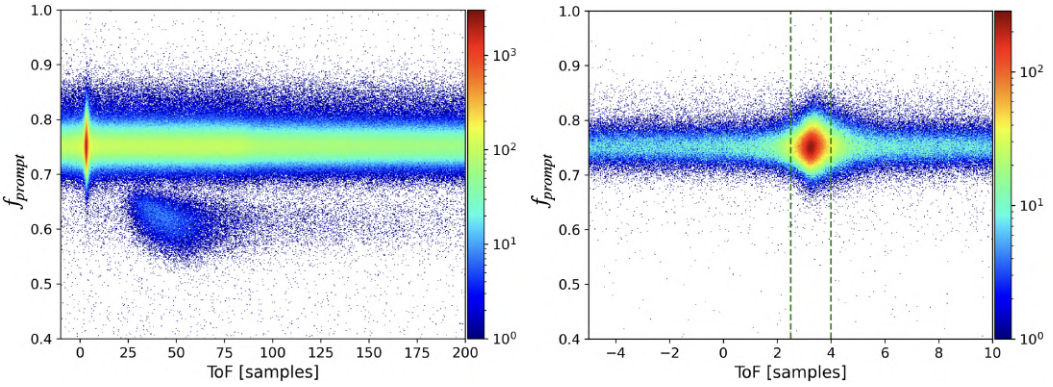

Figure 4.5: The figures show the f_{prompt} vs. ToF parameter space. On the (*right*), it is zoomed on the gamma flash with the vertical green dashed lines showing the selection used to build the f_{prompt} vs. Energy 2D Histogram.

- We select the gamma flash events based on the ToF within the range [2.5, 4] [sa], as indicated by the two vertical green dashed lines on the right panel of Fig. 4.5.
- Construct a 2D Histogram of f_{prompt} vs. Energy with and without the ToF selection, as illustrated in the left panel of Fig 4.6. The population with f_{prompt} near 0.85 is still under investigation. While Cherenkov light is a plausible explanation, a subset of these events may be attributed to noise or mis-reconstructed events. Nevertheless, they do not meet the selection criteria for our candidate neutrons.
- For each energy bin of the f_{prompt} vs. Energy with the ToF selection, calculate the cumulative sum of the total count of events up to each f_{prompt} value within that energy bin.
- Normalize this cumulative sum by the total count of events within that energy bin. In other words, convert the cumulative sum into a cumulative distribution function (CDF), which ranges from 0 to 1.
- Determine the f_{prompt} value where the CDF first meets or exceeds the required contamination threshold of 0.01 %.
- Record this f_{prompt} value for the corresponding energy bin. This value represents the cut-off point for that particular energy bin to limit γ contamination.
- Fit the recorded f_{prompt} values across energy bins with an exponential function defined as such:

$$y = a - b \times \exp \frac{-(x-c)}{d},$$

where x and y are the energy in [ADC] and f_{prompt} respectively. While a, b, c, and d are free parameters determined by the least-squares fit, as shown in Fig. 4.7.

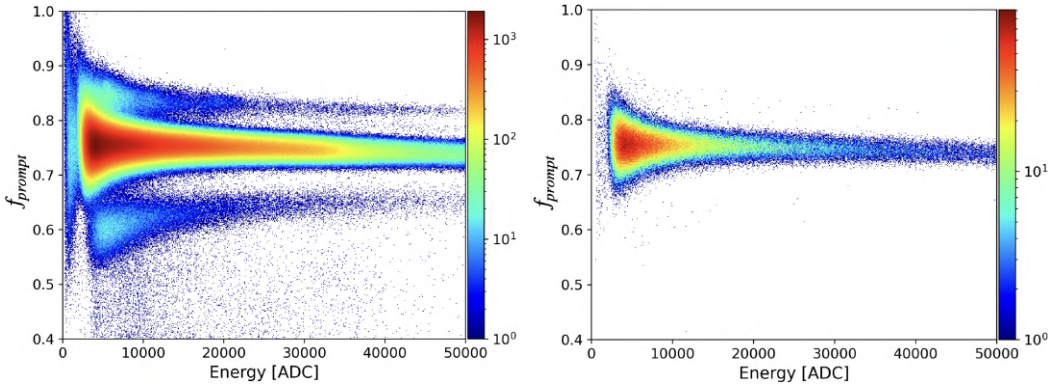

Figure 4.6: A 2D histogram of f_{prompt} vs. Energy with (*right*) and without (*left*) the ToF selection, which is intended to isolate the γ flash from the ^{252}Cf source.

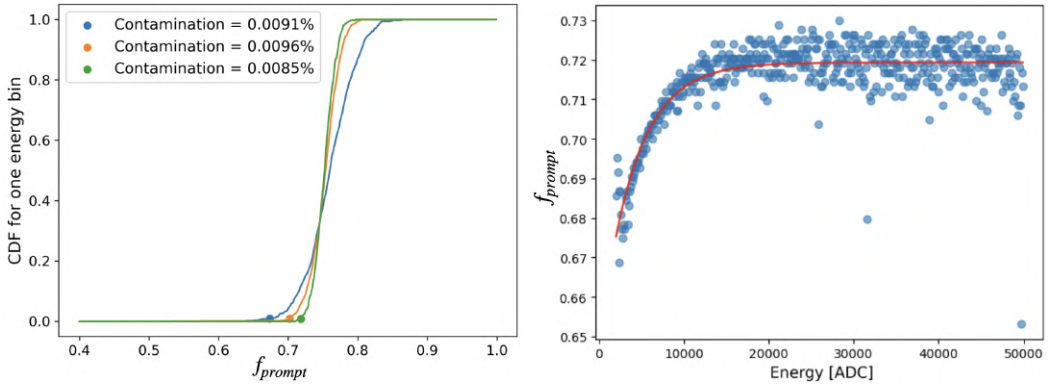

Figure 4.7: On the (*left*), the CDF of three energy bins with the scatter points indicating the f_{prompt} value at which there is a γ contamination of about 0.01 %. On the (*right*), it shows exponential fit in (*red*) used to define the energy-dependent f_{prompt} cut.

By following these steps, we can effectively reduce the γ contamination in the neutron candidate dataset. This can be seen once we employ this f_{prompt} cut along with a ToF selection from 40 to 180 ns, as depicted in Fig 4.8.

4.2 Kinetic Energy of Incoming Neutrons

Upon identifying the signal dataset of candidate neutrons, we search for those leaving a valid S2 signal in the TPC. Events displaying both S1 and S2 signals

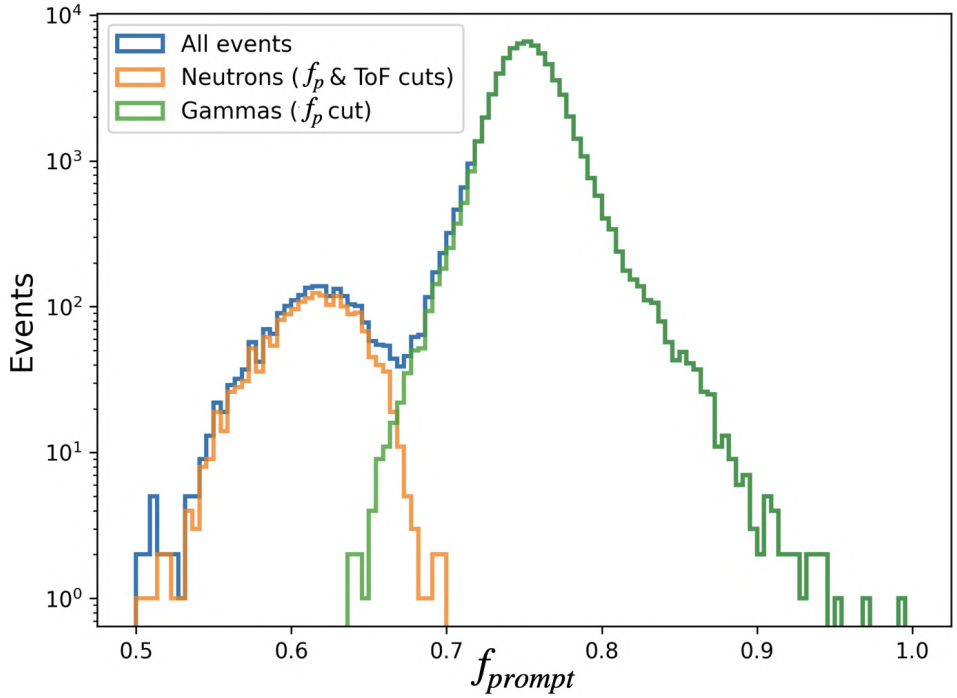

Figure 4.8: A f_{prompt} histogram showing the effect of employing the ToF and energy-dependent f_{prompt} cuts on separately identifying the neutrons, in (*orange*), and gammas, in (*green*), populations.

are excluded, as they predominantly arise from multiple neutron scatterings, a conclusion that has been corroborated by Monte Carlo simulations. This exclusion criterion ensures the accuracy and reliability of the subsequent kinetic energy reconstruction process.

The kinetic energy of the incoming neutrons can then be reconstructed on an event-by-event basis. This relies on determining the path length and the time taken by the neutrons to travel from the ^{252}Cf source to the PSci, passing through an interaction point within the TPC.

To determine the distance involved in the neutron's journey, we use the xy position estimated based on the pattern of the S2 signal among the top SiPMs. Due to the absence of the S1 signal, the z-coordinate is estimated as

$$z = \frac{1}{2} h_{TPC} - \left(\frac{t_{drift}}{t_{drift}^{max}} \right) h_{TPC},$$

where h_{TPC} is the height of the TPC, and t_{drift} is the time difference between the first photo-electron signal time of the S2 pulse and the triggered BaF time. The maximum drift time, t_{drift}^{max}, is 55 µs, which corresponds to the time required for an ionization electron generated at the bottom of the TPC to reach the top SiPMs under an applied drift field of 200 V/cm. This estimation of the

z-coordinate can be validated by examining Fig. 4.9. The left panel shows the distribution of the z-coordinate, which is confined within the TPC boundaries at $Z = -2.5$ and $Z = 2.5$, exhibiting a mostly uniform distribution. The right panel presents the drift time (t_{drift}) for the neutron sample, initially shown in *blue* after applying only the f_{prompt} cut, where some gamma leakage is still present, characterized by shorter drift times. The *orange* curve represents the distribution after applying all the selection criteria in Fig. 4.11, particularly the ToF cut, which effectively reduces the gamma contamination. The sharp decline in the final sample at 55 µs indicates the maximum drift time, t^{max}_{drift}.

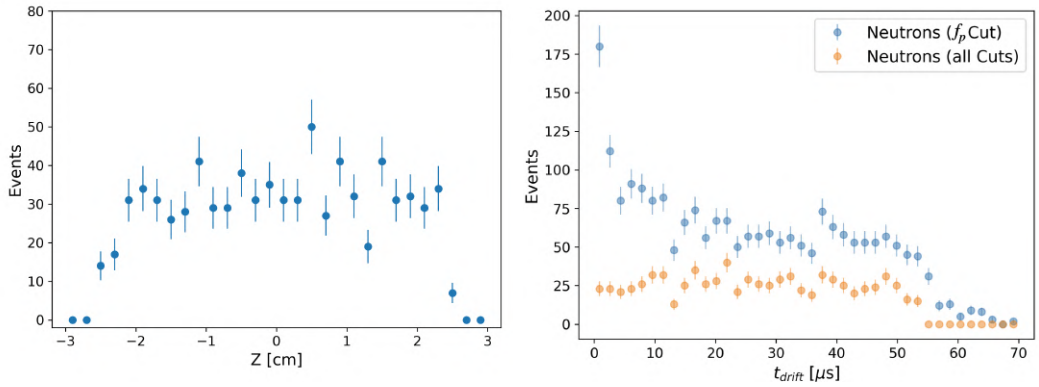

Figure 4.9: *Left*: The z-coordinate distribution of the neutron sample after employing all quality cuts, where the sharp cutoffs at $Z = -2.5$ and $Z = 2.5$ correspond to the boundaries of the TPC. *Right*: The distribution of drift time (t_{drift}) for the neutron sample just after applying the f_{prompt} cut discussed in the previous section in *blue*, and the neutron sample after employing all quality cuts in *orange*. The abrupt decrease in the final sample at 55 µs indicating the maximum drift time, t^{max}_{drift}.

These estimated xyz coordinates summed with the position of the TPC center at $(92.1, 0, 0)$ cm would represent the interaction point of the neutron inside the TPC with respect to the ^{252}Cf source position, taken to be fixed at the *origin*. We then construct vector $\vec{V}_1$ as the difference between the interaction point and the ^{252}Cf source position. The magnitude of $\vec{V}_1$ represents the distance traveled by the neutron before interacting inside the TPC. Similarly, vector $\vec{V}_2$ is constructed as the difference between the PSci position that detected the scattered neutron and the interaction point within the TPC. The coordinates of the PScis are given in Tab. 4.1. By summing the magnitudes $\vec{V}_1$ and $\vec{V}_2$, the total path length (d) traveled by the neutron is obtained. Using the BaF-PSci ToF (t_{BP}) and the calculated path length, we determine the kinetic energy of the incoming neutron based on relativistic principles.

$$\mathrm{KE}^{in}_{n} = m_n(\gamma - 1),$$

where γ is the Lorentz factor given by $1/\sqrt{1-\left(\frac{v}{c}\right)^2}$, with v being the velocity of the neutron, defined as $v = d/t_{BP}$ and c representing the speed of light.

Figure 4.10 shows the kinetic energy calculated on an event-by-event basis for the candidate neutrons with an S2 signal in the TPC.

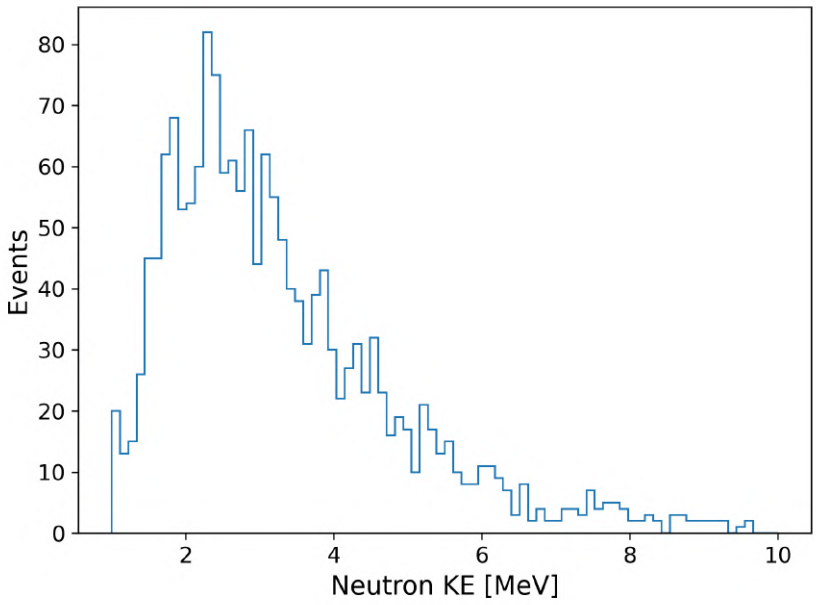

Figure 4.10: The incoming neutrons kinetic energy calculated on an event-by-event basis for the candidate neutrons with an S2 signal in the TPC.

Furthermore, vectors $\vec{V_1}$ and $\vec{V_2}$ can be used to determine the angle at which the neutron is scattered after its interaction in the TPC. This angle is calculated in radians using the formula:

$$\theta_{scatt} = \arccos\left(\frac{\vec{V_1}\cdot\vec{V_2}}{\|\vec{V_1}\|\|\vec{V_2}\|}\right).$$

Given the kinetic energy of the incoming neutron (KE_n^{in}) and the scattering angle of the outgoing neutron (θ_{scatt}) after its collision with an argon atom inside the TPC, the recoil energy (E_{rec}) of the argon atom is evaluated on an event-by-event basis. Initially, the momentum of the incoming neutron (p_n^{in}) is derived from its kinetic energy using the relation:

$$p_n^{in} = \sqrt{2m_n \mathrm{KE}_n^{in}}. \tag{4.1}$$

PSci ID	x (cm)	y (cm)	z (cm)
30	195.5	-4.5	31.7
31	195.5	0.0	31.7
32	195.5	4.5	31.7
33	195.5	-4.5	27.2
34	195.5	0.0	27.2
35	195.5	4.5	27.2
36	195.5	-4.5	22.7
37	195.5	0.0	22.7
38	195.5	4.5	22.7
39	195.5	-4.5	-22.7
40	195.5	0.0	-22.7
41	195.5	4.5	-22.7
42	195.5	-4.5	-27.2
43	195.5	0.0	-27.2
44	195.5	4.5	-27.2
45	195.5	-4.5	-31.7
46	195.5	0.0	-31.7
47	195.5	4.5	-31.7

Table 4.1: The positions of the PScis with respect to the ^{252}Cf source which is taken to be at the *origin*, i.e. at $x = y = z = 0$. The TPC center is at $(92.1, 0, 0)$ cm.

Subsequently, based on two-body kinematics, fully derived in Appendix A, the approximate momentum of the outgoing neutron (p_n^{out}) is expressed by:

$$p_n^{out} = p_n^{in} \frac{m_n}{m_n + m_{Ar}} \left[\cos\theta_{scatt} + \sqrt{\cos^2\theta_{scatt} + \frac{m_{Ar}^2}{m_n^2} - 1} \right]. \tag{4.2}$$

Once the outgoing neutron momentum is determined, its corresponding kinetic energy can be expressed as:

$$\mathrm{KE}_n^{out} = \frac{p_n^{out^2}}{2m_n}. \tag{4.3}$$

Finally, the recoil energy of the argon atom is then calculated as the difference between the incoming and outgoing kinetic energies of the neutron:

$$E_{rec} = \mathrm{KE}_n^{in} - \mathrm{KE}_n^{out}. \tag{4.4}$$

In order to ensure that the S2 events in the TPC are true coincidences not just mere accidentals, some cuts were needed. The effect of these quality cuts can be seen in Fig. 4.11. In particular, "TPC accedintals Cut" is essential to get rid of the neutrons scattering in inactive parts of the set up or the S2

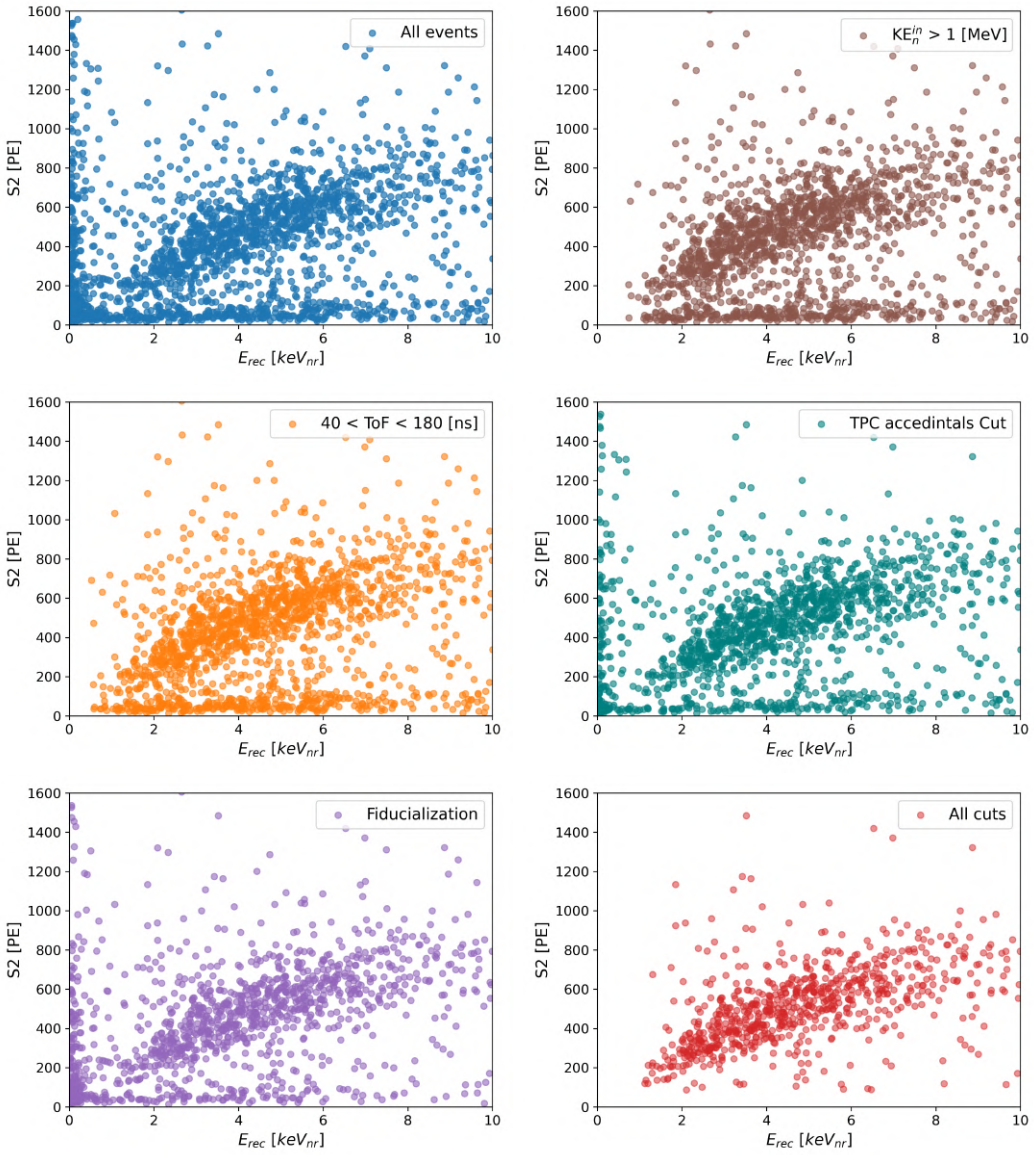

Figure 4.11: The recoil energy of the argon atom calculated on an event-by-event basis. In *blue*, we display all events coincident in the three detectors, namely BaF_2, TPC, and PScis. In *brown*, we require the calculated kinetic energy of the incoming neutron to be more than 1 MeV. In *orange*, the BaF_2–PSci ToF is within a range capturing the entire ^{252}Cf neutron spectrum are presented. In *cyan*, we employ cuts to eliminate the TPC background events. In *purple*, only events within the central 4x4 cm^2 region of the TPC are retained. In *green*, the final sample of events surviving all the selection criteria.

tails of high energy events. Such events are effectively rejected by a cut of the S2 start and stop times and by requiring that the SPE rate in the pre-S2 time window to be compatible with dark noise. "Fiducialization" refers to a cut applied to the xy-coordinates, selecting only events that occur within the central 4x4 cm^2 region of the TPC.

4.3 Systematic Uncertainties on E_{rec}

Experimental physics is inherently subject to systematic uncertainties, which arise from the finite resolution of the measurement instrumentation. Addressing these uncertainties is crucial for both experimental design and data analysis since they can influence the accuracy and reliability of experimental results. Therefore, their careful identification, quantification, and minimization are essential for robust scientific conclusions.

In this section, the impact of measurement uncertainties in neutron scattering angle, ToF, and path length on the calculation of final recoil energy will be investigated. This analysis will involve performing error propagation based on Eq. 3.1, enabling us to quantify how variations in these parameters influence the accuracy of the recoil energy determination. The error propagation equation can be expressed as:

$$(\delta E_{\mathrm{rec}})^2 = \left(\frac{\partial E_{\mathrm{rec}}}{\partial \theta_{\mathrm{scatt}}}\delta\theta_{\mathrm{scatt}}\right)^2 + \left(\frac{\partial E_{\mathrm{rec}}}{\partial t}\delta t\right)^2 + \left(\frac{\partial E_{\mathrm{rec}}}{\partial d}\delta d\right)^2. \tag{4.5}$$

Subsequently, we can compute the partial derivatives of the preceding equation according to Eq. 3.1, resulting in:

$$\begin{aligned}
\frac{\partial E_{\mathrm{rec}}}{\partial \theta_{\mathrm{scatt}}} &= m_{\mathrm{n}}\left(\frac{d}{t}\right)^2 \frac{m_{\mathrm{n}}m_{\mathrm{Ar}}}{(m_{\mathrm{n}}+m_{\mathrm{Ar}})^2}\sin\theta_{\mathrm{scatt}},\\
\frac{\partial E_{\mathrm{rec}}}{\partial t} &= -2m_{\mathrm{n}}\left(\frac{d}{t}\right)^2 \frac{m_{\mathrm{n}}m_{\mathrm{Ar}}}{(m_{\mathrm{n}}+m_{\mathrm{Ar}})^2}\frac{1}{t}(1-\cos\theta_{\mathrm{scatt}}),\\
\frac{\partial E_{\mathrm{rec}}}{\partial d} &= 2m_{\mathrm{n}}\frac{d}{t^2}\frac{m_{\mathrm{n}}m_{\mathrm{Ar}}}{(m_{\mathrm{n}}+m_{\mathrm{Ar}})^2}(1-\cos\theta_{\mathrm{scatt}}).
\end{aligned}$$

These expressions can be simplified to emphasize the relative uncertainties by normalizing with E_{rec}, leading to:

$$\frac{\partial E_{\mathrm{rec}}}{E_{\mathrm{rec}}} = \frac{\sin\theta_{\mathrm{scatt}}}{1-\cos\theta_{\mathrm{scatt}}} = \cot\left(\frac{\theta_{\mathrm{scatt}}}{2}\right)\partial\theta_{\mathrm{scatt}}, \tag{4.6}$$

$$\frac{\partial E_{\mathrm{rec}}}{E_{\mathrm{rec}}} = \frac{-2}{t}\partial t, \tag{4.7}$$

$$\frac{\partial E_{\mathrm{rec}}}{E_{\mathrm{rec}}} = \frac{2}{d}\partial d. \tag{4.8}$$

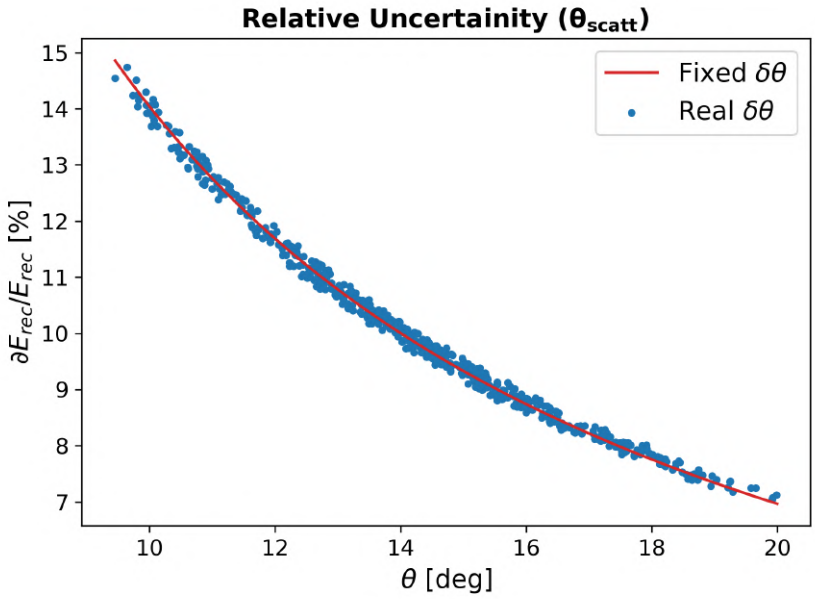

Figure 4.12: The relative uncertainty in the recoil energy, resulting from the uncertainty in the scattering angle (θ_{scatt}). The *solid red line* depicts interactions occurring at the center of the TPC. In contrast, the *blue scatter points* represent the true interaction points on an event-by-event basis for the final neutron sample.

The PScis have a diameter of 1 inch. In our calculation we always assume that the scattered neutron hits exactly the center of the PScis. Thus, the scattering angle uncertainty, denoted as $\delta\theta_{\text{scatt}}$, can be approximated as the ratio of the PSci's radius (r_{PSci}) to the distance (L) from the scattering point within the TPC to the PSci detector.

$$\delta\theta_{\text{scatt}} = \frac{r_{\text{PSci}}}{L} \approx \frac{2.54/2}{103.4} = 1.23\%$$

Subsequently, Eq. 4.6 can be employed to compute the relative uncertainties ($\partial E_{\text{rec}}/E_{\text{rec}}$) as depicted in Fig. 4.12. In this figure, the red solid line represents calculations made using the distance from the center of the TPC to the holding frame of the PSci detectors. In contrast, the blue scatter points correspond to event-by-event calculations, considering the distance from the interaction point within the TPC to the PSci that detected the scattered neutron. Examination of the y-axis reveals that the relative uncertainties vary within 7 – 15 % across the range of scattering angles associated with our candidate neutrons.

The uncertainties associated with the ToF measurement has been evaluated with respect to BaF0 and BaF1, as shown in Fig. 4.4, yielding values of 0.6 ns and 1.4 ns, respectively. To ensure a more conservative estimate in

this analysis, the ToF uncertainty (δt) is taken as 1.4 ns. Then, by employing Eq. 4.7, the impact of this ToF resolution on the calculated recoil energies produced by our neutron candidates can be determined, as illustrated in the left panel of Fig. 4.13. The results indicate that for recoil energies below 4 $\mathrm{keV_{nr}}$, the uncertainty in the ToF measurement contributes to a relative uncertainty ranging within 2 – 4.5 %, with greater accuracy observed at lower energies. Across the full range of recoil energies, the uncertainty remains below 5.5 %, highlighting a generally robust measurement.

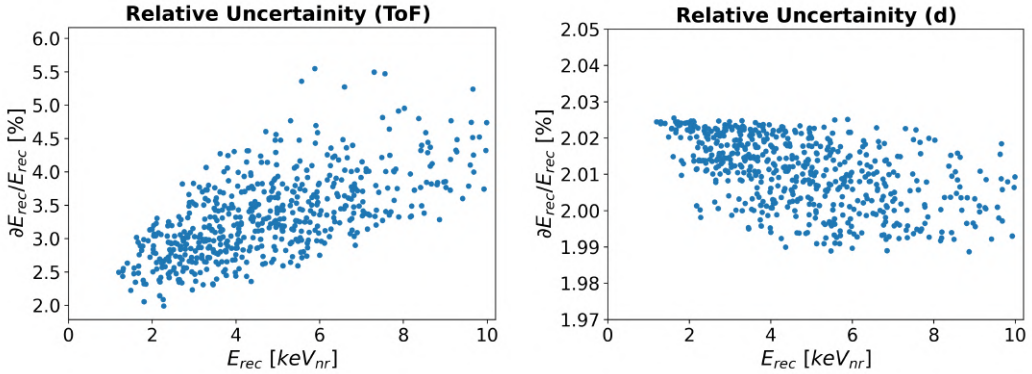

Figure 4.13: The relative uncertainty in the recoil energy, arising from uncertainties in ToF measurement (*left*) and the path length (*right*). The relative uncertainty is plotted as a function of recoil energy on the x-axis, illustrating the variation in accuracy across the range of recoil energies produced by the final neutron sample.

In a similar manner, the effect of the path length uncertainty on the recoil energy is considered and depicted in the right panel of Fig. 4.13. Assuming a path length uncertainty, δd, of 2 cm, which is likely an overestimation, we find that this would result in an approximately 2 % uncertainty across the entire range of recoil energies produced by the final neutron sample. This consistent level of uncertainty suggests that the impact of path length variability on the overall accuracy of the recoil energy estimation is relatively minimal.

By substituting the expressions for the partial derivatives and associated uncertainties into Eq. 4.5, we obtain the total relative uncertainty in the recoil energy, accounting for the contributions from measurement uncertainties of the scattering angle, ToF, and path length. The calculated total relative uncertainty is conservatively below 16 %, corresponding to an error margin of ± 0.32 keV at a recoil energy of 2 keV, and ± 1.6 keV at a recoil energy of 10 keV.

4.4 Determination of the g_2 Factor

As mentioned in Sec. 2.4.2, the gain factor for the S2 signal, denoted as g_2, quantifies the conversion of ionization electrons into detectable photo-electrons. This is a detector-dependent quantity measured in units of PE/$e-$ that depends on several key components:

- the extraction efficiency (η_{ext}), which represents the fraction of electrons extracted from the liquid into the gas phase. Typically, it is determined experimentally by measuring the ratio of the S2 to S1 signals under various conditions. It is influenced by the electric field in the liquid phase. This value can be determined through calibration runs using known sources, such as gamma or X-ray sources.
- the electroluminescence yield (Y_{el}), which describes the number of photons generated per electron in the gas phase under the applied electric field. A higher electric field leads to more photons per electron. Empirical models or simulations provide values for Y_{el} based on the field strength and geometry of the detector.
- the photon detection efficiency (PDE): this accounts for how efficiently the SiPMs array captures the produced photons. It includes factors like the coverage of the SiPMs, reflectivity of materials utilized in the TPC, and the intrinsic efficiency of the SiPMs. This is typically determined through a laser calibration of the SiPMs

The two primary methods for estimating g_2 are through echo events or the anti-correlation between S2 and S1 signals [74]. Echo events occur when photons from an S2 signal strike the cathode, releasing one or more additional electrons. These electrons are subsequently transported by the drift field, extracted, and accelerated, generating a delayed electroluminescence signal known as S3. Assuming the S3 signals arise from the release of one or two electrons, with each contributing a signal of g_2 photo-electrons, the resulting spectrum can be modeled as a sum of two Gaussian distributions with mean values of g_2 and $2g_2$, and standard deviations of σ and $\sqrt{2}\sigma$, respectively. This analysis is still ongoing. For this data-taking campaign in ReD, estimating the g_2 via the S2-S1 anti-correlation is not feasible due to the lack of measurements at varying electric fields, leaving the echo method as the only available approach. The necessity of determining g_2 can be bypassed by utilizing a well-characterized calibration source such as ^{37}Ar, which serves as an effective cross-calibration reference point. This approach allows for the direct determination of the ionization yield at low recoil energies, eliminating the need for extrapolations from higher-energy data, thereby enabling more accurate calibration while minimizing systematic uncertainties arising from non-linear detector responses in the low-energy region. A study of this approach is discussed in App. B.

A preliminary estimate of g_2 was obtained by employing a custom model that relates the S2/S1 ratio to S1 for ERs, which was tuned using DS-50 data and is dependent on both g_1 and g_2. By adjusting this model to fit the ReD data and fixing g_1 using the 60-keV gamma peak from ^{241}Am, we achieved strong consistency with a g_2 value of 17.2 PE/e^-. However, further work is ongoing to refine the g_2 value using only ReD data, without relying on cross-calibration with DS-50.

4.5 Ionization Yield (Q_y^{NR})

The objective of the low-energy calibration described in this dissertation is to determine the ionization yield (Q_y^{NR}) in detector-independent units, such as e^-/keV, which represents the number of extracted electrons per unit of nuclear recoil energy.

The analysis begins with the neutron data shown in Fig. 4.11, where all relevant quality cuts have been applied to ensure that these recoil events in the TPC are genuine coincidences and not just mere accidentals. Subsequently, the S2 signal, measured in photo-electrons, is divided by the preliminary estimate of the gain factor, g_2, which has been determined as 17.2 PE/e^-. The uncertainty on this value is still under active investigation and is not reported here. This conversion yields the y-axis in terms of the number of electrons, as depicted in the left panel of Fig. 4.14. Then, the number of electrons generated in each event is divided by the associated nuclear recoil energy to calculate the ionization yield on an event-by-event basis. This correlation between ionization yield and recoil energy can be visualized as a scatter plot in the right panel of Fig. 4.14.

The recoil energy on the x-axis was binned between 2 and 10 keV, with bins of 0.5 keV width. Energy bins above 10 keV were not computed due to insufficient statistics. For each energy bin, the median value of Q_y^{NR} and the standard error of the mean are computed. While the median serves as a reasonable estimator for the population, it may exhibit some bias due to the long tails in the Q_y^{NR} distribution; nevertheless, it provides a useful initial approximation. The standard error of mean is obtained by dividing the sample standard deviation (σ) by the square root of the number of data points (N) in the sample, where σ is given by:

$$\sigma = \sqrt{\frac{1}{N-1}\sum_{i=1}^{N}(x_i - \bar{x})^2}, \qquad \text{with} \qquad \bar{x} = \frac{1}{N}\sum_{i=1}^{N} x_i.$$

The use of $N-1$ in the denominator is often referred to as "Bessel's correction", which adjusts for the bias that occurs when using the sample mean $\bar{x}$ as an estimator of the population mean. Figure 4.15 shows the first four energy

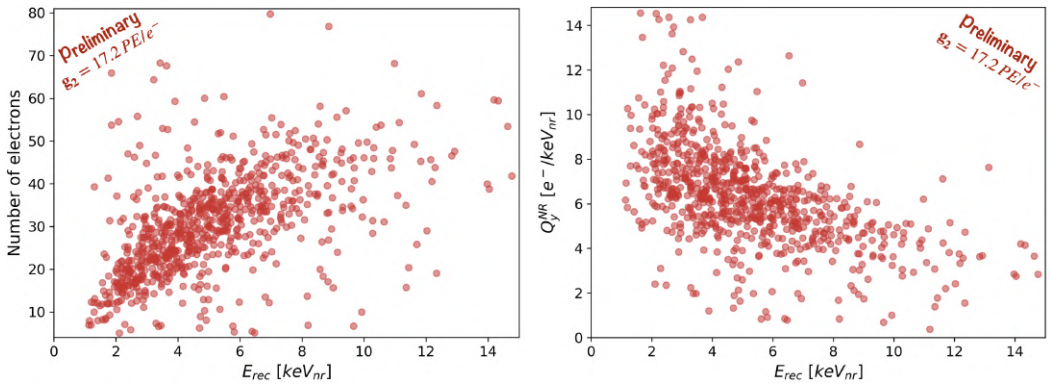

Figure 4.14: *On the left*: the figure shows the final neutron sample where all relevant quality cuts have been applied to ensure that these events represent genuine coincidences between all detectors. The y-axis is converted from photo-electrons to electrons using the preliminary value of $g_2 = 17.2$ PE/e^-. *On the right*: the figure depicts the correlation between the ionization yield and the recoil energy.

bins, where the computed median is depicted as a red vertical dashed line. The associated standard error of the mean is represented by a red band surrounding the median.

In examining Fig. 4.14, one can notice a wide spread of events around the densely populated region. These events need to be investigated thoroughly to determine whether they are caused by backgrounds or are related to the efficiency of the reconstruction algorithm. However, one can try to exclude these outliers and recompute the median and the standard error of the mean for the refined sample. This process would provide an estimate of the systematic uncertainty associated with the Q_y^{NR} values. Figure 4.16 demonstrates this approach; In the left panel, neutron events are shown in red, with outliers defined by eye and marked by blue crosses. The right panel compares the median and standard error of the mean, calculated with and without the outliers, depicted in red and green, respectively. The results suggest that systematic uncertainties are more pronounced at lower energies, approximately 7 %, but diminish at higher energies.

Finally, the ionization yield can be represented as a function of recoil energy utilizing the computed medians with error bars corresponding to the standard error of the mean. This data is compared with existing measurements from the literature, including those from DS-50 [75], ARIS [76], and Joshi et. al. [62] as shown in Fig. 4.17. This result demonstrates consistency with the measurements from ARIS and Joshi et. al., while suggesting that the ionization yields for energies below 5 keV are greater than those predicted by the DS-50 model. Notably, in the lowest energy bin, the observed ionization yield

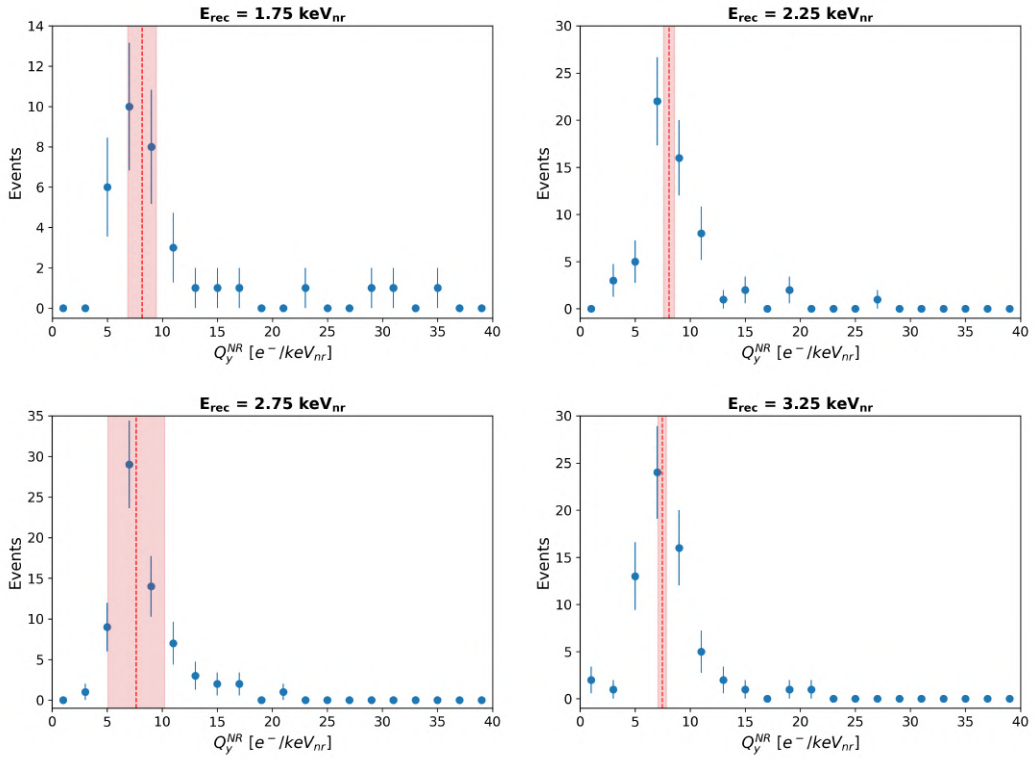

Figure 4.15: The Q_y^{NR} distribution in the first four energy bins. The median value for each bin is indicated by *a red dashed-line*, while the *red band* around the median represents the standard error on the mean.

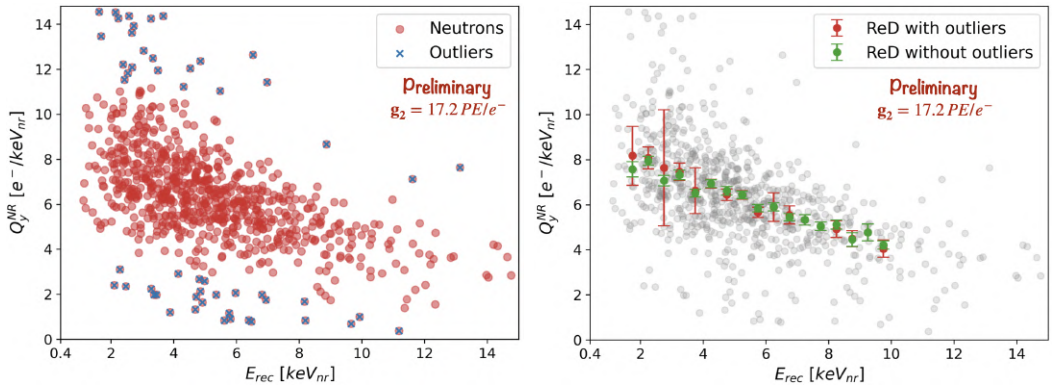

Figure 4.16: Analysis of systematic uncertainty in the ionization yield (Q_y^{NR}). *The left panel* displays neutron events as *red points*, with outliers identified by *blue crosses*. *The right panel* shows the median and standard error of the mean calculated both with (*red*) and without (*green*) the outliers.

is approximately 10 % higher than the DS-50 model's estimation. However, the uncertainty on Q_y^{NR} influenced by multiple factors, including the uncertainty on E_{rec}, the single-electron response of the SiPMs, the SiPMs noise level, and the g_2 parameter. Based on previous experience with ReD, DS-50 and ARIS, the systematic uncertainty associated with g_2 is expected to be significant, likely on the $\mathcal{O}(10-20\,\%)$. Therefore, this indicates that the error bars depicted in Fig. 4.17 might need to be enlarged accordingly.

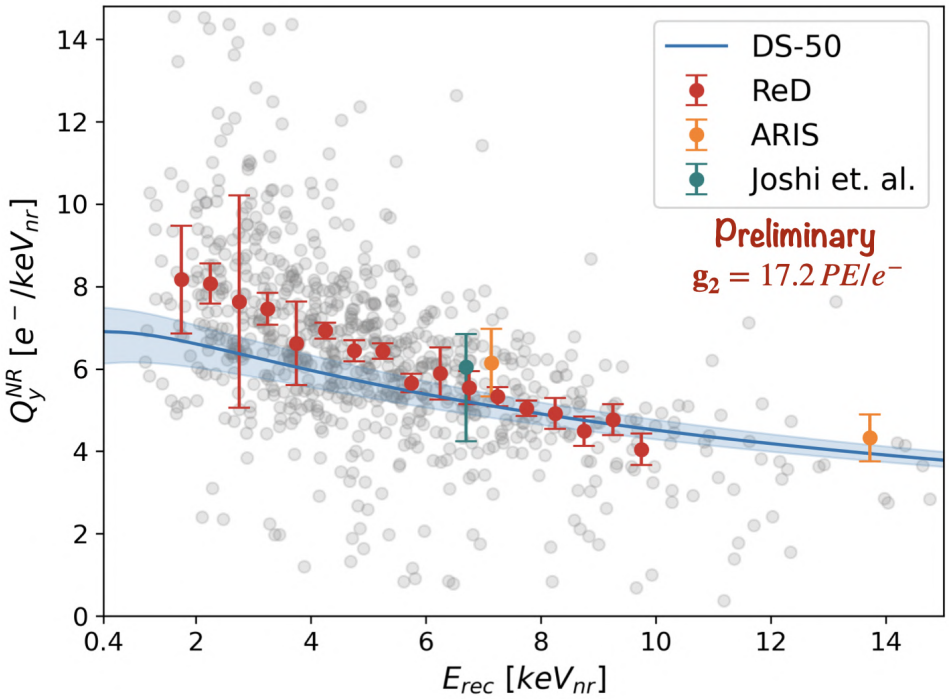

Figure 4.17: The ionization yield (Q_y^{NR}) as a function of the nuclear recoil energy. The ReD measurements are represented by *red* points and were calculated based on the preliminary value of $g_2 = 17.2$ PE/e^-. The DS-50 measurements are indicated by a *blue* line, with the associated uncertainties represented by *a blue shaded band* [75]. The ARIS dataset within this energy range is depicted in *orange* [76]. The Joshi et al. point[1]is illustrated in *teal* [62].

[1]After consulting with the authors, the data point is corrected for their single electron yield using the 2.82 keV K-shell capture of ^{37}Ar line from their experiment and DarkSide-50 as a cross-calibration point, private communication with T. H. Joshi and S. Sangiorgio (Feb. 2018) [96]

CHAPTER V

Conclusion & Further Work

The primary objective of this dissertation is to provide a comprehensive analysis of the liquid argon (LAr) response to low-energy nuclear recoils (NRs) within the $2 - 10\,\mathrm{keV}_{nr}$ range. This study encompasses the entire experimental procedure, spanning from the design and implementation of a setup capable of directly measuring low-enery NRs, to the complete data analysis pipeline. The outcome of this process is the determination of ionization yield, quantified in detector-independent units, specifically as the number of extracted electrons per unit of NR energy.

However, the analysis of the dataset obtained by the ReD experiment from January 10^{th} to March 16^{th}, 2023 is still ongoing. There are several critical areas where further refinement of data selection and analysis can enhance the precision and reliability of the ionization yield determination within the specified low-energy NR range. Key improvements under consideration include, but are not limited to, the following:

- Enhancing the timing accuracy of the barium fluoride (BaF_2) detectors by incorporating a more detailed consideration of the energy deposited in these detectors. This adjustment will improve the time-of-flight (ToF) measurements, which are crucial for constraining the bias introduced by timing uncertainties, thereby improving the overall temporal resolution of the system.

- Refining the analysis of the noise associated with the silicon photomultipliers (SiPMs). In particular, one of the top SiPMs exhibited an anomalously high dark count rate (DCR). Thus, excluding such problematic

SiPM will enhance the accuracy of signal detection and reduce false event contribution.

- Improving event selection through more stringent cuts to reject events that overlap with the tails of previous events. This step is crucial for reducing event contamination in the final sample of neutron candidates, especially when dealing with low-energy NR events where precise event identification is critical.

- Optimizing xy position reconstruction and correcting S2 values; Using ^{241}Am calibration data, improvements will be made to reconstruct the xy position of events more accurately. Furthermore, corresponding corrections will be applied to the S2 signals to account for any spatial dependencies observed in the detector's response.

- Implementing a new calibration curve of the plastic scintillators (PScis) that accounts for the non-linearity observed at low energy. This will ensure that the scintillator response is accurately characterized across the full energy range, improving the reliability of energy measurements for low-energy NRs.

- Ensuring consistency between data and Monte Carlo (MC) simulations: This involves investigating that the MC can reproduce all relevant observables to guarantee that the MC accurately represent the physical processes occurring in the detector.

- Examining the impact of using S2-only events while excluding the S1+S2 population. A systematic bias may be introduced if the events within a given recoil energy bin are originated solely from the S2-only dataset.

- Deriving the gain of the ionization signal (g_2) directly from ReD data using echoes instead of the cross-calibration with DS-50 that yielded the preliminary value of $g_2 = 17\,\mathrm{PE}/e^-$. This method requires a detailed modeling of the S2 pulse shape, as the S2 tails that extend into the echo region have a magnitude comparable to the echo pulse itself. A more accurate characterization of this behavior will lead to a more precise determination of g_2 and thus improve the overall measurement of the ionization yield.

In conclusion, LAr detectors have proven to be a highly promising technology for rare-event detection, particularly in the pursuit of dark matter, due to their exceptional sensitivity and scalability. Interactions of WIMPs in LAr would produce NRs $\mathcal{O}(0 - 100\,\mathrm{keV})$ depending on the WIMP mass. For low-mass WIMPs, this entails less energetic recoils, shifting the sensitivity threshold from the typical $20 - 100\,\mathrm{keV}$ to just a few keVs. Therefore, the accurate characterization of LAr response to such low-energy NRs is crucial, particularly to reduce the significant systematic uncertainties associated with

the intrinsic stochastic nature of the ionization process, and thereby enhance the overall sensitivity of LAr detectors.

The existing literature on ionization yield measurements in argon for low-energy NRs is notably limited, with the lowest data points reported by Joshi et al. [62] and ARIS [76], which measured yields at 6.7 keV and 7 keV, respectively. Additionally, the DarkSide-50 experiment modeled the ionization yield down to 0.5 keV_{nr} using the Geant4 simulation framework, incorporating calibration data from AmBe and AmC sources to develop a two-parameter model [75]. However, this model's accuracy is influenced by ionization quenching effects, where fluctuations can significantly impact the probability of detecting events near the threshold. To address these challenges, the ReD experiment employed a two-body kinematic approach, achieving a direct measurement of ionization yield down to $1 - 2\,\mathrm{keV}_{nr}$. A preliminary analysis of the ReD study resulted in a consistency with measurements from ARIS and Joshi et al., while indicating a higher yield than predicted by the DS-50 model for recoil energies below $5\,\mathrm{keV}_{nr}$. However, the uncertainty on Q_y^{NR} is influenced by several factors, including uncertainties in E_{rec}, the single-electron response of the SiPMs, the SiPM noise level, and the parameter g_2. Previous analyses of ReD, DS-50, and ARIS suggest that the systematic uncertainty associated with g_2 is significant, likely on the $\mathcal{O}(10 - 20\,\%)$. Thus, the error bars in Fig. 4.17 may require adjustment.

This research would not have been possible without the efforts of the entire ReD working group, whose collective contributions were essential to the project's success. However, this dissertation is a reflection of my personal efforts, technical skills, and intellectual contributions, while also acknowledging the collaborative nature of the broader research effort. Over a seven-month period, I worked closely with the ReD local working group in Catania, Italy, where I collaborated extensively in preparing the experimental setup and commissioning key detectors. Specifically, I was involved in assembling the mounting frame for the PScis and performing critical hardware adjustments, such as replacing the anode and cathode windows of the Time Projection Chamber (TPC) in a cleanroom environment. During this period, my contributions extended to different aspects of the experimental procedures, including practicing the entire cryogenic system cool-down process. This involved enclosing the TPC in the cryostat, initiating the vacuum process, and overseeing the liquefaction of argon gas, which is critical for the proper operation of the detector. Furthermore, I was actively engaged in preliminary calibrations, working on the BaF_2 detectors, PScis, as well as conducting laser and source runs in the TPC. These steps were foundational in ensuring that the detectors operated at their optimal performance levels before the data-taking phase began.

In terms of analysis, the majority of the work presented in this dissertation, unless otherwise noted, was conducted by me, although I benefited from

insightful discussions within the collaboration. For instance, in Sec. 3.6, I developed a comprehensive laser calibration analysis based on ReD data. This analysis, constructed in collaboration with Prof. Davide Franco, was designed as part of the reconstruction algorithm that will be used in future work by the collaboration. Moreover, the entire content of Chapter 4, which involves a detailed analysis of the experimental data, represents my independent work. Although I incorporated feedback from internal discussions, I was solely responsible for the data analysis, interpretation, and presentation in this dissertation. It is important to highlight that the ReD working group developed its own software for reconstructing physics parameters, which provided the necessary inputs to my analysis. To ensure the robustness of these reconstructed variables, detailed MC simulations were employed. These simulations not only benchmarked the performance of the reconstruction algorithm but also generated synthetic data sets, which were critical for validating the entire analysis workflow. Many of the conclusions drawn in my analysis were directly motivated and informed by the insights gained from this comprehensive MC study.

Throughout the PhD project, I contributed actively at many stages during the whole procedure, from the physical assembly of the detector components to the execution of the calibration procedures, data taking and analysis procedures. Furthermore, an independent investigation was conducted into the on-demand production and deployment of the ^{37}Ar source as a cross-calibration point within the low-energy range. This study provided critical insights into the calibration of LAr response to low-energy nuclear recoil events. The results of this effort were published as a separate work by myself and are discussed in detail in App. B, where the methodology and implications for the broader experimental approach are further elaborated.

A thorough understanding of the LAr response within this stipulated low-energy range holds pivotal significance for optimizing the sensitivity of current and forthcoming experiments. This work lays the foundation for a more precise examination of dark matter interactions, pushing the boundaries of detection capabilities for low-mass dark matter.

Bibliography

[1] Jan H. Oort. "The Structure of the System of the Milky Way". In: *Bulletin of the Astronomical Institutes of the Netherlands* 5 (1930), p. 179.

[2] Fritz Zwicky. "Die Rotverschiebung von extragalaktischen Nebeln". In: *Helvetica Physica Acta* 6 (1933), p. 110.

[3] Vera C. Rubin and W. Kent Ford. "Rotation of the Andromeda Nebula from a Spectroscopic Survey of Emission Regions". In: *The Astrophysical Journal* 223 (1978), p. 1.

[4] Albert Einstein. "The Field Equations of Gravitation". In: *Sitzungsber. Preuss. Akad. Wiss. Berlin (Math. Phys.)* 1915 (1915), pp. 844–847.

[5] P. J. E. Peebles. "Dark matter and the origin of galaxies and globular star clusters". In: *Astrophys. J.* 277 (1984), pp. 470–477. DOI: 10.1086/161714.

[6] A. Friedman. "On the Curvature of space". In: *Z. Phys.* 10 (1922), pp. 377–386. DOI: 10.1007/BF01332580.

[7] Georges Lemaitre. "A Homogeneous Universe of Constant Mass and Increasing Radius accounting for the Radial Velocity of Extra-galactic Nebulæ". In: *Mon. Not. Roy. Astron. Soc.* 91.5 (1931), pp. 483–490. DOI: 10.1093/mnras/91.5.483.

[8] Planck Collaboration et al. "Planck 2018 results. VI. Cosmological parameters". In: *Astronomy and Astrophysics* 641 (2020), A6. DOI: 10.1051/0004-6361/201833910.

[9] A. A. Penzias and R. W. Wilson. "A Measurement of Excess Antenna Temperature at 4080 Mc/s". In: *The Astrophysical Journal* 142 (1965), pp. 419–421. DOI: 10.1086/148307.

[10] Viatcheslav Mukhanov. *Physical foundations of cosmology*. Cambridge University Press, 2005.

[11] Douglas Clowe et al. "A Direct Empirical Proof of the Existence of Dark Matter*". In: *The Astrophysical Journal* 648.2 (Aug. 2006), p. L109. DOI: 10.1086/508162. URL: https://dx.doi.org/10.1086/508162.

[12] M. Markevitch et al. "Direct Constraints on the Dark Matter Self-Interaction Cross Section from the Merging Galaxy Cluster 1E 0657–56". In: *The Astrophysical Journal* 606.2 (May 2004), p. 819. DOI: 10.1086/383178. URL: https://dx.doi.org/10.1086/383178.

[13] Samuel D. McDermott, Hai-Bo Yu, and Kathryn M. Zurek. "Turning off the lights: How dark is dark matter?" In: *Physical Review D* 83.6 (Mar. 2011). ISSN: 1550-2368. DOI: 10.1103/physrevd.83.063509. URL: http://dx.doi.org/10.1103/PhysRevD.83.063509.

[14] A. D. Dolgov et al. "Constraints on millicharged particles from Planck data". In: *Physical Review D* 88.11 (Dec. 2013). ISSN: 1550-2368. DOI: 10.1103/physrevd.88.117701. URL: http://dx.doi.org/10.1103/PhysRevD.88.117701.

[15] Eugenio Del Nobile, Marco Nardecchia, and Paolo Panci. "Millicharge or decay: a critical take on Minimal Dark Matter". In: *Journal of Cosmology and Astroparticle Physics* 2016.04 (Apr. 2016), pp. 048–048. ISSN: 1475-7516. DOI: 10.1088/1475-7516/2016/04/048. URL: http://dx.doi.org/10.1088/1475-7516/2016/04/048.

[16] Vid Iršič et al. "New constraints on the free-streaming of warm dark matter from intermediate and small scale Lyman-α forest data". In: *Physical Review D* 96.2 (July 2017). ISSN: 2470-0029. DOI: 10.1103/physrevd.96.023522. URL: http://dx.doi.org/10.1103/PhysRevD.96.023522.

[17] Hans Peter Nilles. "Supersymmetry, Supergravity and Particle Physics". In: *Phys. Rept.* 110 (1984), pp. 1–162. DOI: 10.1016/0370-1573(84)90008-5.

[18] A Dolgov. "Massive sterile neutrinos as warm dark matter". In: *Astroparticle Physics* 16.3 (Jan. 2002), pp. 339–344. ISSN: 0927-6505. DOI: 10.1016/s0927-6505(01)00115-3. URL: http://dx.doi.org/10.1016/S0927-6505(01)00115-3.

[19] Sean Tulin and Hai-Bo Yu. "Dark matter self-interactions and small scale structure". In: *Physics Reports* 730 (Feb. 2018), pp. 1–57. ISSN: 0370-1573. DOI: 10.1016/j.physrep.2017.11.004. URL: http://dx.doi.org/10.1016/j.physrep.2017.11.004.

[20] JiJi Fan, Andrey Katz, and Jessie Shelton. "Direct and indirect detection of dissipative dark matter". In: *Journal of Cosmology and Astroparticle Physics* 2014.06 (June 2014), pp. 059–059. ISSN: 1475-7516. DOI: 10.1088/1475-7516/2014/06/059. URL: http://dx.doi.org/10.1088/1475-7516/2014/06/059.

[21] R. D. Peccei and H. R. Quinn. "CP Conservation in the Presence of Pseudoparticles". In: *Physical Review Letters* 38.25 (1977), pp. 1440–1443. DOI: 10.1103/PhysRevLett.38.1440.

[22] S. Weinberg. "A New Light Boson?" In: *Physical Review Letters* 40.4 (1978), pp. 223–226. DOI: 10.1103/PhysRevLett.40.223.

[23] F. Wilczek. "Problem of Strong P and T Invariance in the Presence of Instantons". In: *Physical Review Letters* 40.5 (1978), pp. 279–282. DOI: 10.1103/PhysRevLett.40.279.

[24] M. Dine, W. Fischler, and M. Srednicki. "A Simple Solution to the Strong CP Problem with a Harmless Axion". In: *Physics Letters B* 104.3 (1981), pp. 199–202. DOI: 10.1016/0370-2693(81)90590-6.

[25] J. Preskill, M. B. Wise, and F. Wilczek. "Cosmology of the Invisible Axion". In: *Physics Letters B* 120.1-3 (1983), pp. 127–132. DOI: 10.1016/0370-2693(83)90637-8.

[26] L. F. Abbott and P. Sikivie. "A Cosmological Bound on the Invisible Axion". In: *Physics Letters B* 120.1-3 (1983), pp. 133–136. DOI: 10.1016/0370-2693(83)90638-X.

[27] P. Sikivie. "Experimental Tests of the "Invisible" Axion". In: *Physical Review Letters* 51.16 (1983), pp. 1415–1417. DOI: 10.1103/PhysRevLett.51.1415.

[28] Edward W. Kolb and Michael S. Turner. *The Early Universe*. Vol. 69. Addison-Wesley, 1990.

[29] Gary Steigman, Basudeb Dasgupta, and John F. Beacom. "Precise Relic WIMP Abundance and its Impact on Searches for Dark Matter Annihilation". In: *Physical Review D* 86.2 (2012), p. 023506. DOI: 10.1103/PhysRevD.86.023506.

[30] Benjamin W. Lee and Steven Weinberg. "Cosmological lower bound on heavy neutrino masses". In: *Physical Review Letters* 39.4 (1977), p. 165. DOI: 10.1103/PhysRevLett.39.165.

[31] M. H. Ahn et al. "Measurement of neutrino oscillation by the K2K experiment". In: *Physical Review D* 74 (2006), p. 072003. DOI: 10.1103/PhysRevD.74.072003.

[32] S. Dodelson and L. M. Widrow. "Sterile neutrinos as dark matter". In: *Physical Review Letters* 72.1 (1994), pp. 17–20. DOI: 10.1103/PhysRevLett.72.17.

[33] L. J. Hall et al. "Freeze-in production of FIMP dark matter". In: *Journal of High Energy Physics* 2010.3 (2010), p. 080. DOI: 10.1007/JHEP03(2010)080.

[34] Mark W. Goodman and Edward Witten. "Detectability of Certain Dark-Matter Candidates". In: *Phys. Rev. D* 31 (12 1985), pp. 3059–3063. DOI: 10.1103/PhysRevD.31.3059. URL: https://link.aps.org/doi/10.1103/PhysRevD.31.3059.

[35] A. Drukier and L. Stodolsky. "Principles and applications of a neutral-current detector for neutrino physics and astronomy". In: *Phys. Rev. D* 30.11 (Dec. 1984), pp. 2295–2309. DOI: 10.1103/PhysRevD.30.2295.

[36] J.D. Lewin and P.F. Smith. "Review of mathematics, numerical factors, and corrections for dark matter experiments based on elastic nuclear recoil". In: *Astroparticle Physics* 6.1 (1996), pp. 87–112. ISSN: 0927-6505. DOI: https://doi.org/10.1016/S0927-6505(96)00047-3. URL: https://www.sciencedirect.com/science/article/pii/S0927650596000473.

[37] J. Binney and S. Tremaine. *Galactic Dynamics*. 2nd. Princeton: Princeton University Press, 2008.

[38] B. Loer. "Towards a Depleted Argon Time Projection Chamber WIMP Search: DarkSide Prototype Analysis and Predicted Sensitivity". PhD thesis. Princeton University, 2011.

[39] ANNE M. GREEN. "Astrophysical uncertainties on direct detection experiments". In: *Modern Physics Letters A* 27.03 (Jan. 2012), p. 1230004. ISSN: 1793-6632. DOI: 10.1142/s0217732312300042. URL: http://dx.doi.org/10.1142/S0217732312300042.

[40] Christopher McCabe. "Astrophysical uncertainties of dark matter direct detection experiments". In: *Phys. Rev. D* 82 (2 July 2010), p. 023530. DOI: 10.1103/PhysRevD.82.023530. URL: https://link.aps.org/doi/10.1103/PhysRevD.82.023530.

[41] Gerard Jungman, Marc Kamionkowski, and Kim Griest. "Supersymmetric dark matter". In: *Physics Reports* 267.5–6 (Mar. 1996), pp. 195–373. ISSN: 0370-1573. DOI: 10.1016/0370-1573(95)00058-5. URL: http://dx.doi.org/10.1016/0370-1573(95)00058-5.

[42] RICHARD W. SCHNEE. "Introduction to Dark Matter Experiments". In: *Physics of the Large and the Small*. WORLD SCIENTIFIC, Mar. 2011. DOI: 10.1142/9789814327183_0014. URL: http://dx.doi.org/10.1142/9789814327183_0014.

[43] Eugenio Del Nobile. *The Theory of Direct Dark Matter Detection: A Guide to Computations*. Springer International Publishing, 2022. ISBN: 9783030952280. DOI: 10.1007/978-3-030-95228-0. URL: http://dx.doi.org/10.1007/978-3-030-95228-0.

[44] S. Navas et al. "Review of particle physics". In: *Phys. Rev. D* 110.3 (2024), p. 030001. DOI: 10.1103/PhysRevD.110.030001.

[45] James B. R. Battat. "Resource Letter DM1: Dark matter: An overview of theory and experiment". In: *American Journal of Physics* 92.4 (Apr. 2024), pp. 247–257. ISSN: 0002-9505. DOI: 10.1119/5.0187346. eprint: https://pubs.aip.org/aapt/ajp/article-pdf/92/4/247/20162494/247_1_5.0187346.pdf. URL: https://doi.org/10.1119/5.0187346.

[46] P. Agnes et al. "Search for Dark Matter Particle Interactions with Electron Final States with DarkSide-50". In: *Phys. Rev. Lett.* 130 (10 Mar. 2023), p. 101002. DOI: 10.1103/PhysRevLett.130.101002. URL: https://link.aps.org/doi/10.1103/PhysRevLett.130.101002.

[47] J. Aalbers et al. "First Dark Matter Search Results from the LUX-ZEPLIN (LZ) Experiment". In: *Phys. Rev. Lett.* 131 (4 July 2023), p. 041002. DOI: 10.1103/PhysRevLett.131.041002. URL: https://link.aps.org/doi/10.1103/PhysRevLett.131.041002.

[48] D. S. Akerib et al. "Results from a Search for Dark Matter in the Complete LUX Exposure". In: *Phys. Rev. Lett.* 118 (2 Jan. 2017), p. 021303. DOI: 10.1103/PhysRevLett.118.021303. URL: https://link.aps.org/doi/10.1103/PhysRevLett.118.021303.

[49] E. Aprile et al. "First Dark Matter Search with Nuclear Recoils from the XENONnT Experiment". In: *Phys. Rev. Lett.* 131 (4 July 2023), p. 041003. DOI: 10.1103/PhysRevLett.131.041003. URL: https://link.aps.org/doi/10.1103/PhysRevLett.131.041003.

[50] R. Agnese et al. "Results from the Super Cryogenic Dark Matter Search Experiment at Soudan". In: *Phys. Rev. Lett.* 120 (6 Feb. 2018), p. 061802. DOI: 10.1103/PhysRevLett.120.061802. URL: https://link.aps.org/doi/10.1103/PhysRevLett.120.061802.

[51] Yue Meng et al. "Dark Matter Search Results from the PandaX-4T Commissioning Run". In: *Phys. Rev. Lett.* 127 (26 Dec. 2021), p. 261802. DOI: 10.1103/PhysRevLett.127.261802. URL: https://link.aps.org/doi/10.1103/PhysRevLett.127.261802.

[52] C. Amole et al. "Dark Matter Search Results from the PICO−60 C_3F_8 Bubble Chamber". In: *Phys. Rev. Lett.* 118 (25 June 2017), p. 251301. DOI: 10.1103/PhysRevLett.118.251301. URL: https://link.aps.org/doi/10.1103/PhysRevLett.118.251301.

[53] Tadayoshi Doke et al. "Absolute Scintillation Yields in Liquid Argon and Xenon for Various Particles". In: *Jap. J. Appl. Phys.* 41 (2002), pp. 1538–1545. DOI: 10.1143/JJAP.41.1538.

[54] Elena Aprile et al. *Noble Gas Detectors*. Wiley, 2008. ISBN: 978-3-527-40597-8. DOI: 10.1002/9783527610020.

[55] V Chepel and H Araújo. "Liquid noble gas detectors for low energy particle physics". In: *Journal of Instrumentation* 8.04 (Apr. 2013), R04001–R04001. ISSN: 1748-0221. DOI: 10.1088/1748-0221/8/04/r04001. URL: http://dx.doi.org/10.1088/1748-0221/8/04/R04001.

[56] Akira Hitachi et al. "Effect of ionization density on the time dependence of luminescence from liquid argon and xenon". In: *Phys. Rev. B* 27 (9 May 1983), pp. 5279–5285. DOI: 10.1103/PhysRevB.27.5279. URL: https://link.aps.org/doi/10.1103/PhysRevB.27.5279.

[57] J. Lindhard et al. "Integral equations governing radiation effects (Notes on atomic collisions, iii)". In: *Kgl. Danske Videnskab, Selskab. Mat. Fys. Medd.* 33 (Jan. 1963).

[58] J B Birks. "Scintillations from Organic Crystals: Specific Fluorescence and Relative Response to Different Radiations". In: *Proceedings of the Physical Society. Section A* 64.10 (Oct. 1951), p. 874. DOI: 10.1088/0370-1298/64/10/303. URL: https://dx.doi.org/10.1088/0370-1298/64/10/303.

[59] D.-M. Mei et al. "A model of nuclear recoil scintillation efficiency in noble liquids". In: *Astroparticle Physics* 30.1 (Aug. 2008), pp. 12–17. ISSN: 0927-6505. DOI: 10.1016/j.astropartphys.2008.06.001. URL: http://dx.doi.org/10.1016/j.astropartphys.2008.06.001.

[60] M. Miyajima et al. "Average energy expended per ion pair in liquid argon". In: *Phys. Rev. A* 9 (1974), pp. 1438–1443. DOI: 10.1103/PhysRevA.9.1438.

[61] H. Cao et al. "Measurement of scintillation and ionization yield and scintillation pulse shape from nuclear recoils in liquid argon". In: *Physical Review D* 91.9 (May 2015). ISSN: 1550-2368. DOI: 10.1103/physrevd.91.092007. URL: http://dx.doi.org/10.1103/PhysRevD.91.092007.

[62] T. H. Joshi et al. "First Measurement of the Ionization Yield of Nuclear Recoils in Liquid Argon". In: *Physical Review Letters* 112.17 (May 2014). ISSN: 1079-7114. DOI: 10.1103/physrevlett.112.171303. URL: http://dx.doi.org/10.1103/PhysRevLett.112.171303.

[63] Tadayoshi Doke et al. "Let dependence of scintillation yields in liquid argon". In: *Nuclear Instruments and Methods in Physics Research Section A: Accelerators, Spectrometers, Detectors and Associated Equipment* 269.1 (1988), pp. 291–296. ISSN: 0168-9002. DOI: https://doi.org/10.1016/0168-9002(88)90892-3. URL: https://www.sciencedirect.com/science/article/pii/0168900288908923.

[64] J. Thomas and D. A. Imel. "Recombination of electron-ion pairs in liquid argon and liquid xenon". In: *Physical Review A* 36.2 (1987), pp. 614–616.

[65] G. Jaffe. "The columnar theory of ionization". In: *Annalen der Physik* 42.10 (1913), p. 303.

[66] M Szydagis et al. "NEST: a comprehensive model for scintillation yield in liquid xenon". In: *Journal of Instrumentation* 6.10 (Oct. 2011), P10002–P10002. ISSN: 1748-0221. DOI: 10.1088/1748-0221/6/10/p10002. URL: http://dx.doi.org/10.1088/1748-0221/6/10/P10002.

[67] Carl Eric Dahl. "The physics of background discrimination in liquid xenon, and first results from Xenon10 in the hunt for WIMP dark matter". PhD thesis. Princeton University, 2009.

[68] D. R. Nygren. "Proceedings of the 1974 PEP Summer Study". In: *eConf* C740805 (1974), p. 58.

[69] C. Rubbia. "The Liquid Argon Time Projection Chamber: A New Concept for Neutrino Detectors". In: (May 1977).

[70] Paolo Agnes. "Direct Search for DarkMatter with the DarkSide Experiment". PhD thesis. Université Paris Diderot, 2016.

[71] P. Agnes et al. "DarkSide-50 532-day dark matter search with low-radioactivity argon". In: *Physical Review D* 98.10 (Nov. 2018). ISSN: 2470-0029. DOI: 10.1103/physrevd.98.102006. URL: http://dx.doi.org/10.1103/PhysRevD.98.102006.

[72] P. Agnes et al. "Sensitivity projections for a dual-phase argon TPC optimized for light dark matter searches through the ionization channel". In: *Phys. Rev. D* 107 (11 June 2023), p. 112006. DOI: 10.1103/PhysRevD.107.112006. URL: https://link.aps.org/doi/10.1103/PhysRevD.107.112006.

[73] P. Agnes et al. "Results From the First Use of Low Radioactivity Argon in a Dark Matter Search". In: *Phys. Rev. D* 93.8 (2016). [Addendum: Phys.Rev.D 95, 069901 (2017)], p. 081101. DOI: 10.1103/PhysRevD.93.081101. arXiv: 1510.00702 [astro-ph.CO].

[74] P. Agnes et al. "Performance of the ReD TPC, a novel double-phase LAr detector with silicon photomultiplier readout". In: *The European Physical Journal C* 81.11 (Nov. 2021). ISSN: 1434-6052. DOI: 10.1140/epjc/s10052-021-09801-6. URL: http://dx.doi.org/10.1140/epjc/s10052-021-09801-6.

[75] P. Agnes et al. "Calibration of the liquid argon ionization response to low energy electronic and nuclear recoils with DarkSide-50". In: *Physical Review D* 104.8 (Oct. 2021). ISSN: 2470-0029. DOI: 10.1103/physrevd.104.082005. URL: http://dx.doi.org/10.1103/PhysRevD.104.082005.

[76] P. Agnes et al. "Measurement of the liquid argon energy response to nuclear and electronic recoils". In: *Physical Review D* 97.11 (June 2018). ISSN: 2470-0029. DOI: 10.1103/physrevd.97.112005. URL: http://dx.doi.org/10.1103/PhysRevD.97.112005.

[77] H. Cao et al. "Measurement of scintillation and ionization yield and scintillation pulse shape from nuclear recoils in liquid argon". In: *Physical Review D* 91.9 (May 2015). ISSN: 1550-2368. DOI: 10.1103/physrevd.91.092007. URL: http://dx.doi.org/10.1103/PhysRevD.91.092007.

[78] J. P. Biersack and J. F. Ziegler. "The Stopping and Range of Ions in Solids". In: *Ion Implantation Techniques*. Ed. by H. Ryssel and H. Glawischnig. Berlin, Heidelberg: Springer Berlin Heidelberg, 1982, pp. 122–156. DOI: 10.1007/978-3-642-68377-8_6.

[79] G. Moliere. "Theorie der Streuung schneller geladener Teilchen I. Einzelstreuung am abgeschirmten Coulomb-Feld". In: *Z. Naturforsch. A* 2 (1947), p. 133. DOI: 10.1515/zna-1947-0202.

[80] W. Lenz. "Über die Anwendbarkeit der statistischen Methode auf Ionengitter". In: *Zeitschrift für Physik* 77 (1932), p. 713. DOI: 10.1007/BF01342562.

[81] H. Jensen. "Die Ladungsverteilung in Ionen und die Gitterkonstante des Rubidiumbromids nach der statistischen Methode". In: *Zeitschrift für Physik* 77 (1932), p. 722. DOI: 10.1007/BF01342563.

[82] P. Agnes et al. "Constraints on directionality effect of nuclear recoils in a liquid argon time projection chamber". In: *The European Physical Journal C* 84.1 (2024), p. 24. DOI: 10.1140/epjc/s10052-023-12312-1. URL: https://doi.org/10.1140/epjc/s10052-023-12312-1.

[83] W. Mannhart. *Evaluation of the Cf-252 fission neutron spectrum between 0 MeV and 20 MeV*. Technical Report IAEA-TECDOC–410. International Atomic Energy Agency (IAEA), 1987.

[84] F. H. Froehner. *Watt spectrum fit to 252Cf prompt fission neutron data*. Technical Report IAEA-TECDOC–483. International Atomic Energy Agency (IAEA), 1988.

[85] N. Pino et al. "Study of low-energy nuclear recoils in liquid argon with the ReD experiment". In: *Journal of Instrumentation* 19.04 (Apr. 2024), p. C04054. DOI: 10.1088/1748-0221/19/04/C04054. URL: https://dx.doi.org/10.1088/1748-0221/19/04/C04054.

[86] K. Wisshak and F. Käppeler. "Large barium fluoride detectors". In: *Nuclear Instruments and Methods in Physics Research Section A: Accelerators, Spectrometers, Detectors and Associated Equipment* 227.1 (1984), pp. 91–96. ISSN: 0168-9002. DOI: https://doi.org/10.1016/0168-9002(84)90105-0. URL: https://www.sciencedirect.com/science/article/pii/0168900284901050.

[87] 3M. *3M™ Enhanced Specular Reflector Films*. Technical Data Sheet. 2017. URL: https://multimedia.3m.com/mws/media/1245089O/3m-enhanced-specular-reflector-films-3m-esr-tech-data-sheet.pdf.

[88] Fabio Acerbi et al. "Cryogenic Characterization of FBK HD Near-UV Sensitive SiPMs". In: *IEEE Transactions on Electron Devices* 64.2 (Feb. 2017), pp. 521–526. ISSN: 1557-9646. DOI: 10.1109/ted.2016.2641586. URL: http://dx.doi.org/10.1109/TED.2016.2641586.

[89] CRYOMECH. *Cryorefrigerator Specification Sheet: PT90 with CP2850*. http://www.cryomech.com/specificationsheet/PT90_ss.pdf. Data Sheet. Aug. 2013.

[90] Sigma Technologies. *SAES Getters: PS4-MT3*. http://www.saespuregas.com/Library/documents/s110-243_rev__528.pdf. Data Sheet. May 2012.

[91] Marco D'Incecco et al. "Development of a Novel Single-Channel, 24 cm2, SiPM-Based, Cryogenic Photodetector". In: *IEEE Transactions on Nuclear Science* 65.1 (Jan. 2018), pp. 591–596. ISSN: 1558-1578. DOI: 10.1109/tns.2017.2774779. URL: http://dx.doi.org/10.1109/TNS.2017.2774779.

[92] C. Savarese. "A novel light detector for DarkSide-20k". PhD thesis. Gran Sasso Science Institute, 2017.

[93] Claudio Piemonte et al. "Performance of NUV-HD Silicon Photomultiplier Technology". In: *IEEE Transactions on Electron Devices* 63.3 (2016), pp. 1111–1116. DOI: 10.1109/TED.2016.2516641.

[94] S. Vinogradov et al. "Probability Distribution and Noise Factor of Solid State Photomultiplier Signals with Cross-Talk and Afterpulsing". In: *IEEE Nucl. Science Symp. Conf. Rec.* 25 (2009), p. 1496.

[95] CAEN. *V1730/VX1730 and V1725/VX1725 16/8-channel 14-bit 500/250 MS/s Waveform Digitizer*. User Manual UM2792. June 2016.

[96] P. Agnes et al. "Low-Mass Dark Matter Search with the DarkSide-50 Experiment". In: *Phys. Rev. Lett.* 121 (8 Aug. 2018), p. 081307. DOI: 10.1103/PhysRevLett.121.081307. URL: https://link.aps.org/doi/10.1103/PhysRevLett.121.081307.

[97] P. Zakhary on behalf of the DarkSide collaboration. "37Ar source on-demand production and deployment for low-energy nuclear recoil measurement in ReD liquid Argon TPC". In: *Journal of Instrumentation* 19.06 (June 2024), p. C06003. DOI: 10.1088/1748-0221/19/06/C06003. URL: https://dx.doi.org/10.1088/1748-0221/19/06/C06003.

[98] S. Sangiorgio et al. "First demonstration of a sub-keV electron recoil energy threshold in a liquid argon ionization chamber". In: *NIM-A* 728 (2013), pp. 69–72. ISSN: 0168-9002. DOI: https://doi.org/10.1016/j.nima.2013.06.061. URL: https://www.sciencedirect.com/science/article/pii/S0168900213008942.

[99] R. Kishore et al. "^{37}Cl$(p,n)^{37}$Ar excitation function up to 24 MeV: Study of (p,n) reactions". In: *Phys. Rev. C* 12 (1 July 1975), pp. 21–27. DOI: 10.1103/PhysRevC.12.21. URL: https://link.aps.org/doi/10.1103/PhysRevC.12.21.

[100] R.O. Weber et al. "Cross sections and thermonuclear reaction rates of proton-induced reactions on 37Cl". In: *Nuclear Physics A* 439.1 (1985), pp. 176–188. ISSN: 0375-9474. DOI: https://doi.org/10.1016/0375-9474(85)90212-X. URL: https://www.sciencedirect.com/science/article/pii/037594748590212X.

[101] H. Michael, R. Wölfle, and S.M. Qaim. "Production of 37Ar". In: *The International Journal of Applied Radiation and Isotopes* 35.8 (1984), pp. 813–815. ISSN: 0020-708X. DOI: https://doi.org/10.1016/0020-708X(84)90096-6. URL: https://www.sciencedirect.com/science/article/pii/0020708X84900966.

[102] Christine M. Egnatuk and Steven R. Biegalski. "Radioargon production through the irradiation of calcium oxide". In: *Journal of Radioanalytical and Nuclear Chemistry* 298.1 (Oct. 2013), pp. 475–479. DOI: 10.1007/s10967-012-2400-z. URL: https://doi.org/10.1007/s10967-012-2400-z.

[103] E.M. Boulton et al. "Calibration of a two-phase xenon time projection chamber with a 37Ar source". In: *Journal of Instrumentation* 12.08 (Aug. 2017), P08004. DOI: 10.1088/1748-0221/12/08/P08004. URL: https://dx.doi.org/10.1088/1748-0221/12/08/P08004.

[104] D. G. Kelly et al. "The production of Ar-37 using a thermal neutron reactor flux". In: *Journal of Radioanalytical and Nuclear Chemistry* 318.1 (Oct. 2018), pp. 279–285. DOI: 10.1007/s10967-018-6130-8. URL: https://doi.org/10.1007/s10967-018-6130-8.

[105] G. Gerbier et al. "NEWS : a new spherical gas detector for very low mass WIMP detection". In: (Jan. 2014). arXiv: arXiv:1401.7902(2014) [astro-ph.IM].

[106] Yosuke Iwamoto et al. "Benchmark study of particle and heavy-ion transport code system using shielding integral benchmark archive and database for accelerator-shielding experiments". In: *Journal of Nuclear Science and Technology* 59.5 (2022), pp. 665–675. DOI: 10.1080/00223131.2023.2275736.

APPENDIX A

Two-Body Kinematics

In this Appendix, a comprehensive derivation of the kinematic equations governing a two-body scattering process is provided. This derivation applies equally to scenarios where m_1 is either a WIMP or a neutron, undergoing an elastic scattering with m_2, an argon atom initially at rest. The entire derivation is conducted within a relativistic framework, employing natural units where the speed of light $c = 1$.

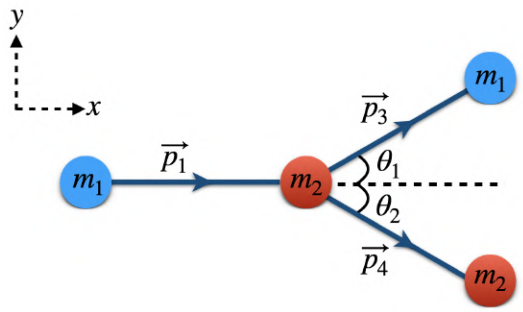

Figure A.1: A sketch of the elastic scattering between two particles with the legend showing the adopted directions of xy-plane.

The energy-momentum conservation equation can be written as

$$p_1^\mu + p_2^\mu = p_3^\mu + p_4^\mu, \tag{A.1}$$

where p_1^μ and p_3^μ are the neutron 4-momenta before and after the collision, respectively. While p_2^μ and p_4^μ are the argon atom 4-momenta before and after

the collision, respectively. They can be explicitly written in terms of their components as:

$$\begin{aligned} p_1^\mu &= (E_1, p_1, 0, 0) \\ p_2^\mu &= (m_2, 0, 0, 0) \\ p_3^\mu &= (E_3, p_3\cos\theta_1, p_3\sin\theta_1, 0) \\ p_4^\mu &= (E_4, p_4\cos\theta_2, -p_4\sin\theta_1, 0) \end{aligned} \tag{A.2}$$

Eq. A.1 consists of 4 independent equations. However, since the elastic scattering is constrained to the xy-plane, it simplifies to 3 non-zero equations:

$$\begin{aligned} E_1 + m_2 &= E_3 + E_4 \\ p_1 &= p_3\cos\theta_2 + p_4\cos\theta_2 \\ 0 &= p_3\sin\theta_2 - p_4\sin\theta_2 \end{aligned}$$

From Eq. A.1, we can construct an invariant relation, i.e. valid in all inertial frames, by moving p_3^μ to the left hand side (LHS) and squaring both sides. This yields:

$$[(p_1^\mu + p_2^\mu) - p_3^\mu]^2 = p_4^{\mu 2}$$

The right hand side (RHS) is simply m_2^2, while the LHS can be expanded as:

$$\begin{aligned} \text{LHS} &= (p_1^\mu + p_2^\mu)^2 + p_3^{\mu 2} - 2p_3^{\mu 2}(p_1^\mu + p_2^\mu) \\ &= p_1^{\mu 2} + p_2^{\mu 2} + 2p_1^\mu p_2^\mu + p_3^{\mu 2} - 2p_3^\mu p_1^\mu - 2p_3^\mu p_2^\mu \\ &= m_1^2 + m_2^2 + 2p_1^\mu p_2^\mu + m_1^2 - 2p_3^\mu p_1^\mu - 2p_3^\mu p_2^\mu = \text{RHS} \equiv m_2^2 \end{aligned}$$

The last equation can be expressed in terms of their components in Eq. A.2 and rearranged as:

$$p_1 p_3\cos\theta_1 + m_1^2 = E_1E_3 + E_3m_2 - E_1m_2$$

We notice that by subtracting m_2^2 from both sides, the RHS can be written as $(E_1 + m_2)(E_3 - m_2)$, This yields:

$$\frac{p_1p_3\cos\theta_1 + m_1^2 - m_2^2}{(E_1 + m_2)} = E_3 - m_2$$

Taking m_2 to the LHS and squaring both sides

$$E_3^2 = m_2^2 + 2m_2\frac{p_1p_3\cos\theta_1 + m_1^2 - m_2^2}{(E_1 + m_2)} + \left(\frac{p_1p_3\cos\theta_1 + m_1^2 - m_2^2}{(E_1 + m_2)}\right)^2 \tag{A.3}$$

Since $E_3^2 \equiv m_1^2 + p_3^2$, we can write Eq. A.3 after rearranging the terms as:

$$\underbrace{p_3^2\left[1 - \frac{p_1^2\cos^2\theta_1}{(E_1+m_2)^2}\right]}_{A} + \underbrace{p_3\left[\frac{-2m_2p_1\cos\theta_1}{(E_1+m_2)} - \frac{2(m_1^2-m_2^2)p_1\cos\theta_1}{(E_1+m_2)^2}\right]}_{B} + \underbrace{\left[(m_1^2-m_2^2) - 2m_2\frac{(m_1^2-m_2^2)}{(E_1+m_2)} - \frac{(m_1^2-m_2^2)^2}{(E_1+m_2)^2}\right]}_{C} = 0 \tag{A.4}$$

Now, we have expressed Eq. A.4 as a quadratic equation in the form $Ap_3^2 + Bp_3 + C = 0$. To proceed, we will further simplify the coefficients B and C. For B, we multiply the first term by $\frac{(E_1+m_2)}{(E_1+m_2)}$ and extract ($\frac{2p_1\cos\theta_1}{(E_1+m_2)^2}$ as a common factor:

$$\begin{aligned} B &\equiv \frac{2p_1\cos\theta_1}{(E_1+m_2)^2}\left[-m_2(E_1+m_2) - (m_1^2 - m_2^2)\right] \\ &= \frac{2p_1\cos\theta_1}{(E_1+m_2)^2}\left[-m_2E_1 - \cancel{m_2^2} - m_1^2 + \cancel{m_2^2}\right] \\ &= \frac{-2p_1\cos\theta_1}{(E_1+m_2)^2}\left[m_2E_1 - m_1^2\right] \end{aligned}$$

In C, we can factor out $\frac{(m_1^2-m_2^2)}{(E_1+m_2)^2}$, which results in:

$$\begin{aligned} C &\equiv \frac{(m_1^2-m_2^2)}{(E_1+m_2)^2}\left[(E_1+m_2)^2 - 2m_2(E_1+m_2) - (m_1^2-m_2^2)\right] \\ &= \frac{(m_1^2-m_2^2)}{(E_1+m_2)^2}\left[E_1^2 + \cancel{m_2^2} + \cancel{2m_2E_1} - \cancel{2m_2E_1} - \cancel{2m_2^2} - m_1^2 + \cancel{m_2^2}\right] \\ &= \frac{(m_1^2-m_2^2)}{(E_1+m_2)^2}\left[E_1^2 - m_1^2\right] = \frac{(m_1^2-m_2^2)}{(E_1+m_2)^2}p_1^2 \end{aligned}$$

Substituting these simplified coefficients back into Eq. A.4 and subsequently multiplying by $(E_1+m_2)^2$ yields:

$$\left[(E_1+m_2)^2 - p_1^2\cos^2\theta_1\right]p_3^2 + \left[-2p_1\cos\theta_1(m_2E_1 - m_1^2)\right]p_3 + (m_1^2-m_2^2)p_1^2 = 0$$

Since the quadratic equation $Ap_3^2 + Bp_3 + C = 0$ has an exact solution:

$$p_3 = \frac{-B \pm \sqrt{B^2 - 4AC}}{2A}$$

Therefore, the exact solution for the momentum of the outgoing neutron (p_3) can be written after extracting $(m_2E_1 - m_1^2)$ as a common factor as:

$$p_3 = \underbrace{\frac{(m_2E_1 + m_1^2)}{2\left[(E_1+m_2)^2 - p_1^2\cos^2\theta_1\right]}}_{a} \left[2p_1\cos\theta_1 \pm \sqrt{4p_1^2\cos^2\theta_1 - \underbrace{\frac{4p_1^2(m_1^2-m_2^2)}{(m_2E_1-m_1^2)^2}\left[(E_1+m_2)^2 - p_1^2\cos^2\theta_1\right]}_{b}}\right] \tag{A.5}$$

At this point, we consider the non-relativistic approximations for E_1 and E_1^2:

$$E_1 \approx E_{\text{rest}} + E_{\text{KE}} = m_1 + \frac{p_1^2}{2m_1}$$
$$E_1^2 \approx m_1^2 + p_1^2 + E_{\text{KE}}^2$$

Given that $m_n \approx 939.6\,\text{MeV}$ and $E_{\text{KE}} \leq 10\,\text{MeV}$. The E_{KE}^2 term can be considered negligible.

Thus, the terms within the radicand can be simplified as follows:

$$\begin{aligned}(m_2E_1 - m_1^2)^2 &= m_2^2E_1^2 + 2m_1^2m_2E_1 + m_1^4\\ &\approx m_2^2(m_1^2 + 2m_1E_{\text{KE}}) + 2m_1^2m_2(m_1 + E_{\text{KE}}) + m_1^4\\ &= m_2^2m_1^2 + 2m_2^2m_1E_{\text{KE}} + 2m_1^3m_2 + 2m_1^2m_2E_{\text{KE}} + m_1^4\\ &= m_1^2(m_2^2 + 2m_1m_2 + m_1^2) + 2m_1m_2E_{\text{KE}}(m_2 + m_1)\\ &= m_1^2(m_1 + m_2)^2 + 2m_1m_2E_{\text{KE}}(m_2 + m_1)\end{aligned}$$

$$\begin{aligned}(E_1 + m_2)^2 - p_1^2\cos^2\theta_1 &= E_1^2 + 2m_2E_1 + m_2^2 - p_1^2\cos^2\theta_1\\ &\approx m_1^2 + 2m_1E_{\text{KE}} + 2m_1m_2 + 2m_2E_{\text{KE}} + m_2^2 - p_1^2\cos^2\theta_1;\end{aligned}$$

But since $p_1^2 = 2m_1E_{\text{KE}}$,

$$\begin{aligned}&= m_1^2 + 2m_1m_2 + m_2^2 + 2m_1E_{\text{KE}}(1 - \cos^2\theta_1) + 2m_2E_{\text{KE}}\\ &= (m_1 + m_2)^2 + 2E_{\text{KE}}(m_1\sin^2\theta_1 + m_2)\end{aligned}$$

Consequently, the term labeled as b in Eq. A.5 can be expressed as follows, utilizing the identity $(m_1^2 - m_2^2) \equiv (m_1 + m_2)(m_1 - m_2)$:

$$4\frac{p_1^2(m_1 + m_2)^3(m_1 - m_2) + 2p_1^2E_{\text{KE}}(m_1 + m_2)(m_1 - m_2)(m_1\sin^2\theta_1 + m_2)}{m_1^2(m_1 + m_2)^2 + 2m_1m_2E_{\text{KE}}(m_2 + m_1)}$$

Similarly, the terms involving E_{KE} can be neglected, as their contributions are two orders of magnitude smaller than those involving the rest masses. Thus, the expression simplifies to:

$$b \equiv 4\frac{p_1^2(m_1 + m_2)^{\cancel{3}}(m_1 - m_2)}{m_1^2\cancel{(m_1 + m_2)^2}} = 4p_1^2\left(\frac{m_1^2 - m_2^2}{m_1^2}\right) = 4p_1^2\left(1 - \frac{m_2^2}{m_1^2}\right)$$

The term a in Eq. A.5 can be simplified by utilizing the previously derived reduced expressions for E_1 and the denominator.

$$\begin{aligned}a \equiv \frac{(m_2E_1 + m_1^2)}{2\left[(E_1 + m_2)^2 - p_1^2\cos^2\theta_1\right]} &= \frac{m_2(m_1 + E_{\text{KE}}) + m_1^2}{2(m_1 + m_2)^2 + 4E_{\text{KE}}(m_1\sin^2\theta_1 + m_2)}\\ &= \frac{m_1m_2 + m_2E_{\text{KE}} + m_1^2}{2(m_1 + m_2)^2 + 4E_{\text{KE}}(m_1\sin^2\theta_1 + m_2)}\end{aligned}$$

By introducing $m_2^2 - m_2^2 + m_1 m_2 - m_1 m_2$ to the numerator and neglecting the terms involving E_{KE}, the expression can be further reduced to:

$$a \approx \frac{m_1^2 + m_2^2 + 2m_1 m_2 - m_2^2 - m_1 m_2}{2(m_1 + m_2)^2}$$
$$\frac{(m_1 + m_2)^2 - m_2(m_1 + m_2)}{2(m_1 + m_2)^2} = \frac{1}{2}\left(1 - \frac{m_2}{m_1 + m_2}\right) = \frac{1}{2}\left(\frac{m_1}{m_1 + m_2}\right)$$

By integrating all components, Eq. A.5 can be approximated by:

$$p_3 \approx \frac{1}{2}\left(\frac{m_1}{m_1 + m_2}\right)\left[2p_1 \cos\theta_1 \pm \sqrt{4p_1^2 \cos^2\theta_1 - 4p_1^2\left(1 - \frac{m_2^2}{m_1^2}\right)}\right]$$
$$= \frac{1}{2}\left(\frac{m_1}{m_1 + m_2}\right)\left[2p_1 \cos\theta_1 \pm 2p_1\sqrt{\cos^2\theta_1 + \frac{m_2^2}{m_1^2} - 1}\right]$$

This indicates that the momentum of the outgoing particle can be accurately determined by the momentum of the incoming particle, the scattering angle post-collision, and the masses of the two particles involved in the interaction.

APPENDIX B

^{37}Ar Source On-demand Production & Deployment

A significant challenge in the pursuit of low-energy dark matter detection lies in accurately determining the detector's response in this energy range, as this is often cited as the dominant source of uncertainty in the final results. A widely employed strategy to address this issue involves exporting the response from external calibration detectors in detector-independent units. In liquid noble gas time projection chambers (TPCs), this typically involves measuring either the scintillation yield in "photons per keV" or the ionization yield in "electrons per keV.". These parameters depend on g_1 (the scintillation photon detection efficiency, expressed in photo-electrons per photon) and g_2 (the detected electroluminescence per ionization electron, quantified in photo-electrons per electron).

To overcome these limitations, a cross-calibration approach can be employed, where nuclear recoil (NR) and electronic recoil (ER) responses are measured relative to a common calibration reference point. ^{37}Ar has emerged as a promising candidate for cross-calibration in noble gas detectors. In this appendix, we present the first implementation of an on-demand ^{37}Ar production and deployment system within the ReD TPC, demonstrating its potential as an effective cross-calibration source for enhancing detector response characterization. This is based on my publication [97].

B.1 ^{37}Ar source: A "standard candle" in the low-energy calibration

To achieve precision in calibrating the liquid argon (LAr) response, the utilization of ^{37}Ar emerges as a strategic choice within the low-energy spectrum, distinguished by discernible peaks at 0.27 keV and 2.82 keV subsequent to electron capture, and characterized by a 35-day half-life, i.e. it would soon decay naturally once the calibration has been completed. ^{37}Ar can be produced through different reactions; namely $^{36}\mathrm{Ar}(n,\gamma)^{37}\mathrm{Ar}$, $^{37}\mathrm{Cl}(p,n)^{37}\mathrm{Ar}$, or $^{40}\mathrm{Ca}(n,\alpha)^{37}\mathrm{Ar}$. The first reaction has been used in [98]. The second reaction necessitates access to a proton beam facility and has been applied in the studies outlined in [99, 100]. Investigations conducted by [101, 102, 103] predominantly relied on the final reaction. Nonetheless, a recurring challenge associated with this reaction lies in the extraction of ^{37}Ar from the matrix, typically involving chemical or thermal treatments.

There is another possibility reported in [104] that ^{37}Ar can be produced from nano-CaO as a gas phase radionuclide by irradiation in vacuum. This suggests the possibility of liberation from nano-CaO without chemical or heating interventions. Therefore, our proposed on-demand methodology involves irradiating nano-CaO powder with a neutron source, and facilitating the diffusion of the resulting ^{37}Ar into the argon within the TPC via a gas circulation system. Notably, a similar approach was implemented in a spherical gaseous detector utilizing calcium salt powder [105].

Given the current interest in low-mass WIMPs searches, it's important to quantify NR yields in LAr relative to low-energy benchmarks, such as ^{37}Ar, in order to cross-calibrate prospective detectors.

By employing PHITS Monte Carlo (MC) simulation [106], we assessed irradiating 40 g of nano-CaO powder with the INFN-LNS Am-Be source (34 GBq, 2.2×10^6 neutrons/s). This simulation resulted in the production of 100 Bq of ^{37}Ar during a 10-day irradiation period. Another factor to be considered here is the relative proportion of LAr volume enclosed by the TPC to the total LAr volume within the system, with the chamber constituting 3 % of the latter. Therefore we can anticipate the detectability of 3 Bq of ^{37}Ar within the TPC in case of 100 % extraction efficiency.

Our efforts encompassed the preparation of the ^{37}Ar source, the irradiation was conducted at INFN-LNS. The irradiation occurred within a PE shielding in the "Hot Room" at INFN-LNS and lasted for 18 days and 23 hours till the system is ready, see Fig. B.1.

Additionally, an indirect assessment of ^{37}Ar yield through the examination of associated ^{42}K production has been performed. This auxiliary measurement

Figure B.1: *Left*: The nano-CaO powder container next to the Am-Be source inside a PE shielding. *Right*: After irradiation, the container is placed inside the HPGe detector to examine the associated ^{42}K production.

was done with the assistance of INFN-LNS experts and the use of the available HPGe detector, as shown in Fig. B.1. ^{42}K, one of the byproducts of the activation process, was observed with 2.9 ± 0.5 Bq. Based on the simulation, this implied that ^{37}Ar should have been activated conservatively with $\mathcal{O}(10^2)$ Bq. Nevertheless, to mitigate complete dependence on the HPGe measurements, given some of their inherent uncertainties, we can assert, albeit without precise quantification, that the activation of ^{37}Ar has *at least* taken place as anticipated in the simulation.

B.2 ^{37}Ar source: Calibration campaign

^{37}Ar is released spontaneously as a gaseous radio-nuclide post-irradiation. To transfer ^{37}Ar to a radiochemically clean receptacle, such as the TPC, can theoretically be accomplished by allowing it to diffuse out due to a pressure gradient, while preserving the integrity of the irradiated nano-CaO powder. Consequently, we configured Swagelok components to house the nano-powder, as depicted in Fig. B.2.

Initial trials were conducted in collaboration with experts from INFN-LNS, utilizing a setup comprising a dry pump, a turbo pump, a pressure gauge, a scale, and various types of valves. Employing the dry pump, we achieved a vacuum of 8×10^{-2} mbar with an average pumping rate of approximately 1 mbar/8s. Subsequently, we explored the combination of the dry pump with the Pfeiffer HiCube 80 Turbo Pumping Station, achieving a plateau of 6.9×10^{-4}

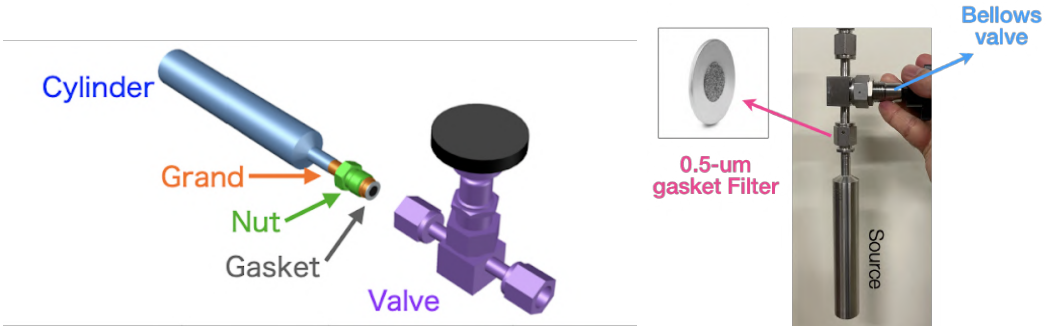

Figure B.2: The *left* diagram depicts Swagelok components housing CaO nano-powder, while the *right* image emphasizes the actual container, spotlighting the 0.5 µm gasket filter and the bellows valve linking the container to the gas panel.

mbar after 3 hours of pumping, which remained stable overnight with minimal fluctuations.

B.2.1 On-demand Production

The irradiation procedure commenced with the addition of 40 grams of nano-CaO powder into the container. The remaining volume was then evacuated and filled with Ar (class-6) gas at a pressure of 1.2 bar. The irradiation process utilized the Am-Be source as described in Sec. B.1. The Gas Panel is illustrated in Fig. B.3. The vacuuming process along the line (between HV107 and HV110) was initiated through HV111, with the CaO container valve closed. The vacuuming process reached a pressure of 7×10^{-2} mbar. Subsequently, the HV111 valve was opened which resulted in a pressure of 6×10^{-2} mbar.

Following this step, HV111 was closed, and the vacuuming of the line was stopped. The valve above the CaO holder was then opened, allowing the gas within the holder to be extracted to the gas panel located between HV107 and HV110. Subsequently, after some time enough for diffusing the generated ^{37}Ar out of holder to the gas conduit feeding the TPC, the valve was closed.

The sequential opening of HV107 and HV110, coupled with the closure of PV102, caused a decrease in pressure within the gas panel from 1860 to 1830 mbar. At this point, the Ar gas from the gas panel was intended to propel the ^{37}Ar inside the system. Upon closing HV107 and HV110 and opening PV102, the entire source loop was excluded, resulting in an increase in pressure within the gas panel from 1830 to 1860 mbar.

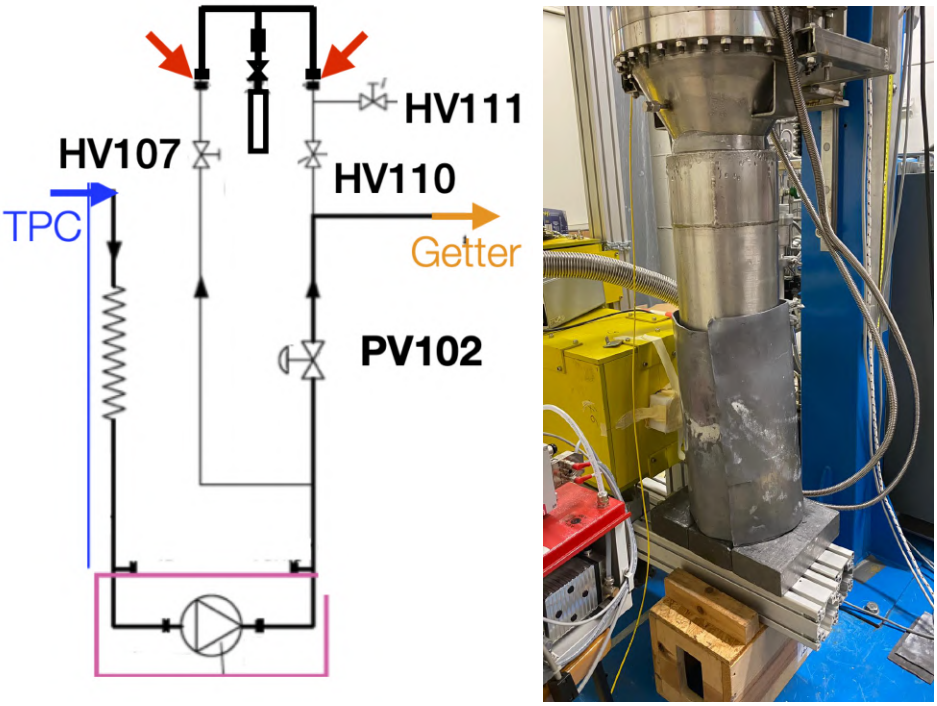

Figure B.3: The *left* schematic of the gas panel delineates the ^{37}Ar calibration loop in relation to the gas conduit supplying the TPC (indicated by a blue arrow) and the pipe leading to the purification system "Getter" (indicated by an orange arrow). The ^{37}Ar source bottle is connected in between the red arrows. On the *right* side, the image portrays the cryostat containing the TPC shielded with lead during data acquisition.

B.2.2 Data Analysis

We took data for 6.5-hour before ^{37}Ar injection for background and for 2.5 hours after the ^{37}Ar diffusion into the TPC in the same DAQ conditions in "S2-trigger" Mode. In this mode, the trigger fires on S2 pulse since S1 from ^{37}Ar event is too small to be triggered efficiently. Waveforms were recorded with 88 µs time window, with post trigger size of 27 % (i.e. [-64.24, +23.76] µs). Coincidence of three SiPMs among the top inner eight SiPMs was required within 2032 ns. This DAQ configuration achieved a target threshold of 15 ADC, approximately 0.5 PE. A series of tests on the DAQ system was conducted, culminating in the successful establishment of a triggering scheme tailored for low energy thresholds. This achievement was validated through its application to ^{83m}Kr data utilizing the S2-trigger mode, demonstrating efficacy with a threshold around 1 PE level. The cryostat hosting the TPC was shielded with a layer of lead surrounding it and beneath it to suppress the accidental event rate. An event is considered if there is at least a 5 ms delay from the previously triggered event. We applied fiducialization looking only at events happening in the inner 2 cm of the TPC.

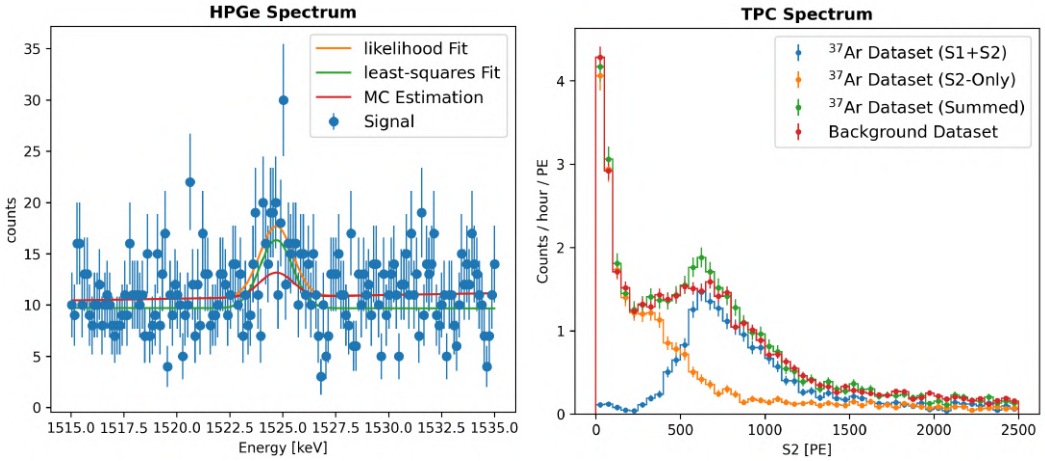

Figure B.4: The left figure presents the HPGe Spectrum centered on the ^{42}K peak at 1524.7 keV compared to the MC expectation. The right figure displays the TPC S2 spectrum encompassing the ^{37}Ar 0.27 keV L-shell and the 2.82 keV K-shell radiation peaks.

The analysis can neither confirm nor reject the observation of ^{37}Ar. Assuming 100 % liberation efficiency of ^{37}Ar from the CaO holder, MC expected ^{37}Ar activity to be 0.5 Bq in the final sample of events incorporating all quality cuts. This corresponds to 8 counts/hour/PE for the k-shell peak. Since this is on the limit of our system sensitivity, we report the observed spectrum before and after ^{37}Ar injection, as illustrated in Fig. B.4. One can find a tiny excess in the vicinity of 600 PE, which could match the ^{37}Ar prediction. However, this potential indication could be an artifact of the limit of our system sensitivity to the S1+S2 and S2-Only populations culminating the summed-up observed spectrum shown in green. The background spectrum, in red, represents the summation of the two populations.

B.3 Key Remarks

The deployment of the CaO-containing holder to the ReD experiment system through the gas panel was successful; The nano-powder was still intact inside the container and no damage was observed in any of the system components. The successful observation of ^{42}K, one of the byproducts suggests the success of the activation process of ^{37}Ar, albeit without precise quantification of its activity since the HPGe measurement is susceptible to some uncertainties. There are some hypotheses for not observing a conclusive evidence for ^{37}Ar, which include:

- The produced ^{37}Ar atoms could not liberate nor diffuse out from the matrix because of the nano-powder being damp or because of the powder almost fully filling up the holder.

- The DAQ system configuration or the reconstruction algorithm are not sensitive enough to such low-energy signal.

Nevertheless, we learnt some lessons for future measurements. This method is reusable and can be done on demand. The CaO nano-powder might have been humid inside the container, which means that pumping was not effective enough, so we might improve by utilizing heating tapes. The ratio between the empty space and the powder-filled space inside the container affects the liberation efficiency significantly. Adjusting the DAQ system and tuning it to trigger on ^{37}Ar event is not straightforward and needs careful consideration of background rate, signal-to-noise ratio of single PE, dark noise, and the acquisition window.